Doklady Physics, Vol. 46, No. 6, 2001, pp. 377–379. Translated from Doklady Akademii Nauk, Vol. 378, No. 4, 2001, pp. 463–465.

PHYSICS

The Eikonal Equation in Parametrized Nonlinear Electrodynamics of Vacuum

V. I. Denisov and I. P. Denisova

Presented by Academician A.R. Khokhlov September 19, 2000

Received September 26, 2000

At the beginning of the 60s, the appearance of lasers was followed by fast development of the electrodynamics of nonlinear media. Progress in the experimental technique achieved at that time made it possible to observe a number of nonlinear effects [1, 2] proceeding in crystals under the action of intense laser radiation.

However, it follows from fundamental physical reasons that electrodynamics is nonlinear not only in material media but in vacuum as well. Under conditions of laboratory experiments, when the magnitudes of the fields **B** and **E** are much smaller than the characteristic quantum-electrodynamic value $B_q = \frac{m^2c^3}{e\hbar} = 4.41 \times 10^{13}$ Gs, according to the terminology introduced by R.V. Khokhlov, a vacuum is a nonlinear nondispersive medium with extremely small magnetic and electric susceptibilities. Therefore, it is not an easy task to study the effects of nonlinear electrodynamics in a vacuum. However, at present, a possibility associated with further development of superhigh-resolution laser spectroscopy [3] appeared, which allows the effects caused by the nonlinearity of electrodynamics in a vacuum to be observed in optical experiments.

In field theory, several different models of the nonlinear electrodynamics of vacuum are considered. In the case of weak fields, their Lagrangian can be written out in the parameterized form [6]:

$$L = \frac{1}{8\pi}\{[\mathbf{E}^2 - \mathbf{B}^2] + \xi[\eta_1(\mathbf{E}^2 - \mathbf{B}^2)^2 + 4\eta_2(\mathbf{BE})^2]\} + \frac{\tau_1 g}{8\pi}\{-\partial_i F^{ik}\partial_j F^{j\cdot}_{\cdot k} + F_{ij}\Box F^{ij}\} + O(\xi^2 B^6), \quad (1)$$

where $\Box = \Delta - \frac{\partial^2}{c^2\partial t^2}$, $\xi = \frac{1}{B_q^2}$, $g = \frac{\alpha\hbar^2}{\pi^2 m^2 c^2}$, and the values of dimensionless post-Maxwellian parameters η_1, η_2, and τ_1 depend on the model chosen for the nonlinear electrodynamics of vacuum.

In particular, in Heisenberg–Einstein nonlinear electrodynamics, the parameters η_1, η_2, and τ_1 have quite concrete values [9]: $\eta_1 = \frac{\alpha}{45\pi} = 5.1 \times 10^{-5}$, $\eta_2 = \frac{7\alpha}{180\pi} = 9 \times 10^{-5}$, and $\tau_1 = \frac{1}{360}$. At the same time, in the Born–Infeld theory, these parameters are expressed in terms of an unknown constant a^2: $\eta_1 = \eta_2 = \frac{a^2 B_q^2}{4}$ and $\tau_1 = 0$.

Equations for the electromagnetic field in nonlinear electrodynamics are similar to those of nonlinear electrodynamics of continua:

$$\begin{aligned} \mathrm{rot}\mathbf{H} &= \frac{1}{c}\frac{\partial \mathbf{D}}{\partial t}, \quad \mathrm{div}\mathbf{D} = 0, \quad \mathbf{D} = 4\pi\frac{\partial L}{\partial \mathbf{E}}, \\ \mathrm{rot}\mathbf{E} &= -\frac{1}{c}\frac{\partial \mathbf{B}}{\partial t}, \quad \mathrm{div}\mathbf{B} = 0, \quad \mathbf{H} = -4\pi\frac{\partial L}{\partial \mathbf{B}}. \end{aligned} \quad (2)$$

Using expression (1), it is easy to expand the vectors **D** and **H** in powers of $\frac{B}{B_q}$ and $\frac{E}{B_q}$ with a post-Maxwellian accuracy of the first order:

$$\begin{aligned} \mathbf{D} &= \mathbf{E} + 2\xi\{\eta_1(\mathbf{E}^2 - \mathbf{B}^2)\mathbf{E} + 2\eta_2(\mathbf{BE})\mathbf{B}\} + 24\pi g\tau_1\Box\mathbf{E}, \\ \mathbf{H} &= \mathbf{B} + 2\xi\{\eta_1(\mathbf{E}^2 - \mathbf{B}^2)\mathbf{B} - 2\eta_2(\mathbf{BE})\mathbf{E}\} + 24\pi g\tau_1\Box\mathbf{B}. \end{aligned} \quad (3)$$

From the standpoint of the eikonal equation, according to the laws of nonlinear electrodynamics, the propagation of a weak electromagnetic wave in vacuum through an imposed external electromagnetic field is equivalent to propagation of this wave in a certain effective space–time whose metric tensor depends on the magnitude and the direction of the external electromagnetic field.

Moscow State University,
Vorob'evy gory, Moscow, 119899 Russia

1028-3358/01/4606-0377$21.00

We now find the components of the metric tensor in this space–time for the case when a weak electromagnetic wave with frequency ω propagates in the field of an intense laser radiation having a frequency Ω. We denote the vectors of electric and magnetic fields for the first and the second of these waves as **e** and **b** and **E** and **B**, respectively.

In the zeroth approximation over the vectors **b** and **e**, the system of nonlinear differential equations (2) has a solution in the form of a plane elliptically polarized wave:

$$\mathbf{E} = \mathbf{E}_1\cos(\Omega t - \mathbf{Kr}) + \mathbf{E}_2\sin(\Omega t - \mathbf{Kr}),$$
$$(\mathbf{E}_1\mathbf{E}_2) = 0,\ \mathbf{B} = \frac{c}{\Omega}[\mathbf{KE}],\ \frac{\Omega^2}{c^2} = \mathbf{K}^2, \qquad (4)$$
$$(\mathbf{KE}_1) = (\mathbf{KE}_2) = 0.$$

Invariants of this wave are equal to zero. Therefore, in the first approximation over **b** and **e**, system of equations (2), (3) takes the form

$$\mathrm{rot}\mathbf{e} = -\frac{1}{c}\frac{\partial \mathbf{b}}{\partial t}, \qquad (5)$$

$$(1 + 3g\tau_1\Box)\left(\mathrm{rot}\mathbf{b} - \frac{1}{c}\frac{\partial \mathbf{e}}{\partial t}\right) + 4\eta_1\xi\left\{[\mathbf{B}\nabla\{(\mathbf{Bb}) - (\mathbf{Ee})\}]\right.$$
$$\left. + \frac{\mathbf{E}}{c}\frac{\partial}{\partial t}\{(\mathbf{Bb}) - (\mathbf{Ee})\}\right\} + 4\eta_2\xi\left\{[\mathbf{E}\nabla\{(\mathbf{Be}) + (\mathbf{bE})\}]\right.$$
$$\left. - \frac{\mathbf{B}}{c}\frac{\partial}{\partial t}\{(\mathbf{Be}) + (\mathbf{bE})\}\right\} = 0.$$

It follows from these equations that the expression $\mathrm{rot}\mathbf{b} - \frac{\partial \mathbf{e}}{c\partial t}$ differs from zero by first-order post-Maxwellian terms. Therefore, the expression $3g\tau_1\Box\left\{\mathrm{rot}\mathbf{b} - \frac{\partial \mathbf{e}}{c\partial t}\right\}$ has the second order of smallness and should be omitted since initial equations (5) are written out with an accuracy to the terms of the first order of smallness. We represent the vectors **b** and **e** in the form

$$\mathbf{b} = \mathbf{b}_0 e^{iS},\quad \mathbf{e} = \mathbf{e}_0 e^{iS}, \qquad (6)$$

where $S = S(t, \mathbf{r})$ is the eikonal and we consider the vectors $\mathbf{b}_0$ and $\mathbf{e}_0$ as weakly varying functions of t and **r** compared to $\exp[iS(t, \mathbf{r})]$.

Substituting expression (6) into Eq. (5) and eliminating vector **b**, we arrive at the system of linear algebraic equations $\Pi^{\alpha\beta}e_\beta = 0$ with respect to three components of the vector $e_\beta = (\mathbf{e})_\beta$, where

$$\Pi_{\alpha\beta} = \left[(\nabla S)^2 - \left(\frac{1}{c}\frac{\partial S}{\partial t}\right)^2\right]\delta_{\alpha\beta} - \frac{\partial S}{\partial x^\alpha}\frac{\partial S}{\partial x^\beta}$$
$$- 4\xi\left\{\eta_1\left[\frac{K_\alpha}{K}(\mathbf{E}\nabla S) - \left[\frac{1}{c}\frac{\partial S}{\partial t} + \frac{(\mathbf{K}\nabla S)}{K}\right]E_\alpha\right]\right.$$
$$\left.\times\left[\frac{K_\beta}{K}(\mathbf{E}\nabla S) - \left[\frac{1}{c}\frac{\partial S}{\partial t} + \frac{(\mathbf{K}\nabla S)}{K}\right]E_\beta\right]\right. \qquad (7)$$
$$\left. + \eta_2\left[N^S_\alpha + \frac{1}{cK}\frac{\partial S}{\partial t}N^K_\alpha\right]\left[N^S_\beta + \frac{1}{cK}\frac{\partial S}{\partial t}N^K_\beta\right]\right\}$$

and the notation $\mathbf{N}^K = [\mathbf{KE}]$, $\mathbf{N}^S = [\nabla S\mathbf{E}]$ is introduced.

As is well known, the condition $\det\|\Pi^{\alpha\beta}\| = 0$ for the existence of nontrivial solutions to this system of equations yields the dispersion equation. In order to represent this equation in explicit tensorial form, we employ formulas of the tensor analysis which were proved in [10, 11]. Following these formulas, we can write out the condition $\det\|\Pi^{\alpha\beta}\| = 0$ in the form

$$2\Pi_{(3)} - 3\Pi_{(1)}\Pi_{(2)} + \Pi^3_{(1)} = 0.$$

Substituting expressions (7) into this equation and dividing the relationship obtained by $\left(\frac{\partial S}{\partial t}\right)^2$, we find

$$\left\{\left(\frac{1}{c}\frac{\partial S}{\partial t}\right)^2 - (\nabla S)^2 + 4\eta_1\xi\mathbf{E}^2\left[\frac{1}{c}\frac{\partial S}{\partial t} + \frac{(\mathbf{K}\nabla S)}{K}\right]^2\right\}$$
$$\times\left\{\left(\frac{1}{c}\frac{\partial S}{\partial t}\right)^2 - (\nabla S)^2 + 4\eta_2\xi\mathbf{E}^2\left[\frac{1}{c}\frac{\partial S}{\partial t} + \frac{(\mathbf{K}\nabla S)}{K}\right]^2\right\} = 0.$$

Thus, depending on the polarization of the weak electromagnetic wave propagating in the field of an intense electromagnetic wave (4), the eikonal in the nonlinear electrodynamics with Lagrangian (1) must satisfy one of the following equations:

$$\left(\frac{1}{c}\frac{\partial S}{\partial t}\right)^2 - (\nabla S)^2 + 4\eta_1\xi\mathbf{E}^2\left[\frac{1}{c}\frac{\partial S}{\partial t} + \frac{(\mathbf{K}\nabla S)}{K}\right]^2 = 0,$$
$$\left(\frac{1}{c}\frac{\partial S}{\partial t}\right)^2 - (\nabla S)^2 + 4\eta_2\xi\mathbf{E}^2\left[\frac{1}{c}\frac{\partial S}{\partial t} + \frac{(\mathbf{K}\nabla S)}{K}\right]^2 = 0. \qquad (8)$$

If $\eta_1 = \eta_2$, then these two equations coincide with one another. This is a situation that takes place in the Born–Infeld electrodynamics in which $\eta_1 = \eta_2 = \frac{a^2B_q^2}{4}$.

Equations (8) are the Hamilton–Jacobi equations

$$g^{nm}\frac{\partial S}{\partial x^n}\frac{\partial S}{\partial x^m} = 0$$

for a massless particle moving in a certain space–time whose metric tensor depends on the field of the strong electromagnetic wave. For the first type of weak electromagnetic waves satisfying the first equation of Eqs. (8), we have

$$g^{00} = 1 + 4\eta_1\xi\mathbf{E}^2, \quad g^{0\alpha} = 4\eta_1\xi\mathbf{E}^2\frac{K^\alpha}{K},$$

$$g^{\alpha\beta} = -\delta^{\alpha\beta} + 4\eta_1\xi\mathbf{E}^2\frac{K^\alpha K^\beta}{K^2}.$$

For the second type of weak electromagnetic waves, we find

$$g^{00} = 1 + 4\eta_2\xi\mathbf{E}^2, \quad g^{0\alpha} = 4\eta_2\xi\mathbf{E}^2\frac{K^\alpha}{K},$$

$$g^{\alpha\beta} = -\delta^{\alpha\beta} + 4\eta_2\xi\mathbf{E}^2\frac{K^\alpha K^\beta}{K^2}.$$

Since the curvature tensor R_{jnml} for the metrics obtained is identically zero, both these four-dimensional spaces are pseudo-Euclidean.

We consider how the properties of these metric tensors depend on the polarization of the strong electromagnetic wave.

For the circularly polarized wave, $\mathbf{E}_1^2 = \mathbf{E}_2^2$. In this case, the components of the metric tensors are independent of the spatial coordinates and time but are not diagonal. This implies that these tensors are metric tensors of inertial reference systems in which the speed of light depends on the propagation direction and polarization of the electromagnetic wave. Therefore, the nonlinear action of a circularly polarized strong electromagnetic wave in vacuum on the propagation of a weak electromagnetic wave is equivalent to the introduction of an anisotropic medium.

For a linearly or elliptically polarized wave, the condition $\mathbf{E}_1^2 \neq \mathbf{E}_2^2$ holds true. In this case, the components of metric tensors are functions of spatial coordinates and time. These components correspond to noninertial reference systems moving in pseudo-Euclidean space–time. Thus, the action of a strong electromagnetic wave which is not circularly polarized on the propagation of a weak electromagnetic wave is equivalent to the introduction of an anisotropic medium and an action of inertia forces of a noninertial reference system in that space region in which these waves interact with one another. This feature can be used as a basis for an experimental search for the manifestation of nonlinearity in the electrodynamics of vacuum.

ACKNOWLEDGMENTS

This work was supported by the Russian Foundation for Basic Research, project no. 00-02-16039.

REFERENCES

1. R. V. Khokhlov, Radiotekh. Élektron. (Moscow) **6**, 917 (1961).
2. S. A. Akhmanov and R. V. Khokhlov, *Nonlinear Optics* (VINITI, Moscow, 1964; Gordon and Breach, New York, 1972).
3. G. E. Stedman, Z. Li, C. H. Rowe, *et al.*, Phys. Rev. A **51**, 4944 (1995).
4. E. B. Aleksandrov, A. A. Ansel'm, and A. N. Moskalev, Zh. Éksp. Teor. Fiz. **89**, 1181 (1985) [Sov. Phys. JETP **62**, 680 (1985)].
5. N. N. Rozanov, Zh. Éksp. Teor. Fiz. **103**, 1996 (1993) [JETP **76**, 991 (1993)].
6. N. N. Rozanov, Zh. Éksp. Teor. Fiz. **113**, 513 (1998) [JETP **86**, 284 (1998)].
7. V. I. Denisov, Phys. Rev. D **61** (3), 036004 (2000).
8. V. I. Denisov, J. Opt. A **2**, 372 (2000).
9. I. M. Ternov, V. R. Khalilov, and V. N. Rodionov, *Interaction of Charged Particles with Strong Electromagnetic Field* (Mosk. Gos. Univ., Moscow, 1982).
10. I. P. Denisova and B. V. Mehta, Gen. Relativ. Gravit. **29**, 583 (1997).
11. I. P. Denisova and M. Dalal, J. Math. Phys. **38**, 5820 (1997).

Translated by G. Merzon

Doklady Physics, Vol. 46, No. 6, 2001, pp. 380–383. Translated from Doklady Akademii Nauk, Vol. 378, No. 4, 2001, pp. 466–469.

PHYSICS

Attenuation of Autowaves

A. Yu. Dovzhenko*, S. V. Maklakov, I. E. Rumanov**, and É. N. Rumanov****

Presented by Academician A.G. Merzhanov January 4, 2001

Received January 10, 2001

If the parameters of an active medium exceed a certain threshold, an autowave propagates uniformly in this medium; otherwise, its amplitude and velocity decrease. In this paper, we derive an approximate equation describing slow autowave-velocity variations. In a near-threshold region, its solutions agree with the results of numerical simulation of an autowave.

1. While studying autowaves, the so-called reaction–diffusion model is widely used. In this model, the width and the velocity of a solitary wave are on the orders of $\sqrt{D\tau_R}$ and $\sim\sqrt{\frac{D}{\tau_R}}$, respectively, where D and τ_R correspond to the diffusion coefficient for a reaction activator and the characteristic time of the relevant chemical reaction. Waves of this type have a propagation threshold (see, e.g., review [1]). When the parameters of the medium exceed the threshold, the autowave problem has two solutions characterized by different wave velocities, the slow wave being unstable. The threshold corresponds to merging of the stable and unstable solutions. Below the threshold, there are no steady-state solutions to the problem; the wave attenuates, and its amplitude and velocity decrease. Near the threshold, the attenuation occurs slowly and an equation describing the slow variations of the wave velocity can be obtained. We now derive this equation considering an exothermal reaction with a high activation energy. However, near the threshold, the equation takes a form that does not contain quantities relevant to a particular reaction and, consequently, applicable to an arbitrary autowave.

A wave of the exothermal reaction propagates due to the heat transfer to an original substance, the wave width and velocity being determined by the thermal diffusivity. The heat release is concentrated in the vicinity of the temperature maximum, i.e., in the reaction zone. Ahead, in the warm-up zone with its relatively low temperature, we may ignore the reaction, while behind, in the cooling zone, the reaction does not proceed because the substance is entirely exhausted. The three-zone structure is characterized by the Zel'dovich number Z and the cooling time τ, where

$$Z = E(T_b - T_0)T_b^{-2}, \quad T_b = T_0 + \frac{Q}{c}.$$

Here, E is the activation energy, Q is the reaction heat, c is the heat capacity, and T_0 is the thermostat temperature. In the case of $Z \gg 1$, the reaction zone is narrow compared to the wave width and, consequently, can be approximately considered as a discontinuity surface for both the heat flow and the diffusion flux [2]. Thus, the wave obeys the equations

$$\frac{\partial n}{\partial t} + u(t)\frac{\partial n}{\partial x} = \frac{\partial^2 n}{\partial x^2} + \varphi\delta(x), \tag{1}$$

$$\frac{\partial T}{\partial t} + u(t)\frac{\partial T}{\partial x} = \frac{\partial^2 T}{\partial x^2} + \varphi\delta(x) - \alpha T, \tag{2}$$

which are written out in the reference system, where the reaction zone is quiescent at $x = 0$ and satisfies the boundary conditions

$$\begin{aligned} x &\longrightarrow -\infty, \quad n = 1, \quad T = 0; \\ x &\longrightarrow \infty, \quad n = 0, \quad T = 0. \end{aligned} \tag{3}$$

The quantities $\tau_R(T_b)$, $\sqrt{\chi\tau_R}$, and $\sqrt{\frac{\chi}{\tau_R}}$ determine the scales of time, length, and velocity, respectively; χ is the thermal diffusivity; n is the concentration of the original substance; T is the temperature counted off from T_0 using the scale $T_b - T_0$; $\alpha = \frac{\tau_R}{\tau}$; $u(t)$ is the instantaneous wave velocity; and

$$\varphi^2 = u_0^2 \exp[-Z(1 - T_m)]. \tag{4}$$

Here, u_0 is the velocity of the wave propagating uniformly at $\alpha = 0$, $u_0 \sim Z^{-1}$, and $T_m = T(x = 0)$. To exclude the complication of the problem due to effects related to the diffusive instability, the diffusivity and the thermal diffusivity are assumed to be equal. System (1)–(4)

* *Landau Institute for Theoretical Physics, Russian Academy of Sciences, Chernogolovka, Moscow oblast, 142432 Russia*

** *Institute of Structural Macrokinetics and Materials Science, Russian Academy of Sciences, Chernogolovka, Moscow oblast, 142432 Russia*

1028-3358/01/4606-0380$21.00

has steady-state solutions at $\alpha < \alpha_{th} \approx u_0^2(2eZ)^{-1}$. For $\alpha = \alpha_{th}$, the difference $1 - T_m \approx Z^{-1} \ll 1$, which justifies the approximate representation of the activation law (4).

According to (1)–(3), the initial conditions already do not affect the solution at times $\sim Z^2$. For $t \gg Z^2$, we can write out that

$$T_m(t) \approx \int_0^t \frac{\varphi(t')}{2\sqrt{\pi(t-t')}} \exp\left[-\frac{l^2(t', t)}{4(t-t')} - \alpha(t-t')\right] dt', \quad (5)$$

where

$$l(t', t) = \int_{t'}^{t} u(t'')dt'', \quad (6)$$

the integrand in (5) being substantially nonzero only within the interval $\sim Z^2$ near the upper limit. According to (1) and (3), we obtain, in the same approximation,

$$\int_0^t \frac{\varphi(t')}{2\sqrt{\pi(t-t')}} \exp\left[-\frac{l^2(t', t)}{4(t-t')}\right] dt' \approx 1. \quad (7)$$

This formula implies the complete conversion of the substance so that $n = 0$ behind the reaction zone. Equalities (4), (5), and (7) allow the quantities u, φ, and T_m to be determined. In the case of uniform wave propagation, $u = \varphi$. Near the threshold, the velocity of the wave varies slowly and the difference between u and φ is not large. Furthermore, everywhere in the integrands of expressions (5) and (7) (except in exponential functions), we use the expansions

$$\varphi(t') \approx \varphi(t) - (t-t')\frac{du}{dt},$$

$$u(t') \approx u(t) - (t-t')\frac{du}{dt}, \quad (8)$$

$$\langle u \rangle \approx u(t) - \left(\frac{t-t'}{2}\right)\frac{du}{dt},$$

where $\langle u \rangle$ is defined by the equality

$$l(t', t) = \langle u \rangle (t-t').$$

Expansions (8) are applicable as long as the difference $t - t'$ is small. However, as was mentioned above, only this variation range of t' essentially contributes to the results of calculating integrals (5) and (7). To perform these calculations, we introduce a new integration variable ξ_1 in (7), which is related to t' by the equality

$$\xi_1^2 = l^2(t', t)[4(t-t')]^{-1}. \quad (9)$$

The integration with respect to ξ_1 should be performed between 0 and $\frac{l(0, t)}{2\sqrt{t}}$. Due to the rapid convergence of the integral, the upper limit can be shifted to infinity. As a result, the left-hand side of (7) takes the form

$$\frac{2}{\sqrt{\pi}} \int_0^\infty \exp(-\xi_1^2)\varphi(\xi_1)[2u(\xi_1) - \langle u \rangle]^{-1} d\xi_1. \quad (10)$$

We now simplify the multiplier ahead of the exponential function in (10), retaining only those terms that contain the derivative $\frac{du}{dt}$ with a power not exceeding the first one. As a result, this multiplier takes the form

$$1 + u_{th}^{-1}\left[\varphi(t) - u(t) + 2\xi_1^2 u_{th}^{-2}\frac{du}{dt}\right]. \quad (11)$$

Here, the instantaneous and average velocities are replaced by the threshold velocity $u_{th} = u(\alpha_{th})$ everywhere except in the small difference $\varphi - u$. Substituting (10) and (11) into (7), we find

$$u - \varphi \approx u_{th}^{-2}\frac{du}{dt}. \quad (12)$$

Furthermore, we perform similar transformations in the integrand of expression (5). Replacing the integration variable $t' \longrightarrow \xi_2$ according to the formula

$$\xi_2^2 = l^2(t', t)[4(t-t')]^{-1} + \alpha(t-t') \quad (13)$$

and using both expansions (8) and the linearization in $\frac{du}{dt}$, we arrive at the relation

$$T_m(t) - \frac{\varphi}{\sqrt{\varphi^2 + 4\alpha}} \approx -\frac{6}{Zu_{th}^3}\frac{du}{dt}. \quad (14)$$

Using relation (4), we can now express the temperature T_m in terms of φ and then replace φ in (14) by u. Indeed, according to (12), the difference $\varphi - u$ is proportional to $\frac{du}{dt}$. However, in this case, a correction $\sim\frac{du}{dt}(u - u_{th})$ arises in (14) which can be ignored near the threshold. Retaining terms leading with respect to $u - u_{th}$ and $\alpha - \alpha_{th}$ in the left-hand side of this equality, we derive the following equation for the velocity:

$$\frac{du}{dt} \approx -\frac{u_{th}^3}{3}\left[\frac{\alpha - \alpha_{th}}{2\alpha_{th}} + \left(\frac{u}{u_{th}} - 1\right)^2\right]. \quad (15)$$

As is seen, this equation contains only u_{th} and α_{th} as parameters and, consequently, is applicable to any autowave having a propagation threshold. At $\alpha < \alpha_{th}$, there exist two solutions characterized by constant velocity, the slow branch being unstable. At $\alpha > \alpha_{th}$, the velocity decreases with time and the wave attenuates.

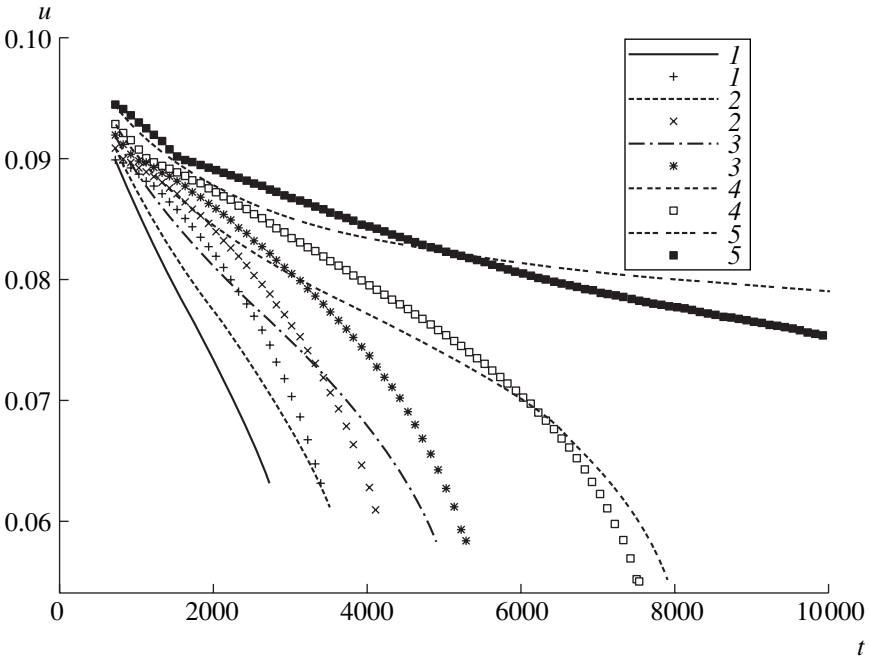

Attenuation curves for an autowave under near-threshold conditions. The values of $\alpha \times 10^4$ are (*1*) 3.0, (*2*) 2.9, (*3*) 2.8, (*4*) 2.7, and (*5*) 2.6.

As long as $(\alpha - \alpha_{th}) \ll \alpha_{th}$, the deceleration becomes small as the velocity approaches u_{th}. This stage of slow variations is typical for the development of the explosive instability near the limit (see [3]) and for chaotic regimes with intermittency [4]. In accordance with Eq. (15), the function $u(t)$ is determined by the equality

$$t = \frac{3}{u_{th}^2}\sqrt{\frac{2\alpha_{th}}{\alpha - \alpha_{th}}}\left[\arctan\left(\frac{u_i - u_{th}}{u_{th}}\sqrt{\frac{2\alpha_{th}}{\alpha - \alpha_{th}}}\right)\right.$$
$$\left. - \arctan\left(\frac{u - u_{th}}{u_{th}}\sqrt{\frac{2\alpha_{th}}{\alpha - \alpha_{th}}}\right)\right]. \quad (16)$$

Here, $u_i = u(t = 0)$ so that the characteristic attenuation time is $\sim u_{th}^{-2}\sqrt{\frac{\alpha_{th}}{\alpha - \alpha_{th}}}$.

2. For numerical simulation of an autowave, we used the system of equations

$$\frac{\partial \eta}{\partial t} + u\frac{\partial \eta}{\partial x} = \frac{\partial^2 \eta}{\partial x^2} + (1 - \eta)\exp\left(\frac{\theta}{1 + \beta\theta}\right), \quad (17)$$

$$\frac{\partial \theta}{\partial t} + u\frac{\partial \theta}{\partial x}$$
$$= \frac{\partial^2 \theta}{\partial x^2} + Z(1 - \eta)\exp\left(\frac{\theta}{1 + \beta\theta}\right) - \alpha(\theta + Z) \quad (18)$$

within the interval $0 < x < x_0$ ($x_0 = 300$). The boundary conditions were taken to be

$$x = 0, \quad \frac{\partial \eta}{\partial x} = u\eta, \quad \frac{\partial \theta}{\partial x} = \left(\frac{u}{2} + \sqrt{\frac{u^2}{4} + \alpha}\right)(\theta + Z);$$
$$x = x_0, \quad \frac{\partial \eta}{\partial x} = \frac{\partial \theta}{\partial x} = 0. \quad (19)$$

The calculations were carried out assuming that $Z = 10$ and $\beta = 0.09$; the steps in variables x and t are equal to 0.1 and 0.2, respectively. Distributions schematically representing a wave with the reaction zone at $x = x_1 = \frac{x_0}{3}$ were used as initial conditions:

$$x < x_1, \quad \eta = \exp[u_i(x - x_1)],$$
$$\theta + Z = Z\exp[(u_i + \alpha u_i^{-1})(x - x_1)];$$
$$x > x_1, \quad \eta = 1, \quad \theta + Z = Z\exp[-\alpha u_i^{-1}(x - x_1)],$$

where u_i is the initial velocity. Furthermore, the value of u was chosen in a manner which made it possible to retain the maximum of the function $\exp\frac{\theta}{1 + \beta\theta}$ at the point x_m situated not far from $\frac{x_0}{3}$. At the nth time step, the value of u was calculated by the formula (corrector)

$$u_n = u_i + \omega\left[\frac{x_0}{3} - (x_m)_{n-1}\right], \quad (20)$$

where $\omega = 6\frac{u_i}{x_0}$ for $x_m < \frac{x_0}{3}$ and $\omega = \frac{3u_i}{2x_0}$ for $x_m > \frac{x_0}{3}$.

For a number of values of α, the function $u(t)$ calculated in this way was compared with the solutions to Eq. (15). The values of u_{th}, α_{th}, and u_0 were calculated in the course of numerical experiments based on system (17)–(19). These values turned out to be $\alpha_{th} \approx 0.000259$ and $u_{th} \approx 0.08$, i.e., coinciding at $u_0 \approx 0.1276$ with the known asymptotic estimations (see [5]) within an accuracy to $\sim\frac{1}{Z}$.

The attenuation curves are plotted in the figure. The results calculated by formula (16) are shown by solid lines, while the data of the numerical simulation obtained with the step $\Delta t = 100$ are represented by dots. The initial time interval ($t \sim Z^2$), inside which the wave-structure formation occurs, is excluded from the plots. We can see the qualitative agreement between the solutions to Eq. (15) with the results of the numerical simulation. In particular, there exists, in each curve, an inflection point at $u \approx u_{th}$. The closer α is to α_{th}, the longer the stage of a slower decrease in the velocity. However, in contrast to the calculations based on Eq. (15), the numerical simulation can reveal an irregular wave behavior near the threshold. Such a behavior is caused by a "random" rounding-off during the calculation process. Far from the threshold, the effect of random rounding-off is insignificant. As α approaches α_{th}, the susceptibility of a wave to external actions increases infinitely. Since, under actual conditions, there always exist random variations of parameters (noise), the fluctuation region with chaotic wave propagation therein must be adjacent to the threshold. The description of the fluctuation region is beyond the scope of this paper and will be presented later.

ACKNOWLEDGMENTS

This work was supported by the Russian Foundation for Basic Research, project no. 98–03–32132.

REFERENCES

1. A. G. Merzhanov and E. N. Rumanov, Rev. Mod. Phys. **71**, 1173 (1999).
2. Ya. B. Zel'dovich, Zh. Éksp. Teor. Fiz. **11**, 159 (1941).
3. A. G. Merzhanov, V. V. Barzykin, and V. G. Abramov, Khim. Fiz. **15** (6), 3 (1996).
4. P. Manneville and Y. Pomeau, Physica D (Amsterdam) **1**, 219 (1980).
5. D. A. Frank-Kamenetskiĭ, *Diffusion and Heat Transfer in Chemical Kinetics* (Nauka, Moscow, 1987).

Translated by Yu. Verevochkin

Doklady Physics, Vol. 46, No. 6, 2001, pp. 384–388. Translated from Doklady Akademii Nauk, Vol. 378, No. 4, 2001, pp. 470–474.

PHYSICS

Polya Hypothesis and Variational Inequalities for Polarizabilities of Dielectric Bodies

V. P. Kazantsev

Presented by Academician A.F. Andreev February 8, 2001

Received January 18, 2001

INTRODUCTION

New alternative inequalities for the polarizability tensor of a homogeneous dielectric body are obtained. As special cases, the well-known inequalities proposed by Polya follow from these inequalities. A possible practical implementation of the inequalities found is demonstrated by example.

The polarizability tensor $\hat{\alpha}$ of a dielectric particle relates its dipole moment $\mathbf{p}$ induced by a uniform external electric field to the field intensity $\mathbf{E}_0$ by the formula [1]

$$\mathbf{p} = \hat{\alpha}\mathbf{E}_0. \quad (1)$$

If the particle is homogeneous and its material is characterized by a symmetric positive-definite permittivity tensor $\hat{\varepsilon}$, then $\hat{\alpha}$ depends on $\hat{\varepsilon}$ and particle geometric parameters.

For $\hat{\varepsilon} = \infty$, $\hat{\alpha}(\infty)$ determines the polarizability tensor $\hat{\alpha}_c$ of a conducting particle having the same shape as the dielectric particle. The quantity $\hat{\alpha}(0)$ differs from the magnetic polarizability tensor $\hat{\alpha}_m$ of a superconducting particle of the same shape by a constant factor only. We recall that, in the case when a superconducting particle is placed in an external magnetic field of intensity $\mathbf{H}_0$, this field induces a magnetic moment on the particle:

$$\mathbf{m} = \hat{\alpha}_m\mathbf{H}_0.$$

In SI units, $\hat{\alpha}(0) = \varepsilon_0\hat{\alpha}_m$.

The exact solution to the problem of the polarizability tensor is known only for a uniform dielectric ellipsoid,

$$\hat{\alpha} = \varepsilon_0 V[(\hat{\varepsilon} - \varepsilon_0\hat{e})\hat{N} + \varepsilon_0\hat{e}]^{-1}(\hat{\varepsilon} - \varepsilon_0\hat{e}). \quad (2)$$

Here, $\hat{N}$ is the ellipsoid depolarization tensor [1], $\hat{e}$ is the unit tensor, and V is the ellipsoid volume. In particular, as follows from (2),

$$\hat{\alpha}_c = \varepsilon_0 V\hat{N}^{-1}, \quad \hat{\alpha}_m = -V(\hat{e} - \hat{N})^{-1}. \quad (3)$$

All tensors introduced here are symmetric; $\hat{\alpha}_c$ and $\hat{N}$ are positive definite, and $\hat{\alpha}_m$ is negative definite. The trace of the $\hat{N}$-tensor is equal to unity:

$$\mathrm{Sp}\,\hat{N} = 1. \quad (4)$$

The problem of finding the polarizability tensor is intricate. Therefore, variational-estimate methods were found interesting for use in practical calculations. The first such estimates (formulated as hypotheses) were the inequalities

$$\frac{1}{3}\mathrm{Sp}\,\hat{\alpha}_c \geq 3\varepsilon_0 V, \quad \frac{1}{3}\mathrm{Sp}\,\hat{\alpha}_m \leq -\frac{3}{2}V \quad (5)$$

known as the Polya hypotheses [2]. Proofs of two-dimensional analogs for these inequalities were given in [2]. The inequalities, in themselves, were proved much later, in [3, 4].

The extension of inequalities (5) to problems on the polarizability of dielectric bodies was given in [5–7]. The essential achievement of these papers consisted in generalization of the depolarization-tensor concept (usually defined only for ellipsoids) to bodies of arbitrary shape. This generalization resulted from the formula

$$\langle\mathbf{E}\rangle_V = -\frac{1}{\varepsilon_0}\hat{N}\mathbf{P},$$

which relates the mean (over the region V) intensity of the electric field to the uniform polarization $\mathbf{P}$ of the region V that produces this field. The tensor $\hat{N}$ is positive definite and symmetric, and its trace is equal to unity. Elements of a matrix representing $\hat{N}$ in a certain coordinate system can be found from the formula

$$N_{ij} = \frac{1}{4\pi V}\int_{\partial V}\int_{\partial V}\frac{n_i(\mathbf{r})n_j(\mathbf{r}')}{|\mathbf{r} - \mathbf{r}'|}dS'dS. \quad (6)$$

Krasnoyarsk State University,
pr. Svobodnyĭ 79, Krasnoyarsk, 660062 Russia

1028-3358/01/4606-0384$21.00

Here, $n_i(\mathbf{r})$ are the components of the unit vector normal to the surface ∂V at the point $\mathbf{r}$. Using formula (2) and finding the depolarization tensor for an arbitrary body, we can calculate the polarizability tensor for a dielectric ellipsoid with the same volume, the same depolarization tensor, and the same permittivity tensor. We denote this polarizability tensor by $\hat{\alpha}_e(\hat{\varepsilon}, \hat{N}, V)$. The following inequalities are proven in [5, 7]:

$$\begin{aligned} \hat{\alpha} &\geq \hat{\alpha}_e(\hat{\varepsilon}, \hat{N}, V) \quad \text{for} \quad \hat{\varepsilon} \geq \varepsilon_0 \hat{e}, \\ \hat{\alpha} &\leq \hat{\alpha}_e(\hat{\varepsilon}, \hat{N}, V) \quad \text{for} \quad \hat{\varepsilon} \leq \varepsilon_0 \hat{e}. \end{aligned} \tag{7}$$

In particular, the inequalities

$$\hat{\alpha}_c \geq \varepsilon_0 V \hat{N}^{-1}, \quad \hat{\alpha}_m \leq -V(\hat{e} - \hat{N})^{-1}$$

follow from these inequalities for $\hat{\varepsilon} \longrightarrow \infty$ and $\hat{\varepsilon} \longrightarrow 0$ and, as was demonstrated in [6], inequalities (5). Estimates (7) were applied in [5, 7] to calculate cross sections for the scattering of electromagnetic waves by small dielectric particles.

It is worth noting that inequalities (7) provide a method of obtaining either the upper or lower bound for the polarizability tensor, whereas principles [8] of the variational dielectric electrostatics make it possible to obtain two-sided estimates. This is very convenient, because, having at hand the two-sided estimates along with an approximate value of the polarizability tensor, the maximum error for this approximation can be found. This brings up a question: is it possible to find alternative inequalities for (7)? The goal of this paper is to find such inequalities.

VARIATIONAL PRINCIPLES AND THE PROBLEM OF POLARIZABILITY

We assume that a dielectric particle occupies a region of space V and its material is characterized by a field of the positive-definite symmetric permittivity tensor $\hat{\varepsilon}(\mathbf{r})$. The electric field $\mathbf{E}_{out}(\mathbf{r})$ produced by external sources polarizes the particle. The polarization $\mathbf{P}(\mathbf{r})$ induced by the external field serves as a source of the electric field $\mathbf{E}(\mathbf{r})$, whose scalar potential is

$$\varphi(\mathbf{r}) = \frac{1}{4\pi\varepsilon_0}\int_V \frac{\mathbf{P}(\mathbf{r}') \cdot (\mathbf{r} - \mathbf{r}')}{|\mathbf{r} - \mathbf{r}'|^3} dV'. \tag{8}$$

The corresponding electric induction can be expressed in terms of the vector potential

$$\mathbf{A}(\mathbf{r}) = \frac{1}{4\pi}\int_V \frac{\mathbf{P}(\mathbf{r}') \cdot (\mathbf{r} - \mathbf{r}')}{|\mathbf{r} - \mathbf{r}'|^3} dV' \tag{9}$$

by the formula

$$\mathbf{D} = \nabla \times \mathbf{A}.$$

The quantities $\mathbf{E} = -\nabla\varphi$, $\mathbf{D}(\mathbf{r})$, and $\mathbf{P}(\mathbf{r})$ are bound by the relation

$$\mathbf{D}(\mathbf{r}) = \varepsilon_0 \mathbf{E}(\mathbf{r}) + \mathbf{P}(\mathbf{r}). \tag{10}$$

Solving the fundamental problem of electrostatics for a dielectric body placed in an external electric field implies finding the unknowns $\mathbf{E}(\mathbf{r})$, $\mathbf{D}(\mathbf{r})$, and $\mathbf{P}(\mathbf{r})$ from the known quantity $\mathbf{E}_{out}(\mathbf{r})$.

The general scheme for solving this problem, which employs the concept of characteristic multipoles and higher polarizabilities for a dielectric particle, is constructed in [9] on the basis of variational principles. These principles are conveniently represented in the form of inequalities:

$$\begin{aligned} -L(\mathbf{A}) &\leq -L(\mathbf{A}_0) \\ &= \frac{1}{2}\int_V \mathbf{P}_0(\mathbf{r}) \cdot \mathbf{E}_{out}(\mathbf{r}) dV = W(\varphi_0) \leq W(\varphi). \end{aligned} \tag{11}$$

Here, the true field distributions are marked by the subscript 0 to distinguish them from the tentative ones. Continuous piecewise smooth potentials $\varphi(\mathbf{r})$ and $\mathbf{A}(\mathbf{r})$ are admissible in the functionals

$$\begin{aligned} W(\varphi) &= \frac{1}{2}\int (\varepsilon_0 (\nabla\varphi)^2 \\ &+ (\mathbf{E}_{out} - \nabla\varphi)(\hat{\varepsilon} - \varepsilon_0 \hat{e})(\mathbf{E}_{out} - \nabla\varphi)) dV, \end{aligned} \tag{12}$$

$$\begin{aligned} L(\mathbf{A}) &= \frac{1}{2\varepsilon_0}\int (\mathbf{D}^2 + (\mathbf{D} + \varepsilon_0 \mathbf{E}_{out}) \\ &\times (\varepsilon_0 \hat{\varepsilon}^{-1} - \hat{e})(\mathbf{D} + \varepsilon_0 \mathbf{E}_{out})) dV, \\ \mathbf{D} &= \nabla \times \mathbf{A}. \end{aligned} \tag{13}$$

In particular, potentials (8) and (9), found for a certain tentative polarization distribution $\mathbf{P}(\mathbf{r})$, can be taken tentatively as $\varphi(\mathbf{r})$ and $\mathbf{A}(\mathbf{r})$.

From the viewpoint of the general approach developed in [9], the problem of the polarizability tensor for a dielectric particle is a problem of the characteristic multipoles of the first order. In this case, the homogeneous electric field $\mathbf{E}_0$ should be used instead of $\mathbf{E}_{out}(\mathbf{r})$ by taking, in relations (11)–(13),

$$\mathbf{E}_{out}(\mathbf{r}) = \mathbf{E}_0.$$

With allowance for relation (1), we can write out

$$\int_V \mathbf{P}_0(\mathbf{r}) \cdot \mathbf{E}_0 dV = \mathbf{E}_0 \cdot \hat{\alpha} \cdot \mathbf{E}_0$$

and use inequality (11) for determining the boundaries in which the value of the tensor $\hat{\alpha}$ can be confined.

The choice of a tentative function is the basic problem of realizing the method of variational inequalities. In solving this problem, physical considerations can play an essential role. It is worth noting that solving this problem for an isolated conductor [10] turned out to be

equivalent to solving the fundamental problem of electrostatics. However, here, we deal with relatively simple tentative functions. Therefore, the estimates obtained have a rather wide field of application.

THE APPROXIMATION OF THE DIELECTRIC-PARTICLE POLARIZATION BY UNIFORM POLARIZATION

An external homogeneous electric field polarizes a homogeneous anisotropic dielectric ellipsoid so that a homogeneous polarization arises in its volume. This can be verified by substituting the potentials determined from formulas (8) and (9) into variational inequalities (11) under the condition of a homogeneous distribution $\mathbf{P}(\mathbf{r})$ inside the ellipsoid for $\varphi(\mathbf{r})$ and $\mathbf{A}(\mathbf{r})$. In this case, $W(\varphi)$ and $W(\mathbf{A})$ turn into quadratic forms in components of $\mathbf{P}$. Minimizing these forms with respect to $\mathbf{P}$, we arrive at the solution to the problem on a homogeneous dielectric ellipsoid in a homogeneous external electric field. A question naturally arises: can a homogeneous polarization be a reasonable approximation for the true polarization of homogeneous dielectric particles whose shape differs (possibly, very essentially) from an ellipsoid? Variational inequalities (11) make it possible to answer this question for different bodies.

We substitute $\varphi(\mathbf{r})$ determined by relation (8) into functional (12) under the condition of homogeneous polarization distribution over the volume of a dielectric particle. Then, for the integral of the first term in integrand (12), we obtain

$$\frac{1}{2}\varepsilon_0\int(\nabla\varphi)^2 dV = \frac{V}{2\varepsilon_0}\mathbf{P}\cdot\hat{N}\cdot\mathbf{P}.$$

The depolarization tensor $\hat{N}$ of the region V is specified by formula (6).

For calculating the integral of the second term in integrand (12), we notice that, in the region occupied by a particle,

$$\mathbf{E}(\mathbf{r}) = -\frac{1}{4\pi\varepsilon_0}\nabla\int\limits_{\partial V}\frac{n(\mathbf{r}')}{|\mathbf{r}-\mathbf{r}'|}dS'\cdot\mathbf{P} = -\frac{1}{\varepsilon_0}\hat{n}(\mathbf{r})\cdot\mathbf{P}. \quad (14)$$

It is reasonable to call $\hat{n}(\mathbf{r})$ the local depolarization tensor. This tensor is symmetric, and its trace is equal to unity. However, unlike the depolarization tensor of the region

$$\hat{N} = \langle\hat{n}(\mathbf{r})\rangle_V = \frac{1}{V}\int\limits_V\hat{n}(\mathbf{r})dV,$$

the local tensor $\hat{n}(\mathbf{r})$ can be not positive definite in certain parts of the region V. For example, if the region V consists of two equal touching balls centered at the points R_1 and R_2, then, at the point of tangency,

$$\hat{n}\left(\frac{R_1+R_2}{2}\right) = \frac{2}{3}\hat{e} - \frac{(R_1-R_2)(R_1-R_2)}{|R_1-R_2|^2}.$$

We introduce the following notation for positive-definite symmetric tensors of the second rank:

$$\hat{\mathbf{E}} = \frac{1}{\varepsilon_0}\langle\hat{n}(\mathbf{r})\cdot\hat{\varepsilon}\cdot\hat{n}(\mathbf{r})\rangle_V, \quad \hat{m} = \langle\hat{n}(\mathbf{r})\cdot\hat{n}(\mathbf{r})\rangle_V. \quad (15)$$

Then,

$$W(\varphi) = \frac{V}{2\varepsilon_0}\mathbf{P}\cdot(\hat{N}+\hat{E}-\hat{m})\cdot\mathbf{P}$$

$$-\frac{V}{\varepsilon_0}\mathbf{P}\cdot\hat{N}\cdot(\hat{\varepsilon}-\varepsilon_0\hat{e})\cdot\mathbf{E}_0 + \frac{V}{2}\mathbf{E}_0\cdot(\hat{\varepsilon}-\varepsilon_0\hat{e})\cdot\mathbf{E}_0.$$

Minimizing the expression obtained for the functional $W(\varphi)$ with respect to $\mathbf{P}$, we arrive at a tensor $\hat{\alpha}_s$ representing the upper bound for the tensor $\hat{\alpha}$; i.e.,

$$\hat{\alpha}\le\hat{\alpha}_s = V(\hat{\varepsilon}-\varepsilon_0\hat{e})$$
$$\times\left(\hat{e}-\frac{1}{\varepsilon_0}\hat{N}(\hat{N}+\hat{E}-\hat{m})^{-1}\hat{N}(\hat{\varepsilon}-\varepsilon_0\hat{e})\right). \quad (16)$$

We recall that tensor inequality (16) implies the positive definiteness of the tensor $\hat{\alpha}_s-\hat{\alpha}$.

It is worth noting that from inequality (16) for $\hat{\varepsilon} < \varepsilon_0\hat{e}$, the second inequality of relations (7) follows. The passage to this inequality is realized by replacing the tensor $\hat{E}-\hat{m}$ by the larger tensor $\hat{N}(\hat{\varepsilon}-\varepsilon_0\hat{e})\hat{N}$. Inequality (7) is weaker than inequality (16). For $\hat{\varepsilon} > \varepsilon_0\hat{e}$, such a replacement cannot be done since $\hat{E}-\hat{m} > \hat{N}(\hat{\varepsilon}-\varepsilon_0\hat{e})\hat{N}$.

To obtain the lower bound for the polarizability tensor, we substitute the vector potential $\mathbf{A}(\mathbf{r})$ from relation (9) into functional $L(\mathbf{A})$ (13) and assume that the polarization is uniformly distributed over the dielectric-body volume. When calculating values of $L(\mathbf{A})$, we employ the relation

$$\mathbf{D}(\mathbf{r}) = (\hat{e}-\hat{n}(\mathbf{r}))\cdot\mathbf{P} \text{ for } \mathbf{r}\in V. \quad (17)$$

Using (17), we find

$$L(\mathbf{A}) = \frac{V}{2\varepsilon_0}\mathbf{P}\cdot(\hat{e}-\hat{N}+\hat{F}-\hat{K})\cdot\mathbf{P} - V\mathbf{P}$$

$$\times(\hat{e}-\hat{N})(\hat{e}-\varepsilon_0\hat{\varepsilon}^{-1})\cdot\mathbf{E}_0 - \frac{\varepsilon_0}{2}V\mathbf{E}_0\cdot(\hat{e}-\varepsilon_0\hat{\varepsilon}^{-1})\cdot\mathbf{E}_0,$$

where

$$\hat{F} = \varepsilon_0\left\langle(\hat{e}-\hat{n}(\mathbf{r}))\hat{\varepsilon}^{-1}(\hat{e}-\hat{n}(\mathbf{r}))\right\rangle_V, \quad (18)$$

$$\hat{K} = \left\langle (\hat{e} - \hat{n}(\mathbf{r}))^2 \right\rangle_V = \hat{e} - 2\hat{N} + \hat{m}. \quad (19)$$

Minimizing the value of the functional $L(\mathbf{A})$ with respect to $\mathbf{P}$, we obtain the lower bound $\hat{\alpha}_i$ for the dielectric-particle polarizability tensor:

$$\hat{\alpha} \geq \hat{\alpha}_i = V\varepsilon_0(\hat{e} - \varepsilon_0\hat{\varepsilon}^{-1})(\hat{e} + (\hat{e} - \hat{N}) \times (\hat{e} - \hat{N} + \hat{F} - \hat{K})^{-1}(\hat{e} - \hat{N})(\hat{e} - \varepsilon_0\hat{\varepsilon}^{-1}). \quad (20)$$

Inequality (20) combined with inequality (16) allows us not only to find an approximate value of the polarizability tensor but also to determine the maximum error of this approximation.

The first inequality of (7) follows from inequality (20) provided that the condition $\hat{\varepsilon} > \varepsilon_0\hat{e}$ holds. To pass to this inequality, the tensor $\hat{F} - \hat{K}$ should be replaced by the larger tensor

$$(\hat{e} - \hat{N})(\hat{e} - \varepsilon_0\hat{\varepsilon}^{-1})(\hat{e} - \hat{N}).$$

Inequality (20) is more rigorous than the first inequality of (7). For $\hat{\varepsilon} < \varepsilon_0\hat{e}$, such a replacement is impossible since

$$\hat{F} - \hat{K} < (\hat{e} - \hat{N})(\hat{e} - \varepsilon_0\hat{\varepsilon}^{-1})(\hat{e} - \hat{N})$$

and the inequality can, generally speaking, change its direction after the replacement.

The inequalities

$$\hat{\alpha}_c \geq V\varepsilon_0(\hat{e} + ((\hat{e} - \hat{N})^{-1} - (\hat{e} - \hat{N})^{-1}\hat{K}(\hat{e} - \hat{N})^{-1})^{-1}),$$

$$\hat{\alpha}_m \leq -V(\hat{e} + (\hat{N}^{-1} + (\hat{N}^{-1} - \hat{N}^{-1}\hat{m}\hat{N}^{-1})^{-1}),$$

which improve the well-known inequalities, can also be written out for the polarizability tensor of a conductor and the magnetic-polarizability tensor of a superconductor that have the same shape as a dielectric particle, while using inequalities (16) and (20).

AN EXAMPLE

We apply the results obtained to estimate the linear polarizabilities of two equal parallel infinite cylinders with circular cross sections of radius a and an axis-to-axis distance $l \geq 2a$, the cylinder material being homogeneous and isotropic. For such a problem, the following expressions should be substituted into inequalities (16) and (20):

$$\hat{E} - \hat{m} = \frac{\varepsilon - \varepsilon_0}{\varepsilon_0}\hat{m}, \quad \hat{F} - \hat{K} = \frac{\varepsilon_0 - \varepsilon}{\varepsilon}\hat{K}:$$

$$V = 2\pi a^2, \quad \hat{N} = \frac{1}{2}(1 - \delta)\mathbf{ii} + \frac{1}{2}(1 + \delta)\mathbf{jj}, \quad \delta = \frac{a^2}{l^2},$$

$$\hat{m} = \left(\frac{1}{4}(1 - \delta)^2 + \Delta\right)\mathbf{ii} + \left(\frac{1}{4}(1 + \delta)^2 + \Delta\right)\mathbf{jj},$$

$$\Delta = \frac{\delta^3(2 - \delta)}{4(1 - \delta)^2}.$$

Here, $\mathbf{i}$ is the unit vector of a straight line intersecting the cylinder axes and is orthogonal to them and $\mathbf{j}$ is the unit vector which is orthogonal to the cylinder axes and to the vector $\mathbf{i}$. As a result of this substitution, we arrive at the following expressions:

$$\frac{\hat{\alpha}_s}{2\pi\varepsilon_0 a^2} = \frac{F(2(1 - \delta) + 4F\Delta)}{2(1 - \delta) + F((1 - \delta)^2 + 4\Delta)}\mathbf{ii} + \frac{F(2(1 + \delta) + 4F\Delta)}{2(1 + \delta) + F((1 + \delta)^2 + 4\Delta)}\mathbf{jj},$$

$$\frac{\hat{\alpha}_i}{2\pi\varepsilon_0 a^2} = \frac{G(2(1 + \delta) - 4G\Delta)}{2(1 + \delta) - G((1 + \delta)^2 + 4\Delta)}\mathbf{ii} + \frac{G(2(1 - \delta) - 4G\Delta)}{2(1 - \delta) - G((1 - \delta)^2 + 4\Delta)}\mathbf{jj},$$

where

$$F = \frac{\varepsilon - \varepsilon_0}{\varepsilon_0}, \quad G = \frac{\varepsilon - \varepsilon_0}{\varepsilon}.$$

In particular, for $\varepsilon = 2\varepsilon_0$, $l = 2a$ (the cylinders are in contact),

$$\frac{\hat{\alpha}_s}{2\pi\varepsilon_0 a^2} = \frac{223}{304}\mathbf{ii} + \frac{367}{592}\mathbf{jj} = 0.73356\mathbf{ii} + 0.61993\mathbf{jj},$$

$$\frac{\hat{\alpha}_i}{2\pi\varepsilon_0 a^2} = \frac{713}{976}\mathbf{ii} + \frac{425}{688}\mathbf{jj} = 0.73053\mathbf{ii} + 0.61773\mathbf{jj}.$$

The example considered demonstrates that the estimates determined by inequalities (16) and (20) can be rather exact.

CONCLUSIONS

We note that inequalities (16) and (20), which express the principal results of the paper, are transformed into equalities in the case of a homogeneous dielectric ellipsoid. Thus, the field-source distributions that result in an exact solution to variational problem (11)–(13) of the polarizability for a dielectric ellipsoid are used in this paper as tentative (basis) ones for constructing estimates of polarizability for arbitrary-shape dielectric bodies. The complete analysis of the corresponding variational problems is carried out. Further extension of the basis of tentative functions and improvement of the variational estimates for the polarizability tensor can be achieved by employing the characteristic-multipole technique developed in [10].

REFERENCES

1. L. D. Landau and E. M. Lifshitz, *Course of Theoretical Physics*, Vol. 8: *Electrodynamics of Continuum* (Nauka, Moscow, 1982; Pergamon, New York, 1984).
2. G. Pólya and G. Szegö, *Izoperimetric Inequalities in Mathematical Physics* (Princeton Univ. Press, Princeton, 1951; Fizmatgiz, Moscow, 1962).
3. M. Shiffer, C. R. Acad. Sci., Ser. 13 **244**, 3118 (1975).
4. A. L. Berdichevskiĭ and V. L. Berdichevskiĭ, Dokl. Akad. Nauk SSSR **224**, 313 (1975) [Sov. Phys. Dokl. **20**, 614 (1975)].
5. V. P. Kazantsev, Izv. Vyssh. Uchebn. Zaved., Radiofiz. **23**, 635 (1980).
6. V. P. Kazantsev, Zh. Tekh. Fiz. **53**, 449 (1983) [Sov. Phys. Tech. Phys. **28**, 282 (1983)].
7. V. P. Kazantsev, Izv. Vyssh. Uchebn. Zaved., Radiofiz. **25**, 1501 (1982).
8. V. P. Kazantsev, Zh. Tekh. Fiz. **49**, 2559 (1979) [Sov. Phys. Tech. Phys. **24**, 1446 (1979)].
9. V. P. Kazantsev, Available form VINITI No. 627-V99 (Krasnoyarsk, 1999).
10. V. P. Kazantsev, Teor. Mat. Fiz. **119**, 441 (1999).

Translated by V. Tsarev

Doklady Physics, Vol. 46, No. 6, 2001, pp. 389–392. Translated from Doklady Akademii Nauk, Vol. 378, No. 4, 2001, pp. 475–478.

PHYSICS

A Minimum of the Lattice Vibration Frequency as a Function of the Electrostatic Field and the Soft-Mode Concept

A. Leyderman*, O. E. Fesenko, S. P. Hernández-Rivera***, and Corresponding Member of the RAS E. E. Fesenko******

Received January 1, 2001

Our objective is to test experimentally the applicability of the contemporary physical theory to the description of the crystal state of a material subjected to the effect of an electrostatic field whose strength is close to the value of the electrical breakdown field.

The concept of a soft mode [1], which is equivalent to the Landau theory [2], covers an extensive class of phase transitions that occur under changes of temperature, pressure, and magnetic field. The only exception to this class was, to date, phase transitions proceeding under the action of an external electrostatic field. This theory was not verified for such transitions owing to the difficulties in achieving an electric field strength exceeding 15×10^6 V/m. We studied the field-induced phase transition using the Raman-scattering method and revealed a quasisoft behavior of one of the lattice vibrations: the spectral line frequency does not vanish at the point of the phase transition, as was postulated in the theory, but attains a minimum. A revealed similarity of the phase transition to a soft-mode one indicates that the phase transitions occurring under a change of electric field fit the ideas of the soft-mode concept and the Landau theory, can be described on their basis, and confirm their universal character.

In an antiferroelectric (AFE) crystal $PbZrO_3$ (lead zirconate), an external electrostatic field induces three phase transitions in electric fields with a strength up to 5×10^7 V/m [3, 4]. Studies carried out by the methods of X-ray diffraction and spectroscopy [5] and by the method of electron spin resonance [6] have shown that the observed phase transitions are associated with modification of the crystal symmetry and that $PbZrO_3$ is more convenient to use when searching for regularities in the atomic-structure dynamics in electric fields than any other crystal.

Experiments on Raman scattering in crystals have been limited so far to fields up to 5×10^6 V/m. We have studied Raman scattering in $PbZrO_3$ in electric fields up to 28×10^6 V/m. Raman scattering spectra were obtained with a T64000 spectrograph using excitation by argon laser radiation (λ = 514.5 nm, 20 mW, 5 min) and an original method of applying an electric field described elsewhere [7].

The general shape of the spectrum (Fig. 1) differs from that reported in [8] by the presence of additional lines with frequencies of 22.9 and 28.4 cm^{-1}. On applying the electric field to a crystal, we observe a shift of the line with a frequency of 233 cm^{-1} (Fig. 2), the appearance of a new line at 673 cm^{-3}, and a change in the intensity of other lines.

We will consider in detail the dependence of the line position on the electric field. In the absence of the field (Fig. 3), this line is positioned at 233 cm^{-1}. The frequency dependence of this line on the field has a weak maximum in the region of 10^6 V/m. Near this field strength, changes in the intensity of the lines 22.9, 28.4, and 35.8 cm^{-1} are observed and a new line with a frequency of 673 cm^{-1} appears. The intensity of the latter rises with further increase in the field strength. The minimum of the function $\omega(E)$ is observed for the electric field strength $E = 239.5 \times 10^5$ V/m, near which the crystal undergoes a phase transition from the antiferroelectric (AFE) phase, whose lattice belongs to the *Pbam* space group, into a ferroelectric (FE) phase with the *Cm*2*m* space group. The line with $E = 244.75 \times 10^5$ V/m, passing through the point of the phase transition, separates the plane of Fig. 3 into two parts. The left part is consistent with an AFE phase; the right one, with an FE phase. It is easy to make sure that the corresponding functional dependences $\omega(E)$ for these two parts are different, but both functions have a minimum near $E = 244.75 \times 10^5$ V/m. Such a behavior of the frequency of the spectral line near the phase transition due

* *Department of Physics, University of Puerto Rico at Mayaguez, 00680 USA*

** *Institute of Physics, Rostov State University, Rostov-on-Don, 344104 Russia*

*** *Department of Chemistry, University of Puerto Rico at Mayaguez, 00680 USA*

**** *Institute of Cell Biophysics, Russian Academy of Sciences, Pushchino, Moscow oblast, 142292 Russia*

1028-3358/01/4606-0389$21.00

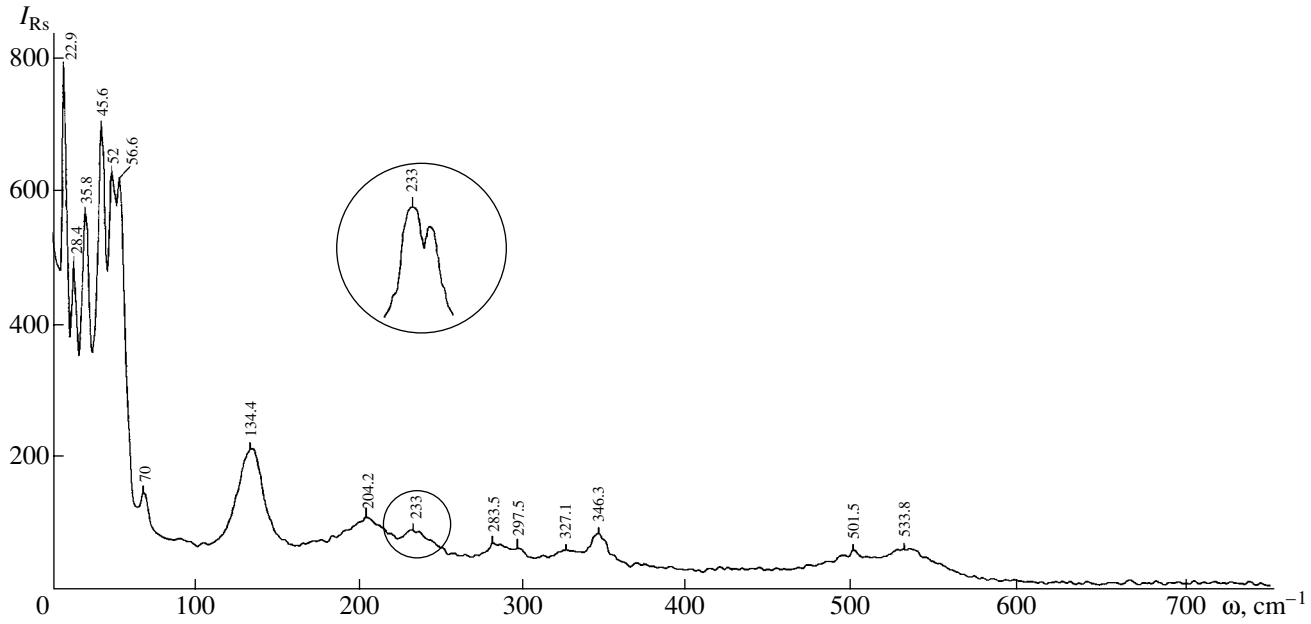

Fig. 1. The Raman spectrum of $PbZrO_3$; T = 293 K (I_{Rs} is the relative intensity of Raman scattering light, ω is the frequency).

to the temperature or hydrostatic pressure effect is characterized in the literature as a quasisoft behavior [9].

According to the commonly accepted interpretation [10], normal vibrations with frequencies in the range 210–240 cm^{-1} in perovskite-type crystals with the general formula ABO_3, in which Zr occupies the B position, are deformation-type and are associated with the change in the angle of the O–Zr–O bond. Recent results of theoretical studies give indirect evidence that the vibration of interest corresponds to a soft ferroelectric mode [11]. According to [11], the Born effective charge calculated for different transverse optical modes in $PbZrO_3$ is maximum for a soft ferroelectric mode involving Zr atoms. This implies that the frequency of this mode should have the strongest dependence on the external electric field as compared to other vibrations.

The above arguments, as well as the fact that only the frequency of the line at 233 cm^{-1} depends notably on the electric field, justify our suggestion that this vibration can be associated with the induced phase transition *Pbam* ⟶ *Cm*2*m* we are studying here. This suggestion is also supported by the frequency behavior near the phase-transition point, which is typical of the soft mode (and some other modes): it follows from Fig. 3 that the vibration frequency as a function of the field changes at a rate three times higher in the FE phase than in the AFE phase near the phase transition. Similar relationships are also fulfilled for spontaneous phase transitions; they are commonly known as the rules of "two" and "four" [12].

To discuss the dependence of the frequency ω on E for the AFE phase (Fig. 3) from the standpoint of lattice dynamics, we use the basic formula for the frequency

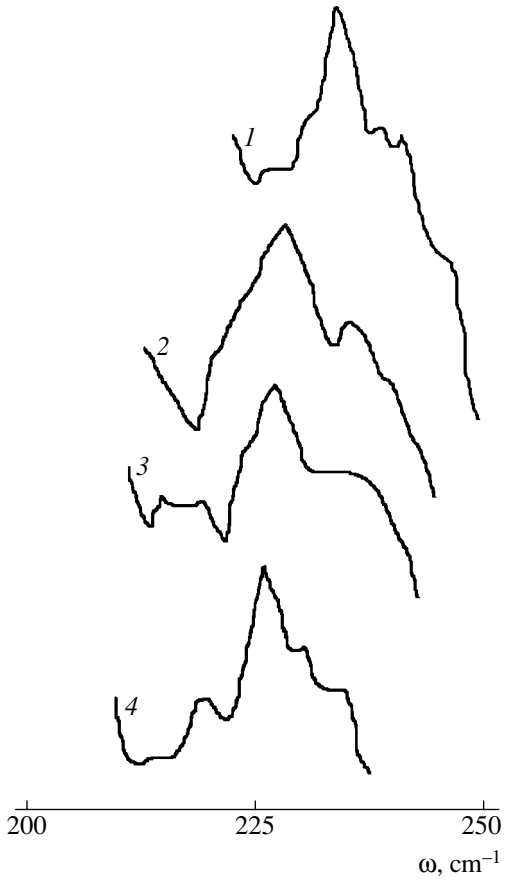

Fig. 2. Fragments of the Raman spectrum of $PbZrO_3$ at various strengths of the electric field near the line that has a frequency of 233 cm^{-3} in the absence of an electric field; E = 116 × 10^5 (*1*), 204 × 10^5 (*2*), 226 × 10^5 (*3*), 239 × 10^5 V/m (*4*); T = 293 K.

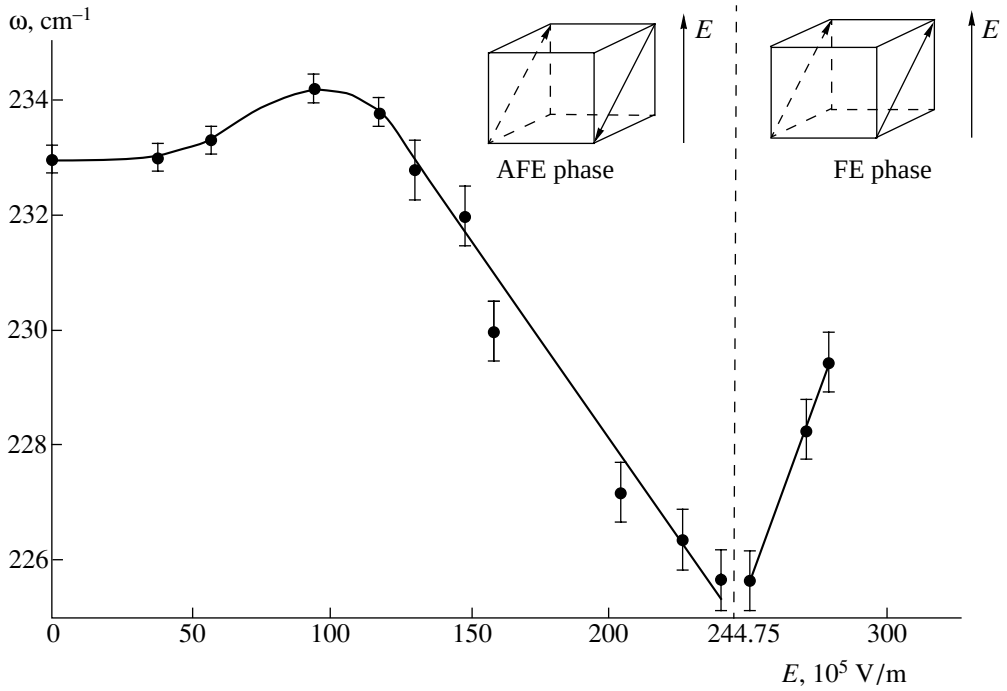

Fig. 3. Quasisoft behavior of the frequency ω of the line at 233 cm^{-1} in the Raman spectra of $PbZrO_3$ for the phase transition AFE ⟶ FE (*Pbam* ⟶ *Cm2m*) induced by an electric field; $T = 293$ K.

of the transverse optical mode ω_T deduced by Cochran [1]; though sufficiently rough, this formula is a useful illustration for the case under consideration:

$$\mu\omega_T^2 = R - \frac{4\pi(n^2+2)(Ze)^2}{9v}. \quad (1)$$

Here, R is the effective force constant, Z is the effective charge, v is the unit cell volume, μ is the reduced ionic mass, e is the electron charge, and n is the refraction index. We have established in this report, as well as in previous works [13], that the unit cell parameters and birefringence of $PbZrO_3$ are independent of the electric field strength up to the field strength that induces the phase transition. This gives grounds to consider only R and Z functions of the electric field in (1) and interpret the observed frequency change as a result of the electric-field dependence of the force constants. This conclusion agrees with the fact that the appearance of the ferroelectric state in crystals with perovskite-type structure is not related to the dependence of the electrostatic polarizability on the crystal volume [12]. Equating expression (1) to a polynomial,

$$[\omega(E)]^2 = a + bE^2 + cE^4 + dE^6 + fE^8,$$

which approximates to within acceptable accuracy the square of the experimental plot presented in Fig. 3, and taking into account the fact that both terms in the right-hand side of Eq. (1) are positive, we find R and Z as a function of the field E:

$$\frac{R}{\mu} = bE^2 + dE^6 + a_1,$$

$$\frac{Z^2}{\mu} = -\frac{9v(cE^4 + fE^8)}{4\pi(n^2+2)e^2} + a_2,$$

with the coefficients $a = 53881.5$ cm^{-2}, $b = 0.26986617$ cm^{-4}/kV^2, $c = -2.1948731 \times 10^{-5}$ cm^{-6}/kV^4, $d = 4.8372522 \times 10^{-10}$ cm^{-8}/kV^6, $f = -3.4644176 \times 10^{-15}$ cm^{-10}/kV^8, and $a_1 + a_2 = a$.

Extrapolating graphically the polynomial dependence $\omega(E)$ to $\omega = 0$, we obtain the field strength $E = 315.6 \times 10^5$ V/m at which the balance of short-range and Coulomb forces results in the loss of crystal stability with respect to small deformations.

One can explain physically that, in contrast to a spontaneous phase transition, the lowering of the soft-mode frequency for the field-induced phase transition is less significant: the dielectric polarizability, which jumpwise increases in the induced phase, is thermodynamically conjugated to the electric field, which favors a forced freezing of atomic displacements with the wave vector $\mathbf{k} = 0$ even for a relatively high frequency of the soft mode.

To summarize, we can say that, in accordance with the soft mode theory, the reduction of the mechanical stability of a crystal is observed near the phase transition induced by an electric field. The total loss of stabil-

ity is postulated as the main reason for the spontaneous phase transition. However, in the case studied, the drop of the thermodynamic stability of the AFE phase with respect to the FE phase occurs at lower fields than the field at which the crystal becomes mechanically unstable.

ACKNOWLEDGMENTS

The authors are grateful to V.S. Gorelik, V.V. Koltashev, and V.G. Plotnichenko for their assistance in developing the Raman-spectroscopy technique in the absence of an electric field and N.G. Leont'ev for his help in performing the X-ray diffraction studies.

One of the authors (A. Leyderman) is grateful to AFOSR (grant F49620-99-1-0308) for their financial support.

REFERENCES

1. W. Cochran, Adv. Phys. **9** (33/36), 387 (1960).
2. L. D. Landau and E. M. Lifshitz, *Statistical Physics* (Nauka, Moscow, 1976; Pergamon, Oxford, 1980), Part 1.
3. O. E. Fesenko, Dokl. Akad. Nauk SSSR **229**, 1109 (1976) [Sov. Phys. Dokl. **21**, 431 (1976)].
4. O. E. Fesenko, R. V. Kolesova, and Yu. G. Sindeev, Fiz. Tverd. Tela (Leningrad) **21**, 1152 (1979) [Sov. Phys. Solid State **21**, 668 (1979)].
5. V. A. Shuvaeva, M. Yu. Antipin, O. E. Fesenko, and Yu. T. Struchkov, J. Phys.: Condens. Matter **8**, 1615 (1996).
6. A. V. Leyderman, V. G. Zaletov, O. E. Fesenko, *et al.*, Fiz. Tverd. Tela (St. Petersburg) **41**, 1279 (1999) [Phys. Solid State **41**, 1169 (1999)].
7. O. E. Fesenko and V. S. Popov, Dokl. Akad. Nauk SSSR **260**, 1134 (1981) [Sov. Phys. Dokl. **26**, 926 (1981)].
8. G. Kugel, I. Junkowska-Sumara, K. Roleder, and J. Dec, J. Korean Phys. Soc. **32**, S581 (1998).
9. A. P. Fedotov, V. F. Shabanov, and A. D. Shefer, Fiz. Tverd. Tela (Leningrad) **21** (11), 3483 (1979) [Sov. Phys. Solid State **21**, 2013 (1979)].
10. C. H. Perry and D. J. McCarthy, Phys. Rev. **138** (5A), A1537 (1965).
11. W. Zhong, R. D. King-Smith, and D. Vanderbilt, Phys. Rev. Lett. **72**, 3618 (1994).
12. R. Blinc and B. Zeks, *Soft Modes in Ferroelectrics and Antiferroelectrics* (North-Holland, Amsterdam, 1974; Mir, Moscow, 1975).
13. O. E. Fesenko and V. G. Smotrakov, Ferroelectrics **12**, 211 (1976).

Translated by T. Galkina

Doklady Physics, Vol. 46, No. 6, 2001, pp. 393–395. Translated from Doklady Akademii Nauk, Vol. 378, No. 5, 2001, pp. 610–612.

PHYSICS

Fractal Nature of Sea Surface Reverberation

L. M. Lyamshev

Presented by Academician F.V. Bunkin December 6, 2000

Received December 25, 2000

An empirical frequency-angular dependence characterizing the high-frequency backscattering by a ruffled sea surface is well known. This dependence was obtained in [1] by Schulkin and Shaffer by means of analysis and generalization of many experimental results:

$$N_s = 10\log(fh\sin\theta)^{0.99} - 45. \quad (1)$$

Here, N_s is the amplitude (expressed in decibels) of the sound scattering by the sea surface, f is the sound frequency, h is the amplitude of the rough sea, and θ is the sliding angle.

To date, there exists no explanation for the physical mechanisms governing the origin or nature of this dependence. Meanwhile, we can see that dependence (1) is described by a power law with a fractional (noninteger) exponent, which is typical of the scattering of waves by fractal structures and surfaces. It is well known that power dependence of the wave scattering on the frequency (wavelength) and scattering angle with a fractional exponent [2] is characteristic of these fractals. It is natural to relate dependence (1) to the fractal features of a sea surface.

There exist rather convincing data in favor of the fact that the sea surface exhibits fractal features. For example, Barenblatt and Leĭkin [3] indicated the self-similarity of the high-frequency spectrum for wind waves on the sea surface and proposed a formula describing the frequency spectrum of the rough sea. This spectrum features a power law with an exponent that can acquire fractional values. The authors of [3] paid attention to many experimental observations, indicating the fact that the frequency spectrum of sea-surface waves is described by the power (fractal) law.

In [4], expressions are derived that characterize, in three-dimensional space, the elevations and the frequency spectrum for a billowy sea surface. These expressions are obtained on the basis of the modified Weierstrass–Mandelbrojt function, which is often used for describing fractal surfaces. It was noted in [4] that the sea surface under a strong swell is fractal with surface-wave amplitudes of 0.1 to 100 m, the fractal dimension being $D \approx 2.25$.

Andreev Acoustical Institute, Russian Academy of Sciences, ul. Shvernika 4, Moscow, 117036 Russia

In a recent publication [5], an attempt was made to theoretically relate dependence (1) to the fractal features of the sea surface. Sound scattering in two-dimensional space is considered under the condition that the surface is described by the Koch generalized fractal curve. This curve is characterized by the parameters

$$n = 0, \quad a^{(0)} = \Lambda,$$
$$n = 1, \ a_1^{(1)} = \frac{\Lambda_0}{4}(1-\alpha)^{1/2}, \ a_2^{(1)} = 2a_1^{(1)}, \ a_3^{(1)} = 2a_1^{(1)}, \quad (2)$$
$$n = 2, \quad a_1^{(2)} = \ldots$$

Here,

$$\alpha = \frac{4A_0}{\Lambda_0}\cot\frac{\Theta}{2}; \quad (3)$$

n is the number of the sequence (step) for the formation of the fractal curve; Λ_0 is a seed; $a_1^{(1)}$, $a_2^{(1)}$, and $a_3^{(1)}$ are elements composing a generatrix element of the Koch curve; A_0 is the amplitude; and Θ is the angle between neighboring elements of the fractal set (Koch curve). The Hausdorff measure for the indicated generalized fractal curve is expressed by the formula

$$(2^{1-D}+1)(a_2^{(1)})^D = 1, \quad (4)$$

where D is the fractal dimension, $1 < D < 2$.

The calculation of the sound scattering is performed in the Kirchoff approximation, when the condition $\lambda \ll \Lambda_0, A_0$ is valid, where λ is the wavelength of the sound wave. In essence, the calculation of sound scattering by a surface is approximated by the Koch prefractal. In this case, in order to exclude prefractal peculiarities from the consideration, the calculation of the scattered field was based on the procedure proposed in [6]. The expression for the intensity of the sound backscattering by a rough surface (i.e., by the Koch prefractal), which was obtained in [5], has the form

$$N_s = N_s^0 + 10\log\left[fh\tan\frac{\Theta}{2}\sin\theta\right]^{2D}. \quad (5)$$

Expression (5) virtually coincides with formula (1) under the assumption that the conditions $\Theta \approx \frac{\pi}{2}$ and $D \approx 0.5$ are fulfilled. It is worth remembering that the

1028-3358/01/4606-0393$21.00

dimension of the Koch prefractal is characterized by the condition $1 < D < 2$.

In the opinion of the author of [5], the necessity of satisfying the equality $D \cong 0.5$ in formula (5) may be explained by the fact that the degeneration of the Koch continuous fractal curve into the Cantor set occurs. It is well known that the Cantor-set dimension is $0 < D < 1$ [2].

In our opinion, this explanation, being not sufficiently evident, may turn out to be quite reasonable in the light of optical experiments [7]. The authors of this experiment studied the fractal properties of collapsing-wave zones on the sea surface. The experimental data were collected as a result of remote optical probing of the sea surface. A series of large-scale photographs of a ruffling sea surface with the presence of foam formations that accompany collapsing surface gravity waves was obtained. In other words, this experimental material contained data related to the backscattering of light (i.e., electromagnetic waves) by the sea surface in the case of collapsing waves. It was established that the distribution of the collapsing zones is fractal with the dimension $D = 0.5$, which characterizes the Cantor set.

Comparing formulas (1) and (5) with the experimental results of [7], we can conclude that the acoustical experiments, whose results are generalized in [1], correspond to the conditions when the sound backscattering arises on separate wave troughs of the sea-surface ruffle. However, in this state of the sea, even in the presence of collapsing sea waves, as observed in optical experiments [7], the efficient production of the near-surface layer of air bubbles did not yet occur. In the opposite case, when this layer does occur at the sea surface, the dependence described by formula (1) is violated. However, therewith, as was shown in [8], the sound backscattering by the sea surface also obeys the power law. In this case, the sound scattering is caused not by the direct effect of the sea surface but by a layer of air bubbles. It turned out that the spectrum of the sound-velocity fluctuations in the layer of near-surface bubbles satisfies the Kolmogorov–Obukhov law, which, as is now well known, reflects the fractal structure of the turbulence. The calculations of the backscattering intensity performed in [8] are in agreement with experimental data for both rather low frequencies (from 0.1 kHz) and a wide range of sliding angles of incidence. Schulkin and Shaffer emphasize in [1] that power laws for intensity variations of the sound backscattering by the sea surface were obtained by a number of researchers. As above [cf. (1)], their experimental results can be written out in the form

$$N_s = 10\log(fh\sin\theta/K_i)^{\nu_i}. \quad (6)$$

Hence, it follows from [9], [10], [11] and [12] that $K_1 = 3.28 \times 10^2$, $\nu_1 = 2.03$; $K_2 = 5.57 \times 10^3$, $\nu_2 = 1.52$; $K_3 = 1.81 \times 10^3$, $\nu_3 = 1.43$; and $K_4 = 6.88 \times 10$, $\nu_4 = 1.03$, respectively. At the same time, for dependence (1) in [1], we have $K = 3.649 \times 10^4$ and $\nu = 0.99$.

Dependences (6) could be considered individual, in a certain sense, occasional facts. The authors of [1], apparently, analyzed these dependences from these positions and, as a result of generalization, obtained the averaged dependence described by expression (1). In the actual situation, the results of [9–12] taken separately seem to be quite reasonable. They reflect the experimental conditions or, in other words, the state of the sea surface, i.e., its fractal properties. In this case, the exponent in the power law indicates the fractal dimension. This conclusion coincides with the above-mentioned ideas of [2]: the approximation of experimental spectra for wind waves of the sea surface obeys the power (fractal) law

$$N_s = A\omega^{-\gamma}, \quad (7)$$

where ω is the wave frequency and A is constant.

Analysis of a large number of experimental spectra of developed sea waves, which was performed in [13] (see also [1]), has shown that for the frequency range $\omega = 1.5$–3.8 s^{-1}, the values of n lie in the interval $\gamma = 2.5$–4.3.

The fact that the fractal properties of a billowy sea surface can be characterized by different fractal dimensions depending on external conditions and the state of the sea surface is confirmed, in particular, by the results of optical experiments [14] and their comparison with the experimental data of [7]. In [14], the results of experimental studies are presented for static characteristics of wind waves on the ocean surface. The investigations were carried out by scanning the sea surface by a laser beam. It was found that the set of mirror points on a ruffling ocean surface corresponds to a Cantor set with fractal dimension $0 < D = 0.8 < 1$. It should be remembered that optical experiments [7] yield the fractal dimension $D = 0.5$. The experimental results of [7] and [14] do not contradict each other. Moreover, they indicate the existence of a variety of fractal properties for a billowy sea surface.

As should be expected, at small amplitudes of the surface ruffling or sufficiently long sound waves, Rayleigh scattering is observed. In this case, the exponent in the power law of the sound-intensity variation as a function of the frequency is $\gamma = 4$. The sea surface is similar to an Euclidean surface. However, even when it is fractal rather than Euclidean, its fractal properties did not manifest themselves in scattering of low-frequency sound.

Thus, we may state that the high-frequency sea surface reverberation is characterized by fractal properties or has a fractal nature in a wide variation range of the sea ruffling. The frequency dependence for the reverberation intensity obeys the power law with a fractional exponent. The value of the exponent yields information on the fractal properties of the sea surface and its fractal dimension and, thus, can serve as a characteristic of sea-surface ruffling.

ACKNOWLEDGMENTS

This work was supported by the Russian Foundation for Basic Research, project no. 99-02-16334.

REFERENCES

1. M. Schulkin and M. Shaffer, J. Acoust. Soc. Am. **36**, 1699 (1964).
2. J. Feder, *Fractals* (Plenum, New York, 1988; Mir, Moscow, 1991).
3. G. I. Barenblatt and V. A. Leĭkin, Izv. Akad. Nauk SSSR, Fiz. Atm. Okeana **17**, 50 (1981).
4. B. J. West, J. Opt. Soc. Am. **7**, 1074 (1990).
5. Z. W. Qian, J. Acoust. Soc. Am. **107**, 260 (2000).
6. A. Freedman, Acustica **12** (1), 10 (1962).
7. G. M. Zaslavskiĭ and E. A. Sharkov, Dokl. Akad. Nauk SSSR **294**, 1362 (1987) [Sov. Phys. Dokl. **32**, 499 (1987)].
8. K. E. Gilbert, J. Acoust. Soc. Am. **94**, 3325 (1993).
9. *Principles of Underwater Sound*, Summary Technical Report (National Defence Research Council Division 6, Washington, DC, 1946), Vol. 7, Chap. 5, pp. 99–109.
10. R. J. Urick and R. M. Hoover, J. Acoust. Soc. Am. **28**, 1038 (1956).
11. G. R. Garisson, S. R. Murphy, and D. S. Potter, J. Acoust. Soc. Am. **32**, 104 (1960).
12. R. P. Chapman and R. P. Harris, J. Acoust. Soc. Am. **38**, 1592 (1962).
13. P. L. Grose, K. L. Warsh, and M. Garstang, J. Geophys. Res. **77**, 3902 (1972).
14. V. V. Zosimov and K. A. Naugolnykh, Chaos **4**, 21 (1994).

Translated by G. Merzon

Doklady Physics, Vol. 46, No. 6, 2001, pp. 396–399. Translated from Doklady Akademii Nauk, Vol. 378, No. 5, 2001, pp. 613–616.

PHYSICS

Critical Phenomena in Plasmas and Electrolyte Melts

G. A. Martynov

Presented by Academician V.E. Fortov December 4, 2000

Received December 4, 2000

The problem associated with describing critical phenomena in charged-particle systems is of both applied and theoretical importance. From the applied standpoint, the problem is interesting because both plasma and electrolyte solutions and melts are related to this class of systems. From the theoretical standpoint, the problem attracts attention through the fact that, in the case of charged particles, the available Kadanov–Wilson theory of critical phenomena, which is based on methods of the similarity theory and renormalization-group theory [1], has faced a challenging phenomenon that could not be explained [2]. In addition, methods of numerical simulations also proved unsuccessful [3]. As a result, until now, it has been unclear how important the critical indices in the charged-particle systems are. However, it is this topical issue that is of principal importance. The matter is that in the Kadanov–Wilson theory, all substances are divided into universality classes and it is postulated that the critical indices are the same within each class. At the same time, there exist no criteria that make it possible to relate a particular substance to a given class. Moreover, at present, it is entirely unknown whether different classes exist if all substances are related to the same class. Thus far, this question has been considered only empirically. There exist certain experimental data that imply the fact that the critical indices in liquids may slightly differ from those predicted by the Kadanov–Wilson theory for crystals. Nevertheless, the discrepancies observed in experiments are too small and insufficiently reliable to make final conclusions (see [4]).

In [5, 6], an alternative (with respect to the Kadanov–Wilson theory) approach to the critical phenomena was developed. It is based on a local Ornstein–Zernike equation that characterizes the state of a substance at a given point of a system rather than on a global Gibbs distribution describing the state of the macroscopic system as a whole. However, since the equations underlying these grounds are based on the same postulates, both approaches are essentially equivalent [7]. Therefore, the Ornstein–Zernike equation virtually represents the same Gibbs distribution written out in the integral form [8].

As is shown in [5, 6], in the certain vicinity of a critical point, the Ornstein–Zernike equation has two solutions, namely, regular and critical. When approaching the critical point, the regular solution gradually degenerates, completely vanishing at this point. In contrast, the critical solution degenerates when going away from the critical point. However, in the nearest neighborhood of the critical point, the critical solution generates nonanalytic values of critical indices that satisfy the same similarity relationships as in the Kadanov–Wilson theory (note that the particular values of indices were not calculated in [5, 6]).

In this study, the method developed in [5, 6] is extended to the case of critical phenomena in charged-particle systems. In particular, we show that, in these systems, only the regular (analytical) solution exists. However, it generates critical indices that differ from those predicted by the Van der Waals theory (and, of course, from the nonanalytic indices in the Kadanov–Wilson theory). In addition, we also show that the critical amplitudes in these systems tend to infinity when approaching the critical point (in the case of neutral particles, they are always finite).

FORMULATION OF THE PROBLEM

In what follows, we restrict ourselves, for simplicity, to consideration of the so-called primitive electrolyte model defined by the following relationships:

$$e = e_+ = -e_-, \quad \rho = n_\pm\sigma^3 = \rho_{\alpha\beta}, \quad \sigma = \sigma_{\alpha\beta}, \quad \Phi(r) = \Phi_{\alpha\beta}(r), \tag{1}$$

where $e_\pm$ are the charges of cations and anions; ρ_α are their concentrations; $\sigma_{\alpha\beta}$ are the particle diameters for different species α and $\beta = +$ and $-$, respectively; $\Phi_{\alpha\beta}(r)$ are the short-range interaction potentials; and r is the distance between particles. In this case, the system of Ornstein–Zernike equations takes the form [9]

$$h_{++}(t) = -\varphi(t) + C_{++}(t)$$

Institute of Physical Chemistry,
Russian Academy of Sciences,
Leninskiĭ pr. 31, Moscow, 117915 Russia

1028-3358/01/4606-0396$21.00

$$+\rho\int_V C_{++}(t')h_{++}(|\mathbf{t}-\mathbf{t}'|)d\mathbf{t}' + \rho\int_V C_{+-}(t')h_{+-}(|\mathbf{t}-\mathbf{t}'|)d\mathbf{t}',$$
$$h_{+-}(t) = \varphi(t) + C_{+-}(t) \tag{2}$$
$$+\rho\int_V C_{++}(t')h_{+-}(|\mathbf{t}-\mathbf{t}'|)d\mathbf{t}' + \rho\int_V C_{+-}(t')h_{++}(|\mathbf{t}-\mathbf{t}'|)d\mathbf{t}',$$

where $t = \frac{r}{\sigma}$, $h_{\alpha\beta} = \exp\left[-\left(\frac{\Phi_{\alpha\beta}}{\theta} + \omega_{\alpha\beta}\right)\right] - 1$ is the common correlation function, $\theta = k_B T$ is the temperature (expressed in ergs), $\omega_{\alpha\beta}(t)$ are the thermal potentials, $C_{\alpha\beta} = h_{\alpha\beta} - \omega_{\alpha\beta} + B_{\alpha\beta}$ are the direct correlation functions, and $B_{\alpha\beta}(t)$ are the bridge functionals. In addition, Eq. (2) involves the electrostatic potential $\varphi(t)$, its value being determined by the Poisson equation

$$\Delta\varphi(t) = -\kappa_D^2[h_{++}(t) - h_{+-}(t)] \tag{3}$$

and by the electrical-neutrality condition of the Debye atmosphere

$$1 = -4\pi\rho\int_0^{+\infty}[h_{++}(t) - h_{+-}(t)]t^2 dt \tag{4}$$

$\left(\text{here, } \kappa_D^2 = 8\pi\chi\rho = \frac{1}{R_D^2}\text{, where } R_D \text{ is the Debye radius and } \chi = \frac{e^2}{\theta\sigma}\right)$.

The system of equations obtained corresponds to the exact formulation of the problem. However, this system is unclosed until closing equations that link $B_{\alpha\beta}$ and $\omega_{\alpha\beta}$ are given. Below, we do not need the closing equations, since they are required only for calculating particular values of amplitudes and other numerical coefficients.

THE GENERAL SOLUTION

We expand all functions involved in Eqs. (1)–(4) into the Fourier integral

$$\psi(k) = \int_V \psi(t)e^{-i\mathbf{kt}}d\mathbf{t} = 4\pi\int_0^\infty \psi(t)\frac{\sin(kt)}{kt}t^2 dt,$$
$$\psi(t) = \frac{1}{8\pi^3}\int_V \psi(k)e^{-i\mathbf{kt}}d\mathbf{k} = \frac{1}{2\pi^2}\int_0^\infty \psi(k)\frac{\sin(kt)}{kt}k^2 dk. \tag{5}$$

Thereafter, Eqs. (3) and (4) are reduced to the system of algebraic equations

$$\varphi(k) = \frac{\kappa_D^2}{k^2}[h_{++}(k) - h_{+-}(k)], \tag{6}$$

$$h_{++}(k) = -\frac{\kappa_D^2}{k^2}[h_{++}(k) - h_{+-}(k)] + C_{++}(k)$$
$$+\rho\{C_{++}(k)h_{++}(k) + C_{+-}(k)h_{+-}(k)\},$$
$$h_{+-}(k) = \frac{\kappa_D^2}{k^2}[h_{++}(k) - h_{+-}(k)] + C_{+-}(k) \tag{7}$$
$$+\rho\{C_{++}(k)h_{+-}(k) + C_{+-}(k)h_{++}(k)\}.$$

Solving this system with respect to the unknowns $h_{\alpha\beta}$, we arrive at

$$h_{\alpha\beta}(k) = \frac{\Delta(k) + \chi_{\alpha\beta}(k)}{1 - \Delta(k)}, \tag{8}$$

where

$$\chi_{++} = -\rho C_{++}(k) + \frac{\kappa_D^2}{k^2}\{2 - \rho[C_{++}(k) + C_{+-}(k)]\}, \tag{9}$$

$$\chi_{+-} = -\rho C_{++}(k) - \rho[C_{++}(k) - C_{+-}(k)]$$
$$\times\{1 - \rho[C_{++}(k) + C_{+-}(k)]\}$$
$$+\frac{\kappa_D^2}{k^2}\{2 - \rho[C_{++}(k) + C_{+-}(k)]\},$$

$$\Delta = 2\rho C_{++}(k) - \rho^2[C_{++}^2(k) - C_{+-}^2(k)]$$
$$-2\frac{\kappa_D^2}{k^2}\{1 - \rho[C_{++}(k) + C_{+-}(k)]\}. \tag{10}$$

Substituting solution (8) into (5), we obtain [5]

$$th_{\alpha\beta}(t) = \frac{1}{2}\frac{4\pi}{(2\pi)^3}\int_{-\infty}^{+\infty}\frac{\Delta(k) + \chi_{\alpha\beta}(k)}{1 - \Delta(k)}\frac{\sin(kt)}{kt}k^2 dk$$
$$= \frac{1}{4\pi^2 i}\int_{-\infty}^{+\infty}\frac{\Delta(k) + \chi_{\alpha\beta}(k)}{1 - \Delta(k)}e^{ikt}k dk. \tag{11}$$

This integral can be calculated with the help of the theory of residues. Closing the real axis in the upper half-space by an arc of infinite radius, we find

$$h_{\alpha\beta}(t) = \sum_j A_{\alpha\beta}^j\frac{e^{-z_j t}}{t}, \tag{12}$$

where

$$A_{\alpha\beta}^j = \frac{z_j^2[1 + \chi_{\alpha\beta}(z_j)]}{2\pi\rho\tilde{\Delta}(z_j)},$$

$$\tilde{\Delta}(z_j) = 2\left\{\rho\tilde{C}_{++}\left[1-\rho C_{++}-\frac{\kappa_D^2}{z_j^2}\right]\right.$$

$$\left.+\rho\tilde{C}_{+-}\left[\rho\tilde{C}_{+-}-\frac{\kappa_D^2}{z_j^2}\right]-2\frac{\kappa_D^2}{z_j^2}[1-\rho(C_{++}+C_{+-})]\right\}, \quad (13)$$

$$C_{\alpha\beta}(z_j) = 4\pi\int_0^\infty C_{\alpha\beta}(t)\frac{\sinh(z_j t)}{z_j t}t^2(dt),$$

$$\tilde{C}_{\alpha\beta}(z_j) = 4\pi\int_0^\infty C_{\alpha\beta}(t)\left[\cosh(z_j t)-\frac{\sinh(z_j t)}{z_j t}\right]t^2 dt,$$

and $\mathbf{k} = i\mathbf{z}$ and z_j are the roots of the transcendental equation

$$1-\Delta(z_j) = 0. \quad (14)$$

Using these formulas, it is possible to find the electrostatic potential,

$$\varphi(t) = \kappa_D^2\sum_j \varphi_j\frac{\exp[-z_j t]}{t}, \quad (15)$$

where

$$\varphi_j = \frac{C_{++}(z_j)-C_{+-}(z_j)}{2\pi\tilde{\Delta}}\{1-\rho[C_{++}(z_j)+C_{+-}(z_j)]\},$$

as well as the condition for the electrical neutrality of the Debye atmosphere,

$$1 = 2\sum_j \frac{[C_{++}(z_j)-C_{+-}(z_j)]\{1-[C_{++}(z_j)+C_{+-}(z_j)]\}}{\tilde{\Delta}(z_j)}. \quad (16)$$

CRITICAL PHENOMENA

As is well known, a critical point is defined by the conditions

$$\left(\frac{\partial P}{\partial\rho}\right)_\theta = 0, \quad \left(\frac{\partial^2 P}{\partial\rho^2}\right)_\theta = 0, \quad (17)$$

where P is pressure. Therefore, the isothermal compressibility, by definition, equal to [8],

$$\kappa_\theta = \left(\frac{\partial P}{\partial\rho}\right)_\theta^{-1}$$

$$= \frac{1}{\theta}\left\{1+4\pi\rho\int_0^\infty[h_{++}(t)+2h_{+-}(t)+h_{--}(t)]\right\}t^2 dt$$

$$= \frac{1}{\theta}\left\{1+8\pi\rho\int_0^\infty[h_{++}(t)+h_{+-}(0)]t^2 dt\right\},$$

becomes infinite at the critical point. Substituting (12) into this expression, assuming $z_j = \lambda_j + i\mu_j$, and integrating over t, we have

$$\kappa_\theta = \frac{1}{\theta}\left\{1+8\pi\left[\frac{A}{\lambda_0^2}+\sum_{j\geq 1}\left(B_j\frac{2\lambda_j\mu_j}{[\lambda_j^2+\mu_j^2]^2}+C_j\frac{\lambda_j^2-\mu_j^2}{[\lambda_j^2+\mu_j^2]^2}\right)\right]\right\}, \quad (18)$$

where $A = A_{++}^{(0)} + A_{+-}^{(0)}$ and all values of λ_j and μ_j lie in the interval $0 \leq \lambda_j, \mu_j \leq \infty$. It follows from equality (18) that κ_θ may become infinite only if the real root of the transcendental equation (14) λ_0 vanishes and the correlation radius $R = \dfrac{1}{\lambda_0} = \infty$. In cases of arbitrary values of λ_j and μ_j ($j \geq 1$), κ_θ has a finite value. Moreover, since, by definition [9],

$$\kappa_\theta^{-1} = \left(\frac{\partial P}{\partial\rho}\right)_\theta = \theta\left\{1-4\pi\sum_{\alpha,\beta}\rho_\alpha\int_0^\infty C_{\alpha\beta}(t)t^2 dt\right\} \quad (19)$$

$$= \theta\{1-4\pi\rho[C_{++}^{(2)}+C_{+-}^{(2)}]\},$$

where $C_{\alpha\beta}^{(l)} = \dfrac{4\pi}{(2l-1)!}\displaystyle\int_0^\infty C_{\alpha\beta}(t)t^{2l}dt$ are the moments of the function $C_{\alpha\beta}$ on the order of $2l$, we have, at the critical point, the equality

$$1-\rho[C_{++}^{(2)}+C_{+-}^{(2)}] = 0. \quad (20)$$

Expanding in (13) the amplitude $A_{\alpha\beta}^0$ into a series in terms of λ_0, we obtain as $\lambda_0 \longrightarrow 0$ that

$$A_{++}^0 \approx A_{+-}^0 \longrightarrow \frac{1}{\lambda_0^2}\frac{\kappa_D^2}{8\pi\rho^2\Gamma} \longrightarrow \infty, \quad (21)$$

where

$$\Gamma = -C_{++}^{(4)}+\rho[C_{++}^{(2)}C_{++}^{(4)}-C_{+-}^{(2)}C_{+-}^{(4)}]+8\pi\chi[C_{++}^{(6)}+C_{+-}^{(6)}].$$

Next, substituting this expression into relationship (18) and taking into account that $A = A_{++}^0 + A_{+-}^0$, we find that, when approaching the critical point, the isothermal compressibility increases by the law

$$\kappa_\theta \longrightarrow \frac{1}{\lambda_0^4}\frac{2\kappa_D^2}{\rho^2\theta\Gamma} \sim \frac{1}{\lambda_0^4} \longrightarrow \infty \quad (22)$$

(we recall that, in the case of neutral particles, it varies as $\kappa_D \sim \lambda_0^{-(2-\eta)}$, where the critical index $\eta \approx 0.05$ [9]). Since the regular (analytical) solution at the critical point becomes infinite [see formula (21)], then no solutions can manifest themselves against the background of the regular solution.

Thus, we show that the critical indices in charged-particle systems differ from the predictions of both the classical and Kadanov–Wilson theories.

REFERENCES

1. R. Balescu, *Equilibrium and Nonequilibrium Statistical Mechanics* (Wiley, New York, 1975; Mir, Moscow, 1978), Vol. 1.
2. M. E. Fisher, in *New Approaches to Problems in Liquid State Theory*, Ed. by C. Caccamo, J.-P. Hansen, and G. Stell (Kluwer, Dordrecht, 1999), pp. 3–8.
3. J. M. Caillol, D. Levesque, and J. J. Weis, J. Chem. Phys. **107**, 1565 (1997).
4. V. A. Rabinovich and Yu. E. Sheludyak, *Thermodynamics of Critical Phenomena: New Analysis of the Evaluation of Properties* (Begell House, New York, 1998).
5. G. A. Martynov, Teor. Mat. Fiz., No. 3, 498 (1999).
6. G. A. Martynov, Usp. Fiz. Nauk **169** (6), 595 (1999).
7. G. A. Martynov, Usp. Fiz. Nauk **166**, 1105 (1996) [Phys. Usp. **39**, 1045 (1996)].
8. T. Morita and K. Hiroike, Prog. Theor. Phys. **23**, 1003 (1960); **24**, 317 (1961); **25**, 537 (1961).
9. G. A. Martynov, *Fundamental Theory of Liquids* (Institute of Physics, Bristol, 1992).

Translated by Yu. Vishnyakov

Doklady Physics, Vol. 46, No. 6, 2001, pp. 400–402. Translated from Doklady Akademii Nauk, Vol. 378, No. 5, 2001, pp. 617–619.

PHYSICS

On a Discrepancy of Experiments Supporting Certain Conclusions of General Relativity[1]

V. V. Okorokov

Presented by Academician S.T. Belyaev February 1, 2001

Received February 7, 2001

Over a long period of time, I was involved in activities associated with substantiating experiments employing the effect of coherent excitation of energy levels of fast atoms or relativistic nuclei penetrating a crystal [1–4]. In particular, the feasibility of testing the equivalence principle for the gravitational field and the accelerated reference system (for accelerations $a \sim 10^{20}$–10^{21} cm/s^2) was analyzed. I also studied the consistency of possible results of such experiments and well-known experiments on testing certain conclusions of the general relativity (GR). In the process of this analysis, I came up against an intriguing and paradoxical situation.

Unfortunately, the numerous long-term discussions I was involved in did not result in any intelligible scientific elucidation of the paradoxical situation. Therefore, I considered it necessary to attract the attention of the scientific community to this issue by writing this paper.

As is well known, the GR predictions related to variation of a photon frequency when moving along the direction of the gravitational-potential gradient, as well as those related to the variation of the timepiece rate at points with different gravitational potentials, were confirmed in experiments [5–9].

The gravitational shift of the photon frequency $\frac{\Delta\nu}{\nu} = \frac{gH}{c^2}$ was measured in the well-known experiments of Pound and Rebka [5, 6] and Vessot and Levine [7] (Fig. 1).

Variation of the frequency $\Delta\nu$ of photons emitted by ^{57}Fe nuclei [5, 6] or hydrogen atoms in a hydrogen frequency standard [7], when rising (or dropping) through a height H in the gravitational field, has been experimentally recorded. This effect was detected through comparison with a reference frequency of an "oscillator" located at the photon-detection point. In [5, 6], ^{57}Fe nuclei (identical to nuclei radiating photons with an energy of 14 keV at $H = 0$) were taken as an oscillator of the reference frequency at the elevation H. In the experiment of Vessot and Levine [7], a hydrogen frequency standard identical to that emitting photons at the ground level played the same role.

In both cases, it was implied as self-evident that the energy distances between levels for nuclei [5, 6] and atoms [7] are independent of the gravitational potential.

We recall that the stability of the emitted-photon frequency and the fixation accuracy of the detected-photon frequency are unambiguously determined by the stability of the energy distance between levels in nuclei [5, 6] and atoms [7]. The treatment (and even execution!) of these experiments is impossible without assuming the independence of energy-level positions from the gravitational potential. Indeed, even a small shift of the photon frequency can be detected only by comparing it with an invariant reference frequency determined by the invariant positions of nuclear or atomic energy levels.

Three alternative variants in treating the results of experiments on the gravitational shift of the photon frequency are apparently possible:

(a) when rising in the Earth's gravitational field, the photon frequency varies in exact accordance with the formula $\frac{\Delta\nu}{\nu} = \frac{gH}{c^2}$ predicted by the GR, while the positions of nuclear and atomic energy levels are independent of the gravitational potential;

(b) the photon frequency does not vary, whereas the nuclear and atomic energy levels follow the gravitational-potential variation in accordance with the dependence $\frac{\Delta\nu}{\nu} = \frac{gH}{c^2}$;

(c) both the photon frequency and the nuclear levels vary; in this case, different alternatives are possible

[1] The preliminary version was published in the ITEP preprint No. 27-98.

Institute of Theoretical and Experimental Physics, ul. Bol'shaya Cheremushkinskaya 25, Moscow, 117259 Russia

1028-3358/01/4606-0400$21.00

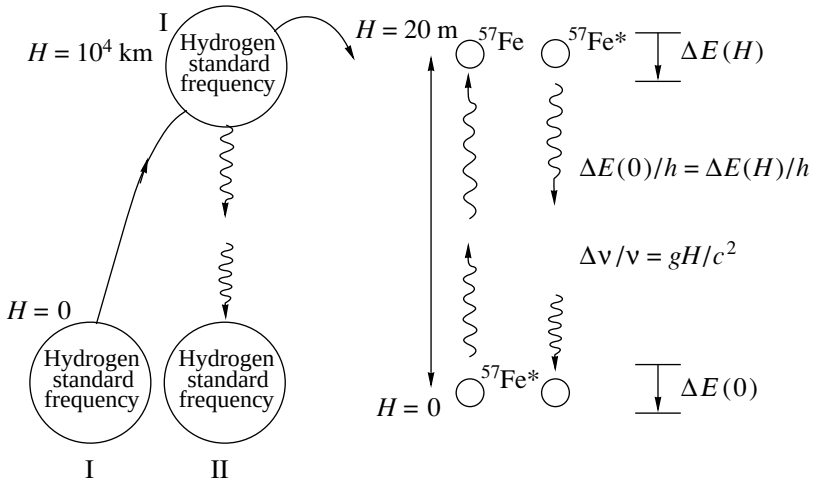

Fig. 1. Gravitational shift of the photon frequency [5–7].

when moving in the gravitational field depending on the sign and the value of these variations.

As is seen from [5–7], version (a) is, undoubtedly and without a trace of hesitation, taken in these papers.

The effect of the gravitational potential on the timepiece rate $\left($this dependence is given quantitatively by the twin formula $\frac{\Delta T}{T} = \frac{gH}{c^2}\right)$ was studied in experiments [8–10]. They were performed by comparing readings of two high-precision frequency standards in a position with the same gravitational potential. Then, one of the frequency standards was lifted, for a while, to a position with different values of the gravitational potential (i.e., to an altitude on the order of a few kilometers).

The divergence between the readings of these instruments after bringing them to the initial point (Fig. 2) quantitatively supports the gravitational-potential dependence of the timepiece rate predicted by the GR.

The treatment of these experiments is unambiguously related to the assumption that the position of atomic energy levels (specifying the rate of the frequency standards) depends on the value of the gravitational potential in which these atoms reside. In this case, the atoms play the role of a "timepiece" measuring the time-rate variation at different altitudes in the Earth's gravitational field. Therefore, the treatment of the well-known experiments of Pound and Rebka [5, 6], as well as those of Vessot and Levine [7], is based, as a matter of course, on assumptions implying the invariance of atomic and nuclear energy levels. These assumptions contradict the well-known GR predictions on the variation of the timepiece rate at points with different gravitational potential. This conclusion is also supported by the experiments performed in [8–10]. It follows from these experiments that there exists, at least, a dependence of atomic energy levels on the gravitational potential. In other words, atoms are timepieces following the variation of the gravitational potential!

Thus, we may conclude that the positive results of the experiments on the gravitational shift of the photon frequency [5–7] and on the gravitational change of the timepiece rate [8–10] are, unfortunately, incompatible.

If the atomic and nuclear energy levels are independent of the gravitational potential, then experiments [5–7] and [8–10] should yield positive and negative results, respectively. If the positions of atomic and nuclear energy levels depend on the gravitational potential, then, in contrast to experiments [8–10], experiments [5–7] cannot yield positive results. It is impossible to simultaneously obtain positive results in both experiments [5–7] and [8–10] since atomic and nuclear energy levels cannot be simultaneously dependent on and independent of the gravitational potential.

This fairly paradoxical and conjectural situation "springing from nowhere" entails a chain of important physical corollaries whose discussion is premature. However, one of them should be recalled. For example,

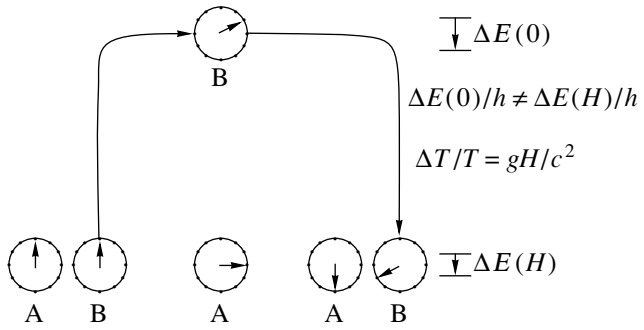

Fig. 2. Variation of the timepiece rate depending on the gravitational potential [8–10].

the motion in an effective gravitational field caused by acceleration (equivalence principle!) is the heart of the twin paradox [11].

Evidently, the indicated inconsistency between the results of experiments, which have already become classical, necessitates additional experimental confirmation in other experiments carried out by different techniques. These experiments could be the coherent excitation of energy levels of fast atoms and relativistic nuclei when penetrating a crystal [1–4]. In these experiments, the projectile nucleus serves as a timepiece whose rate is studied by means of a series of successive interactions with the crystal atoms. A sharp resonant dependence of the effect makes it possible to isolate the component of the energy-level shift in flying nuclei. The appearance of this component is stipulated by the action of the varying effective gravitational potential, which, in turn, is caused by the deceleration of nuclei in the crystal substance.

REFERENCES

1. V. V. Okorokov, Yad. Fiz. **2**, 1009 (1965) [Sov. J. Nucl. Phys. **2**, 716 (1966)].
2. V. V. Okorokov, Pis'ma Zh. Éksp. Teor. Fiz. **2**, 175 (1965) [JETP Lett. **2**, 111 (1965)].
3. C. Moak, S. Datz, O. H. Crawford, *et al.*, Phys. Rev. A **19**, 843 (1979).
4. Yu. L. Pivovarov and A. A. Shirokov, Yad. Fiz. **44**, 882 (1986) [Sov. J. Nucl. Phys. **44**, 569 (1986)].
5. R. V. Pound and G. A. Rebka, Phys. Rev. Lett. **4**, 337 (1960).
6. R. V. Pound and J. L. Snider, Phys. Rev. B **140**, 788 (1965).
7. R. F. C. Vessot and M. N. Levine, Gen. Relativ. Gravit. **10**, 181 (1979).
8. C. O. Alley *et al.*, in *Proceedings of the Conference on Experimental Gravitation, Pavia, 1976*, Ed. by B. Bertotti (Academic, New York, 1977).
9. J. C. Hafele and R. E. Keating, Science **177**, 166 (1972).
10. L. Briatore and S. Leschiutta, Nuovo Cim. B **37**, 219 (1977).
11. A. Einstein, *Collection of Scientific Papers* (Nauka, Moscow, 1965), Vol. 1, p. 616.

Translated by V. Tsarev

Doklady Physics, Vol. 46, No. 6, 2001, pp. 403–406. Translated from Doklady Akademii Nauk, Vol. 378, No. 5, 2001, pp. 620–623.

PHYSICS

Viscosity of Liquids in the Melting Line and in the Supercooled State

Academician V. P. Skripov and M. Z. Faizullin

Received February 5, 2001

1. The coefficient of dynamic viscosity η (below, for brevity, viscosity) enters into the linear relation between the shear velocity $\dot{\varepsilon}$ in a fluid and the tangent component of a force acting between fluid layers in the case of shear. When η is independent of $\dot{\varepsilon} = \frac{du_x}{dy}$, where u is the velocity, the liquid is called Newtonian. The quantity η^{-1} is called fluidity. Depending on the nature of the medium, temperature T, and pressure p, the range of the viscosity variation is great, e.g., from $\eta = 10^{-3}$ Pa s (water under normal conditions) to 10^{12} Pa s in the region of the glass transition. It follows from the given values of η that the approximation of the Newtonian liquid suggests a corresponding space–time scale of performing an experiment or a passage to a more complicated description of a medium as viscous-elastic. The relaxation time τ of shear stresses is determined by the order of magnitude on the basis of the ratio of the viscosity coefficient to an "instantaneous" shear modulus G in Hooke's law:

$$\tau = \frac{\eta}{G}. \tag{1}$$

We have analyzed experimental data on the viscosity of relatively simple molecular liquids and extrapolated these data to the region of a supercooled state. The interest in supercooling ($T < T_m$, where T_m is the melting temperature at a given pressure) is associated with both the problem of homogeneous nucleation [1] and the conditions of preparation of solid-amorphous samples, including metallic glasses. Here, the main difficulty consists in the choice of the viscosity dependence on the liquid thermodynamic parameters and in the intrinsic consistency of data related to T, p, v, and η in the case of using far-range extrapolation.

The goal of this study was to establish the character of the melt-viscosity variation in the line of the crystal–liquid phase equilibrium for both the high pressure and extended states of coexisting phases ($p < 0$) in the case of extrapolating the melting line to the metastable region. For materials being normally melted, the derivative $\frac{dp}{dT_m}$ is positive. An elevation of both temperature and pressure results in the opposite viscosity variation, such that the resulting effect depends on the slope of the melting line. The preliminary consideration [2] has shown that while moving along this line, the liquid becomes more viscous with increasing temperature. This can result in the vitrification of the melt not in the low-temperature region of the continued melting line but in its high-temperature region. In this paper, the problem indicated is considered on the basis of experimental data on the viscosity of a series of liquids and on the basis of extrapolating the values of η over isobars. For the melting line, the Simon equation [3]

$$1 + \frac{p}{p_*} = \left(\frac{T}{T_0}\right)^c \tag{2}$$

was used, in which $c > 1$, p_* are the individual constants and T_0 is the melting temperature at the zero pressure. The applicability of Eq. (2) and its corollaries were discussed in [4] and in other publications.

2. There are two approaches to the description of viscosity that are the most well-known. According to Frenkel, the fluid viscosity is associated with the activation energy E of a local molecular regrouping:

$$\eta = A\exp\left(\frac{E}{kT}\right), \tag{3}$$

where A is a weak (compared to the exponential factor) function of temperature and pressure. The activation energy increases with decreasing temperature and increasing pressure. When approaching the glass-transition region under atmospheric pressure, the parameter E increases by an order of magnitude compared to its values for low-viscous states [1]. Another approach was developed by Bachinskiĭ [5]. The essence of this approach is expressed in the statement that the viscosity

Institute of Thermal Physics, Ural Division, Russian Academy of Sciences, ul. Pervomaĭskaya 91, Yekaterinburg, 620219 Russia.

1028-3358/01/4606-0403$21.00 © 2001 MAIK "Nauka/Interperiodica"

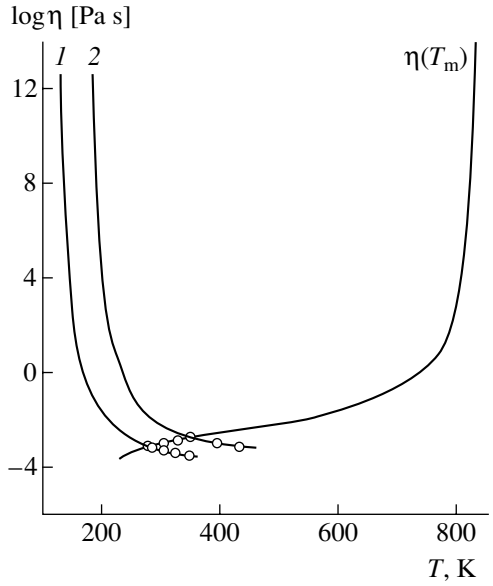

Fig. 1. Variation of the benzene viscosity along the melting line $\eta(T_m)$ and along the isobars (*1*) p = 0.1 and (*2*) 300 MPa. Dots correspond to experimental data. Solid lines are the results of calculations according to formula (5).

of a liquid is determined by its specific volume. Bachinskiĭ proposed the formula

$$\eta = \frac{c}{\nu - \omega}, \tag{4}$$

where c and ω are individual constants. Although subsequent verification has shown the inadequacy of expression (4) in a wide range of viscosities, the heuristic importance of this expression is retained. Frenkel' considered the possibility of formulas (3) and (4) agreeing on the basis of the hole theory of liquids. We have chosen the following expressions for viscosity:

$$\eta = A\exp\left(\frac{B}{T - T_1}\right), \tag{5}$$

$$\eta = a\exp\left(\frac{b}{\nu - \nu_1}\right). \tag{6}$$

They are known as the Fulcher–Tamman and Doolittle formulas, respectively, and can be considered modified versions of formulas (3) and (4). Introducing the quantities T_1 and ν_1 *a priori* determines the zero fluidity by the conditions $T = T_1$ or $\nu = \nu_1$, but the values of T_1 and ν_1 in themselves depend on pressure. In addition, parameters A and b are assumed to be functions of pressure, whereas B and a are considered individual constants. Experimental data for fluid viscosities in the isobars were treated within this approximation using the glass-transition temperature of each material under atmospheric pressure. The consistency of data for T, p, ν, and η was verified for the melting line and glass-transition line by calculations according to formulas (5) and (6). Formula (5) was taken as a basis.

Data on the viscosity of the following liquids were analyzed: argon [6], carbon tetrachloride [7], benzene [8], dodecane [9], octadecane [9], and carbon dioxide [10]. The pressure range in the references indicated was 360 MPa for dodecane and 200–300 MPa for other liquids. The viscosity variation with temperature for two isobars (to the left) and in the benzene melting line is shown in Fig. 1 in a semilogarithmic scale. According to our estimate, the glass transition ($\eta = 10^{12}$ Pa s) on the melting line for benzene occurs at a temperature of 833 K and a pressure of 6.5 GPa.

3. The elevation of the fluid viscosity in the melting line with temperature is associated with the reduction of the specific fluid volume ν in the same direction under the coexistence of phases. This is expressed by the local condition [2]

$$Ml = \frac{\beta_T}{\alpha_p}\frac{dp}{dT_m} = \frac{dp}{dT_m}\left(\frac{\partial p}{\partial T}\right)_\nu^{-1} > 1, \tag{7}$$

where $\beta_T = -\frac{1}{\nu}\left(\frac{\partial \nu}{\partial p}\right)_T$ is the isothermal compressibility coefficient and $\alpha = \frac{1}{\nu}\left(\frac{\partial \nu}{\partial T}\right)_p$ is the coefficient of thermal expansion. Inequality (7) is valid for the conventional melting materials for which the melting line slope $\frac{dp}{dT_m}$ is larger than that of the isochore of a liquid at the point of intersection of the isochore with the melting line. There exists another local criterion that provides the inequality $\frac{d\eta}{dT_m} > 0$:

$$\frac{dp}{dT_m}\left(\frac{\partial p}{\partial T}\right)_\eta^{-1} > 1. \tag{8}$$

This criterion relates the melting-line slope to the constant-viscosity line expressed in the T and p variables. The melting line, three isoviscous curves, and the isochore that has a common [with the line $\eta(T, p)$ = 3 mPa s] point in the melting line are shown in Fig. 2 for dodecane.

Qualitatively, the behavior of the fluid viscosity in the melting line is remarkable not only by increasing η with temperature but by retaining low values of η in the case of metastable continuation of the melting line to the region of low temperatures, i.e., at $\frac{T}{T_0} < 1$. This follows from the monotonicity of isoviscous curves $\eta(T, p)$ = const and from their nonintersecting with one another (Fig. 2).

Although the viscosity in the melting line increases with temperature, this is not yet sufficient evidence that the glass transition occurs in the melting line. Here, the

mutual disposition of the glass transition line $\eta(T, p) = 10^{12}$ Pa s and the melting line in the T, p plane for various materials, as well as the possibility of mutual intersection of these lines, are important. In addition to the check of the consistency of data for η, which are calculated by formulas (5) and (6), we also take into account the conditions of explosive crystallization [1] in the case of heating of amorphous layers for a number of organic materials. Under atmospheric pressure, the temperature of explosive crystallization T_* is higher than the glass-transition temperature approximately by 15 K and the viscosity of 10^7–10^8 Pa s [1] corresponds to this temperature.

The melting temperature T_0, the fluid viscosity corresponding to this temperature and atmospheric pressure, and the glass-transition temperature $T_{g, at}$ under this pressure are presented in the table for each of the materials under consideration. The values of the melt viscosity at $\frac{T}{T_0} = 0.8$ and 1.5 are also given, and the pressure p_g in the melting line at which the melt undergoes the glass transition is estimated. For the same material, the data of various authors can strongly differ. Thus, for carbon tetrachloride, the value for $T_{g, at} = 61$ K was taken from [11], in which the glass-transition point was estimated from experiments on the crystallization of amorphous layers. The authors of [12] indicate another value, $T_{g, at} = 129$ K, which was obtained by extrapolating glass-transition temperatures for solutions of carbon tetrachloride in ethylbenzene to zero concentration of the second component. At $T_{g, at} = 61$ K, the ratio $\frac{T_{g, at}}{T_0}$ is 0.25; i.e., it is sufficiently lower than the similar ratio for organic materials with a more complicated molecular configuration. For example, in the case of dichlorethane, thiophene, and benzene, we have $\frac{T_{g, at}}{T_0} = 0.40$ [1], 0.39 [1], and 0.47 [12], respectively. The values of $T_{g, at}$, which are indicated in the table for argon and carbon dioxide, are obtained under the assumption that $\frac{T_{g, at}}{T_0} = 0.25$. For dodecane and octadecane, this ratio is assumed to be 0.6. Plotting the isoviscous curves (Fig. 2), we can expect their nonlinearity in the region of negative pressures. Indeed, only in this case is their intersection impossible. Under high pressures, $p \approx p_*$, the lines of constant viscosity in coordinates T, p are close to straight lines. This property is also confirmed experimentally for the glass-transition line [13]. Solving the question on the fluid glass transition in the melting line, we adhered to the following rule. Let the parameter p_* in the Simon equation (2) be taken as a scaling value for pressure. This parameter serves as a characteristic of the internal pressure in the condensed phase [3, 4] for each of the materials. We assume that the liquid undergoes the glass transition in the melting line if the glass-transition line $\eta(T, p) = 10^{12}$ Pa s, in its extrapolation, intersects the melting line

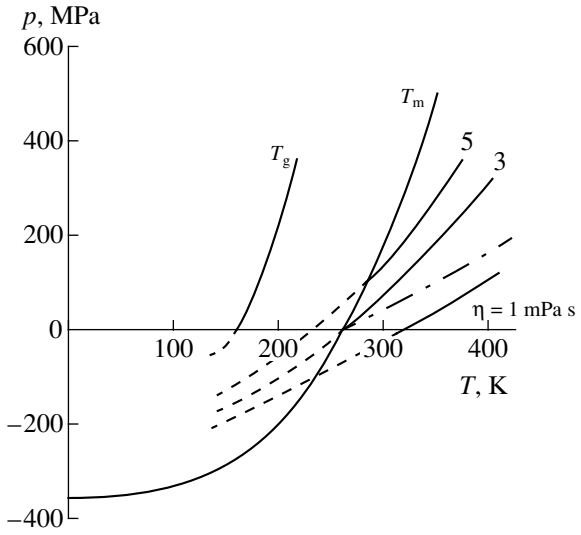

Fig. 2. Dodecane melting line $T_m(p)$, viscosity isolines η = 1, 3, 5 mPa s, and $T_g(p)$ for $\eta = 10^{12}$ Pa s with extrapolation to the region of negative pressures. The dashed-dotted line is the isochore $\nu = 1.3$ cm^3/g of the liquid.

Viscosity of liquids at various points of the melting line and the glass-transition temperature $T_{g, at}$ under atmospheric pressure

Material	T_0, K	$\eta(T = 0.8T_0)$, mPa s	$\eta(T = T_0)$, mPa s	$\eta(T = 1.5T_0)$, mPa s	p_g, GPa s	$\frac{p_g}{p_*}$	$T_{g, at}$, K
Carbon tetrachloride	250.6	1.8	2.0	2.7			61
Benzene	278.6	0.3	0.82	3.8	6.5	18.1	131
Dodecane	263.7	0.6	2.8	20.1	5.3	14.9	160
Octadecane	301.0	1.3	4.0	55	2.7	7.9	181
Carbon dioxide	216.6	0.15	0.25	0.59			54
Argon	83.8	0.20	0.28	0.47			21

$T = f_m(p)$ at a pressure $\frac{p}{p_*} < 20$. In the opposite case, the question remains open since the validity of the procedure employed becomes unreliable. For the substances listed in the table, argon, carbon dioxide, and carbon tetrachloride can be related to this case.

Thus, the analysis of the behavior of the fluid viscosity, which was undertaken by us, yields the following pattern for the variation of η in the melting line with allowance for its continuation far beyond the triple point. The liquid retains the high fluidity $\frac{1}{\eta}$ in the low-temperature (metastable) region of the melting line, which is caused by the omnidirectional extension of coexisting phases. The melt viscosity monotonically increases with temperature, and in the vicinity of a certain point of the melting line $\{T, p\}_{m, g}$, the liquid can undergo the glass transition. This conclusion has not only a cognitive but a practical meaning, e.g., for metallurgy and geophysics. For example, in [14], on the basis of extrapolating the iron melting line to $p \approx 300$ GPa, a conclusion was made as to the vitreous state of the Earth's core. This conclusion requires additional analysis, but the approach, in itself, confirms the necessity of further study of the fluid viscosity in the melting line within a wide range of temperatures and pressures for various materials.

ACKNOWLEDGMENTS

This work was supported by the Russian Foundation for Basic Research, project no. 00-02-16227.

REFERENCES

1. V. P. Skripov and V. P. Koverda, *Spontaneous Crystallization of Supercooled Liquids* (Nauka, Moscow, 1984).
2. V. P. Skripov and M. Z. Faizullin, High Temp.-High Press **18** (3), 1 (1986).
3. F. E. Simon and G. Glatzel, Z. Anorg. Chem. **178**, 309 (1929).
4. V. P. Skripov and M. Z. Faĭzullin, Teplofiz. Vys. Temp. **37**, 814 (1999).
5. A. I. Bachinskiĭ, *Selected Papers* (Akad. Nauk SSSR, Moscow, 1960).
6. N. J. Trappeniers, P. S. van der Gulik, and H. van den Hooff, Chem. Phys. Lett. **70**, 438 (1980).
7. M. A. McCool and L. A. Woolf, J. Chem. Soc., Faraday Trans., Part 1, No. 10, 1971 (1972).
8. H. J. Parkhurst and J. Jonas, J. Chem. Phys. **63**, 2705 (1975).
9. D. L. Hogenboom, W. Webb, and J. A. Dixon, J. Chem. Phys. **46**, 2586 (1967).
10. S. A. Ulybin and W. Makarushkin, in *Proceedings of the VII Symposium on Thermophysical Properties, Gaithersburg (Md), 1977* (New York, 1977), p. 678.
11. H. Suga and S. Seki, J. Non-Cryst. Solids **16** (2), 171 (1974).
12. C. A. Angell, J. M. Sare, and E. J. Sare, J. Phys. Chem. **82**, 2622 (1978).
13. T. Atake and C. A. Angell, J. Phys. Chem. **83**, 3218 (1979).
14. V. V. Brazhkin and A. G. Lyapin, Usp. Fiz. Nauk **170**, 535 (2000).

Translated by T. Galkina

Doklady Physics, Vol. 46, No. 6, 2001, pp. 407–409. Translated from Doklady Akademii Nauk, Vol. 378, No. 6, 2001, pp. 751–753.

PHYSICS

Exact Dispersion Equations for Waveguide Modes of a Graded-Index Optical Fiber

V. I. Krivenkov

Presented by Academician E.M. Dianov January 4, 2001

Received December 20, 2000

Because of a series of technological (sometimes, occasional) reasons, the profile of the refractive index for actual optical fibers has a fairly complicated form. When evaluating the dispersion characteristics of an actual optical fiber, all the features of its refractive index need not be allowed for, because many of them are random in nature and would not noticeably influence the calculation results.

A graded-index fiber with an arbitrary refractive index is the optimum mathematical model for actual graded-index fibers, which are widely used in various optical-fiber devices. In this paper, we derive both exact dispersion equations and equations for the critical wavelengths of all the waveguide modes of a graded-index fiber with an arbitrary refractive-index profile. In fact, we develop a method for evaluating the dispersion characteristics for graded-index fibers that is more efficient than known methods (they were analyzed in monograph [1]). Within the framework of the model proposed, this method has the maximum range of use; in addition, it is exact, fairly simple, and efficient.

APPROXIMATION FOR THE REFRACTIVE-INDEX PROFILE

We consider a graded-index fiber consisting of a core, whose permittivity is given by a piecewise continuous function $\varepsilon(r)$ (in the cylindrical coordinate system r, φ, and z, with z being the guide axis), and of an infinitely thick cladding with a constant permittivity ε_{00}. Without loss of generality, we assume that the function $\varepsilon(r)$ is continuous from the right at the discontinuity points, including the point $r = 0$.

Omitting intermediate transformations based on interpolation with the optimum sampling of its points, we present the permittivity for this fiber in the following form:

$$\varepsilon(r) = \begin{cases} \sum_{k=0}^{\infty} \varepsilon_{ik} \left(\frac{r - r_{i-1}}{r_i - r_{i-1}} \right)^k, & r_{i-1} \le r \le r_i, \quad i = 1, 2, \ldots, N \\ \varepsilon_{00}, & r_N \le r < \infty. \end{cases}$$

Here, $r_0 = 0, r_1, r_2, \ldots, r_{N-1}$ are the discontinuity points of the function $\varepsilon(r)$, r_N is the core radius,

$$\varepsilon_{ik} = \lim_{M \to \infty} \sum_{n=k}^{M} 2^{\operatorname{sgn}(n)} a_{in}^M t_{nk},$$

$$t_{n-1,0} = (-1)^{n-1}, \quad t_{nn} = 2^{2n-1},$$

$$t_{n+1,k} = 4t_{n,k-1} - 2t_{nk} - t_{n-1,k},$$

$$1 \le k \le n, \quad n = 1, 2, \ldots, \quad t_{n-1,n} = 0,$$

$$a_{in}^M = \frac{1}{M+1} \sum_{j=0}^{M} \varepsilon(r_{ij}) \cos \frac{(2j+1)n\pi}{2(M+1)},$$

$$r_{ij} = \frac{r_i + r_{i-1}}{2} + \frac{r_i - r_{i-1}}{2} \cos \frac{(2j+1)\pi}{2(M+1)}.$$

Such an interpolation (with the optimum sampling of its points) can be used to most closely represent the permittivity for a fiber core as a power series only if the refractive-index profile for this fiber is given analytically. If the refractive-index profile for a graded-index fiber is given in the form of tabulated values, other methods (for example, a step-function approximation [2–4]) have to be employed.

DISPERSION EQUATIONS

In what follows, we omit the factor $\exp[j(\omega t - \beta z + m\varphi)]$, which describes the common dependence of the electric and magnetic field strengths, $\mathbf{E} = (E_r, E_\varphi, E_z)$ and $\mathbf{H} = (H_r, H_\varphi, H_z)$, respectively, on the time t and coordinates z and φ of a waveguide mode with the azimuthal number m. Here, ω and β are the circular fre-

Moscow State Academy of Instrumentation Engineering and Informatics, ul. Stromynka 20, Moscow, 107846 Russia

1028-3358/01/4606-0407$21.00

quency and the longitudinal-propagation constant for the mode, respectively. In this case, using the Maxwell equations for a nonmagnetic dielectric medium, we obtain the following set of equations:

$$\varepsilon(r)r\frac{d\mathbf{e}}{dr} = \mathbf{A}(r)\mathbf{h},$$

$$r\frac{d\mathbf{h}}{dr} = \mathbf{A}(r)\mathbf{e}.$$

Here,

$$\mathbf{e} = j\sqrt{\varepsilon_0}\begin{pmatrix} E_z \\ k_0 r E_\varphi \end{pmatrix}, \quad \mathbf{h} = \sqrt{\mu_0}\begin{pmatrix} H_z \\ k_0 r H_\varphi \end{pmatrix},$$

$$\mathbf{A}(r) = \begin{pmatrix} m\gamma & \gamma^2 - \varepsilon(r) \\ k_0^2 r^2 \varepsilon(r) - m^2 & -m\gamma \end{pmatrix},$$

$$\gamma = \frac{\beta}{k_0}, \quad k_0 = \omega\sqrt{\varepsilon_0\mu_0} = \frac{2\pi}{\lambda},$$

ε_0 and μ_0 are the dielectric and magnetic constants, respectively, and λ is the wavelength.

Taking into account that the components of the vectors **E** and **H** must tend to zero more rapidly than r^{-1} as $r \longrightarrow \infty$, we present a continuous solution to this set of equations in the following form:

$$\begin{pmatrix} \mathbf{e}(r) \\ \dots \\ \mathbf{h}(r) \end{pmatrix} = \begin{cases} \sum_{l=1}^{2}\sum_{k=0}^{\infty} c_l \begin{pmatrix} \mathbf{e}_{ik}^l \\ \dots \\ \mathbf{h}_{ik}^l \end{pmatrix} \left(\frac{r - r_{i-1}}{r_i - r_{i-1}}\right)^{m[1-\mathrm{sgn}(i-1)]+k}, \\ r_{i-1} \le r < r_i, \quad i = 1, 2, \dots, N \\ c_3 \begin{pmatrix} \mathbf{e}_0(r) \\ \dots \\ \mathbf{h}_0(r) \end{pmatrix} + c_4 \begin{pmatrix} \mathbf{h}_0(r) \\ \dots \\ \varepsilon_{00}\mathbf{e}_0(r) \end{pmatrix}, \quad r_N \le r < \infty. \end{cases}$$

Here,

$$\mathbf{e}_{10}^1 = \begin{pmatrix} 1 \\ 0 \end{pmatrix}, \quad \mathbf{h}_{10}^1 = \mathrm{sgn}(m)\begin{pmatrix} \gamma \\ -m \end{pmatrix},$$

$$\mathbf{e}_{10}^2 = \mathbf{h}_{10}^1, \quad \mathbf{h}_{10}^2 = \varepsilon_{10}\mathbf{e}_{10}^1,$$

$$\begin{pmatrix} \mathbf{e}_{1k}^l \\ \dots \\ \mathbf{h}_{1k}^l \end{pmatrix} = \frac{1}{\varepsilon_{10}k(2m+k)}\mathbf{C}_k \sum_{j=0}^{k-1} \mathbf{B}_{kj} \begin{pmatrix} \mathbf{e}_{1j}^l \\ \dots \\ \mathbf{h}_{1j}^l \end{pmatrix},$$

$$\mathbf{C}_k = \left(\begin{array}{c|c} (m+k)\mathbf{I} & \mathbf{A}_{10} \\ \hline \mathbf{A}_{10} & \varepsilon_{10}(m+k)\mathbf{I} \end{array}\right),$$

$$\mathbf{A}_{10} = \begin{pmatrix} m\gamma & \gamma^2 - \varepsilon_{10} \\ -m^2 & -m\gamma \end{pmatrix},$$

$$\mathbf{B}_{kj} = \left(\begin{array}{c|c} -(m+j)\varepsilon_{1,k-j}\mathbf{I} & \mathbf{A}_{1,k-j} \\ \hline \mathbf{A}_{1,k-j} & [0] \end{array}\right),$$

$$\mathbf{A}_{1n} = \begin{pmatrix} 0 & -\varepsilon_{1n} \\ k_0^2 r_1^2 \varepsilon_{1,n-2} & 0 \end{pmatrix}, \quad n = 1, 2, \dots, \quad \varepsilon_{1,-1} = 0,$$

$$k = 1, 2, \dots, \quad l = 1, 2,$$

I and [0] are the unit and zero matrices of the second rank, respectively. In addition,

$$\mathbf{e}_{i0}^l = \sum_{j=0}^{\infty} \mathbf{e}_{i-1,j}^l, \quad \mathbf{h}_{i0}^l = \sum_{j=0}^{\infty} \mathbf{h}_{i-1,j}^l,$$

$$\mathbf{e}_{i,k+1}^l = \frac{\Delta r_i}{r_{i-1}\varepsilon_{i0}(k+1)}$$

$$\times \sum_{j=0}^{k}\left[-j\left(\varepsilon_{i,k-j} + \frac{r_{i-1}}{\Delta r_i}\varepsilon_{i,k-j+1}\right)\mathbf{e}_{ij}^l + \mathbf{A}_{i,k-j}\mathbf{h}_{ij}^l\right],$$

$$\mathbf{h}_{i,k+1}^l = \frac{\Delta r_i}{r_{i-1}(k+1)}\left(\sum_{j=0}^{k}\mathbf{A}_{i,k-j}\mathbf{e}_{ij}^l - k\mathbf{h}_{ik}^l\right),$$

$$\mathbf{A}_{i0} = \begin{pmatrix} m\gamma & \gamma^2 - \varepsilon_{i0} \\ k_0^2 r_{i-1}^2 \varepsilon_{i0} - m^2 & -m\gamma \end{pmatrix},$$

$$\mathbf{A}_{in} = \begin{pmatrix} 0 & -\varepsilon_{in} \\ 2k_0^2 r_{i-1}^2 \sum_{j=0}^{2} \frac{(\Delta r_i / r_{i-1})^j}{j!(2-j)!}\varepsilon_{i,n-j} & 0 \end{pmatrix},$$

$$n = 1, 2\dots, \quad \varepsilon_{i,-1} = 0, \quad \Delta r_i = r_i - r_{i-1},$$

$$k = 0, 1, \dots, \quad i = 2, 3, \dots, N, \quad l = 1, 2,$$

$$\mathbf{e}_0(r) = \begin{pmatrix} 0 \\ r\frac{dK_m(\rho r/r_N)}{dr} \end{pmatrix}, \quad \mathbf{h}_0(r) = \begin{pmatrix} u^2 K_m(\rho r/r_N) \\ -m\gamma K_m(\rho r/r_N) \end{pmatrix},$$

$$\rho = k_0 u r_N, \quad u^2 = \gamma^2 - \varepsilon_{00} > 0,$$

$K_m(\rho r/r_N)$ is the MacDonald function of the integer order m, and c_1, c_2, c_3, and c_4 is a nontrivial solution to the homogeneous system of equations

$$\mathbf{G}\begin{pmatrix} c_1 \\ c_2 \end{pmatrix} = \left(\begin{array}{c:c} \mathbf{e}_0(r_N) & \mathbf{h}_0(r_N) \\ \hdashline \mathbf{h}_0(r_N) & \varepsilon_{00}\mathbf{e}_0(r_N) \end{array}\right)\begin{pmatrix} c_3 \\ c_4 \end{pmatrix},$$

where

$$\mathbf{G} \equiv (g_{ij}) = \sum_{k=0}^{\infty}\left(\begin{array}{c:c} \mathbf{e}^1_{Nk} & \mathbf{e}^2_{Nk} \\ \hdashline \mathbf{h}^1_{Nk} & \mathbf{h}^2_{Nk} \end{array}\right)$$

is a matrix whose determinant must be zero.

We eliminate the unknowns c_3 and c_4 from this set of equations and, then, set the determinant of the system obtained equal to zero. As a result, we arrive at the equation

$$\det\left[\left(\begin{array}{c:c} \varepsilon_{00}\mathbf{e}_1 & \mathbf{h}_1 \\ \hdashline \mathbf{h}_1 & \mathbf{e}_1 \end{array}\right)\mathbf{G}\right] = 0,$$

where

$$\mathbf{e}_1 = (mK_m(\rho) + \rho K_{m-1}(\rho), 0),$$

$$\mathbf{h}_1 = (m\gamma K_m(\rho), u^2 K_m(\rho)).$$

This is a dispersion equation for the symmetric modes H_{0n} and E_{0n} or for the hybrid modes HE_{mn} and EH_{mn} when $m = 0$ or $m = 1, 2, \ldots$, respectively, with $n = 1, 2, \ldots$.

For $m = 0$, this equation is reduced to two independent equations:

$$\varepsilon_{00}\rho K_1(\rho)g_{11} + u^2 K_0(\rho)g_{41} = 0$$

and

$$\rho K_1(\rho)g_{32} + u^2 K_0(\rho)g_{22} = 0,$$

which are dispersion equations for the modes E_{0n} and H_{0n}, respectively ($n = 1, 2, \ldots$).

EQUATIONS FOR THE CRITICAL WAVELENGTHS

For a waveguide mode of a fiber, the dispersion equation implicitly determines the dependence $\beta(\lambda)$ for this mode. The exact upper bound for the wavelengths satisfying the condition $\lambda\beta(\lambda) > 2\pi\sqrt{\varepsilon_{00}}$ (with $u^2 > 0$) is the critical wavelength for this mode.

We proceed to the limit $\gamma \longrightarrow \sqrt{\varepsilon_{00}}$ in the dispersion equations obtained. As a result, we arrive at the equations

$$g_{11}(\lambda) = 0, \quad g_{32}(\lambda) = 0,$$

$$g_{11}(\lambda)g_{32}(\lambda) - g_{12}(\lambda)g_{31}(\lambda) = 0,$$

$$\det\left[\left(\begin{array}{c:c} \varepsilon_{00}\mathbf{e}_c & \mathbf{h}_c \\ \hdashline \mathbf{h}_c & \mathbf{e}_c \end{array}\right)\mathbf{G}(\lambda)\right] = 0,$$

with

$$\mathbf{e}_c = \left(\frac{2\pi^2\sqrt{\varepsilon_{00}}r_N^2}{\lambda^2(m-1)}, -1\right),$$

$$\mathbf{h}_c = \left(m - \frac{2\pi^2\varepsilon_{00}r_N^2}{\lambda^2(m-1)}, \sqrt{\varepsilon_{00}}\right).$$

These equations determine the critical wavelengths, respectively, for the modes E_{0n}, H_{0n}, HE_{1n} and EH_{1n} ($m = 1$), and HE_{mn} and EH_{mn} ($m = 2, 3, \ldots$), with $n = 1, 2, \ldots$.

When solving these equations, the wavelength dependence of the refractive-index profile must be taken into account. The problem of determining this dependence is not discussed in this paper because, in each specific case, its solution requires a proper approach. Possible methods of solving this problem were given in [5–7].

REFERENCES

1. M. Adams, *An Introduction to Optical Waveguides* (Wiley, New York, 1981; Mir, Moscow, 1984).
2. P. J. B. Clarricoatts and K. B. Chan, Electron. Lett. **6**, 694 (1970).
3. A. S. Belanov and V. I. Krivenkov, Radiotekh. Élektron. **39** (1), 31 (1994).
4. A. S. Belanov, E. M. Dianov, and V. I. Krivenkov, Dokl. Akad. Nauk **364**, 37 (1999) [Dokl. Phys. **44**, 1 (1999)].
5. D. Gloge, Appl. Opt. **10**, 2442 (1971).
6. A. S. Belanov, E. M. Dianov, V. I. Krivenkov, and A. S. Kurilov, Élektrosvyaz', No. 12, 24 (1985).
7. A. S. Belanov, V. I. Krivenkov, and E. A. Kolomiĭtseva, Radiotekhnika, No. 3, 32 (1998).

Translated by V. Chechin

Doklady Physics, Vol. 46, No. 6, 2001, pp. 410–413. Translated from Doklady Akademii Nauk, Vol. 378, No. 6, 2001, pp. 754–757.

PHYSICS

Dissociative Excitation of SrCl Molecules in e-$SrCl_2$ Collisions

Yu. M. Smirnov

Presented by Academician V.V. Osiko February 22, 2001

Received January 18, 2001

1. When devising metal vapor lasers, the use of metal halides is presently considered a promising method of metal-atom injection into a discharge; it is best suited to practical implementation [1]. In this case, for a number of active media, laser action can be gained by utilizing not only transitions of atoms and ions of metals but also molecular transitions of metal monohalides. This is primarily true for monohalides of the IIB-group metals, i.e., for molecules of the MX-type, where M = Zn, Cd, Hg and X = Cl, Br, I.

Dihalides MX_2 provide the initial material for formation of these molecules in plasma. The dissociative electron-impact excitation

$$MX_2 + e \longrightarrow MX^* + X^{(*)} + e' \qquad (1)$$

is a major process for obtaining excited monohalide molecules. Here, e and e' are incident and scattered electrons, respectively. Excited particles are marked by asterisks. Generally, a halogen atom X produced by the dissociation can find itself in the ground state as well as in excited states; for a reasonably high energy of the incident electron, an atomic halogen ion in the ground state or excited states can be produced, etc.

Process (1) is studied for a number of halides of the IIB-group metals (see, e.g., [2, 3]), mainly for mercury halides. A high saturation vapor pressure is characteristic of all these compounds at a temperature not considerably higher than room temperature. The study of collisions between electrons and halides of the IIA-group metals, i.e., alkali-earth metals, is also of interest. Although a reasonably dense vapor can be obtained for these compounds only at temperatures of approximately 1000 K and higher, the advent of lasers and their use as an active medium seems to be a technically tractable problem. However, for performing calculations or, at least, for estimating parameters of such lasers, it is necessary to know the constants that characterize inelastic collisions between electrons and molecules of alkali-earth-metal dihalides. Moreover, in any event, this information is of interest in such divisions of fundamental science as molecular spectroscopy, chemical-bond theory, plasma physics, and chemistry.

Inelastic collisions between slow monoenergetic electrons and $SrCl_2$ molecules that result in the formation of excited molecules of strontium monochloride are experimentally studied in this paper. The author is not aware of theoretical data on the molecule under consideration.

2. The method of extended crossed beams [4, 5] in combination with optical spectroscopy is the basis for the experiment with molecules $SrCl_2$. Among the distinctive features of this method, mention should be made of its high sensitivity and universality. This makes the method a useful tool for studying atoms of virtually all elements, as well as various categories of molecules (oxides, hydroxides, halides, etc.).

To produce a molecular beam, strontium dichloride is placed into a tantalum crucible whose external surface is heated by an electron ray. Defocusing of the ray to approximately 40 mm makes it possible to obtain a more uniform temperature field and to avoid hot spots. At the same time, in the course of the evaporation, the thermal excitation of molecules with filling of rovibrational levels of the ground electronic state of a $SrCl_2$ molecule inevitably occurs. It is well known [6–8] that the cross sections for various electron–molecule collisions depend on the initial vibrational level on which the molecule finds itself prior to its collision with an electron. However, specific results for the processes of dissociative excitation, in particular, for a $SrCl_2$ molecule, have not been published to date.

The evaporation of strontium dichloride proceeds at a temperature of 1200 K, the molecule concentration in the crossing region for the electron and molecular beams being 1.2×10^{10} cm^{-3}. The $SrCl_2$ molecule is characterized by three fundamental oscillations with the fundamental frequencies $\nu_1 = 285$, $\nu_2 = (60)$, and $\nu_3 = 318$ cm^{-1} [9]; the bracketed value was determined in [9] as an estimate. Evidently, the distribution of molecules over the oscillation levels ν_2 turns out to be quite wide under the conditions of our experiment and the individual contribution of an excitation from each of

Moscow Institute of Power Engineering (University of Technology), ul. Krasnokazarmennaya 14, Moscow, 111250 Russia

1028-3358/01/4606-0410$21.00

the oscillation levels to the resulting cross section is relatively small. At the same time, for the oscillations ν_1 and ν_3, the ratio of the populations for two neighboring levels is 0.711 and 0.685, respectively. For these oscillations, at the lowest levels with the oscillation quantum number $\nu' = 0$–5, 85 and 88% of the total number of beam molecules are found, respectively. Therefore, the role of each of the low levels for these oscillations is reasonably large and variation in their population may have a pronounced effect on the resulting cross section. This should be properly accounted for in the subsequent comparison of theoretical data with the present experimental results.

The electron-beam current density was not in excess of 0.8 mA/cm^2 everywhere in the range of operating energies, i.e., from 0 to 100 eV. The width of the electron-energy distribution at the electron-collector entry, measured by the retarding potential method, was not in excess of 1.0 eV in the range of electron energies between 20 and 100 eV (for 90% of the beam electrons).

The spectral resolution is one of the most important experimental factors in studying molecular-spectrum excitation. In the present paper, it was approximately 0.1 nm in the ultraviolet and visible range for $\lambda \leq 600$ nm. For longer wavelengths, the resolution was impaired to 0.2 nm as a result of replacing the diffraction grating, which was caused by the construction parameters of the MDR-3 monochromator.

The remaining experimental conditions are not specific to studying collisions between electrons and $SrCl_2$ molecules; these conditions were discussed earlier [4, 5]. The measurement error of the relative values of the cross section for the studied spectral bands of SrCl was 8–18%. This stems from both their position in the spectrum and the rather complicated structure of the investigated spectral objects. The error in determination of absolute values of cross sections was within the limits from ±25 to ±35%.

3. The optical emission spectrum excited by collisions of electrons with an energy of 100 eV with strontium–dichloride molecules was studied in the spectral range 338–700 nm. Molecular bands are found in the red part of the spectrum within the range 623–688 nm, as well as at the boundary between the visible and ultraviolet regions in the range 391–406 nm. Using data from [10], these band systems are identified as being possessed by the SrCl molecule. The bands of the red system have violet shading and closely spaced series pertaining to the electron transition $A^2\Pi$–$X^2\Sigma^+$. The bands of the ultraviolet system have a red shading and can be assigned to the electron transition $B^2\Sigma^+$–$X^2\Sigma^+$. An efficient generation takes place on this transition in lasers utilizing similar molecules of monohalides of the IIB-group metals.

It is worth noting that the interpretation of the strontium monochloride bands was changed in [11] as compared to the initial paper [10]. In particular, the system $A^2\Pi$–$X^2\Sigma^+$ is considered a result of the superposition of two resonance systems: $A^2\Pi_{1/2}$ (T_e = 15112 cm^{-1}), $A^2\Pi_{3/2}$ (14818 cm^{-1})–$X^2\Sigma^+$(0) and $B^2\Sigma^+$ (15719 cm^{-1})–$X^2\Sigma^+$(0). It is seen that the electron energies T_e for these states differ from one another by 600–900 cm^{-1}, so that, given the large extent of these systems, their partial overlap is inevitable. On the other hand, the system $B^2\Sigma^+$–$X^2\Sigma^+$ from [10] is interpreted in [11] as $C^2\Pi_{1/2,\,3/2}$–$X^2\Sigma^+$. Since the data on the band-border positions are lacking in [11] and the excitation cross sections are found for these bands in the present study, the initial notations from [10] are retained in the table.

Because of a close spacing of the spectral bands, individual bands cannot be isolated at the average spectral resolution of the apparatus, although, in the present study, the resolution is much better than in most other beam experiments. As with the MgCl molecule [12], we succeeded only in resolving sequences. In this case, in the system $A^2\Pi$–$X^2\Sigma^+$, there is a virtually complete spectral overlap for the branches (P_1, Q_1) of the sequence $\Delta v = +1$ and for the branches (P_2, Q_2) of the sequence $\Delta v = -1$.

The measurement results are presented in the table. Here, we indicate the sequence and the values of the oscillation quantum numbers for the upper v' and lower v'' levels, the branch, the wavelength of the band border λ, and the values of the excitation cross section Q^{100} for the electron energy of 100 eV. The classification is given, according to the data of paper [10], for the $^{88}Sr^{35}Cl$ molecule. Two optical excitation functions (OEF) are measured in the electron-energy range 0–100 eV. For these functions, in the column OEF, the number corresponding to the curve numbering in the figure, as well as the wavelength at which the OEF was recorded, is given. The two OEFs related to the sequences 0 in the system $A^2\Pi$–$X^2\Sigma^+$ are very close in shape, as can be seen from the figure.

At low electron energies, the dissociative excitation of the strontium monochloride may be caused by the following reaction channels:

$$SrCl_2 + \longrightarrow e\ SrCl^* + Cl^- \quad (4.48) \qquad (2)$$

$$\longrightarrow SrCl^* + Cl + e' \quad (6.86) \qquad (3)$$

$$\longrightarrow SrCl^* + Cl^* + e' \quad (\sim 16.1) \qquad (4)$$

$$\longrightarrow SrCl^* + Cl^+ + e' + e'' \quad (19.83). \qquad (5)$$

Here, e'' is an electron knocked out from a chlorine atom when it is ionized; the remaining designations correspond to those used earlier for reaction (1). The bracketed numbers following the reaction equations are the minimum calculated values for the appearance energy E_a. When calculating these values, the thermal motion energy, as well as the possibility that a portion of the incident electron energy is transformed into the kinetic energy of heavy particles in the course of the

Dissociative excitation cross sections for sequences of the SrCl molecule

Sequence, Δv	$v' - v''$	Branch	λ, nm	Q_{100}, 10^{-18} cm^2	OEF, no., λ	Sequence, Δv	$v' - v''$	Branch	λ, nm	Q_{100}, 10^{-18} cm^2	OEF, no., λ
System $A^2\Pi$–$X^2\Sigma^+$						System $B^2\Sigma^+$–$X^2\Sigma^+$					
–2	0–2	Q_1	688.08	5.16	–	–2	3–5	R_2	403.85	1.53	–
	…	Q_1	…				…	R_2	…		
	5–7	Q_1	686.15				8–10	R_2	405.05		
–1	0–1	P_1	675.59	12.8	–		3–5	Q_2	403.97		
	…	P_1	…				…	Q_2	…		
	3–4	P_1	674.64				10–12	Q_2	405.62		
	0–1	Q_1	674.50			–1	0–1	R_1	400.84	2.25	–
	…	Q_1	…				…	R_1	…		
	6–7	Q_1	672.65				5–6	R_1	402.29		
0	0–0	P_1	662.01	17.7	1–661.0		0–1	Q_1	400.93		
	1–1	P_1	661.75				…	Q_1	…		
	0–0	Q_1	661.40				5–6	Q_1	402.37		
	…	Q_1	…			–1	0–1	R_2	398.25	3.58	–
	6–6	Q_1	659.64				…	R_2	…		
+1	1–0	P_1	649.10	6.34	–		5–6	R_2	399.68		
	…	P_1	…				0–1	Q_2	398.34		
	4–3	P_1	648.50				…	Q_2	…		
	1–0	Q_1	648.29				4–5	Q_2	399.53		
	…	Q_1	…			0	0–0	R_1	396.08	4.80	–
	6–5	Q_1	647.39				1–1	R_1	396.39		
–1	0–1	P_2	649.10				0–0	Q_1	396.15		
	…	P_2	…				1–1	Q_1	396.47		
	3–4	P_2	648.50			0	0–0	R_2	393.64	8.96	–
	0–1	Q_2	648.24				1–1	R_2	393.93		
	…	Q_2	…				0–0	Q_2	393.71		
	8–9	Q_2	646.69				1–1	Q_2	394.01		
0	0–0	P_2	636.25	14.3	2–636.0	+1	1–0	R_1	391.73	2.65	–
	…	P_2	…				…	R_1	…		
	6–6	P_2	635.26				4–3	R_1	392.73		
	0–0	Q_2	635.89				1–0	Q_1	391.82		
	…	Q_2	…				…	Q_1	…		
	7–7	Q_2	634.73				5–4	Q_1	393.09		
+1	1–0	P_2	624.53	4.50	–						
	…	P_2	…								
	8–7	P_2	623.97								
	1–0	Q_2	623.71								
	…	Q_2	…								
	9–8	Q_2	623.15								

dissociation (production of “hot” particles [13]), was ignored. Reference data on the bond rupture energies and other energy characteristics of particles are taken from [14]. In reaction (4), the chlorine-atom excitation to the same group of lower states as that in paper [12] was considered. All values of E_a are calculated for the branches (P_1, Q_1) of the sequence 0 in the system $A^2\Pi$–$X^2\Sigma^+$.

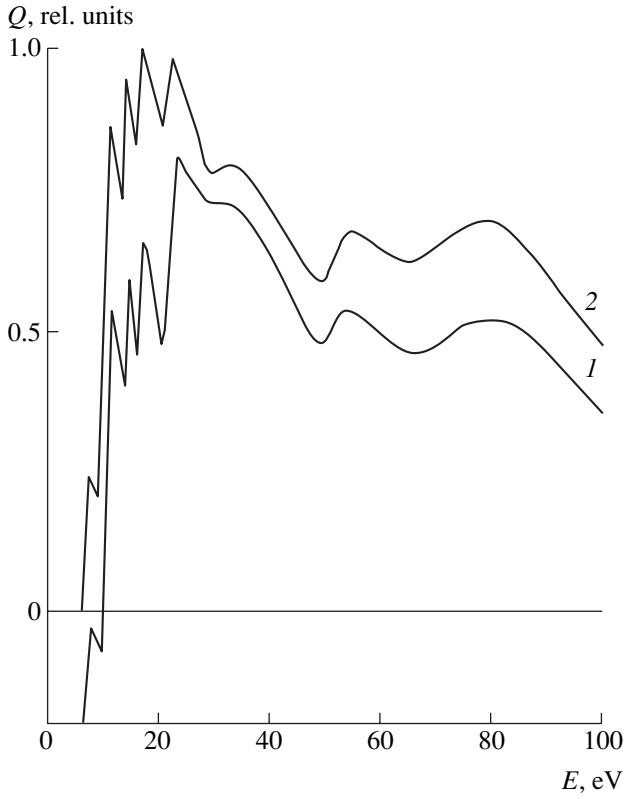

Optical functions of dissociative excitation for a strontium monochloride molecule.

The appearance-energy value measured for the OEF of this sequence is $E_a = 7.0 \pm 0.3$ eV. It correlates well with that calculated for reaction (3). No manifestations of reaction (2) exceeding the noise level were observed; the same situation also holds for the molecules studied earlier. However, the features of the OEF structure associated with reactions (4) and (5) are well pronounced. At the same time, in the energy range 7–16 eV, three peaks are found for both OEFs; their origin remains unclear. These features are not found for the MgCl molecule [12]; however, when studying electron–atom collisions [15], they often appear for the OEF of a strontium atom. Theoretical studies seem to be necessary for interpretating the OEF structure for strontium monochloride in the indicated energy range.

Comparing the results of the present study for strontium monochloride with those obtained earlier [12] for a similar molecule of magnesium monochloride, one can conclude that the absolute values of the dissociative excitation cross sections for bands of the system $A^2\Pi$–$X^2\Sigma^+$ for the MgCl molecule are several times greater than those for the SrCl molecule. The difference is about a factor of two for the sequences –1 and +1 and is close to 3.5 for the most intense sequence 0. The system $B^2\Sigma^+$–$X^2\Sigma^+$ for the MgCl molecule was not studied in [12]. According to the data taken from [11, part 1, p. 392], the state $B^2\Sigma^+$ for the MgCl molecule is much higher than the state $A^2\Pi$ and the transitions $B^2\Sigma^+$–$A^2\Pi$ are observed, whereas the transitions $B^2\Sigma^+$–$X^2\Sigma^+$ are not observed.

REFERENCES

1. G. G. Petrash, Izv. Vyssh. Uchebn. Zaved., Fiz., No. 8, 18 (1999).
2. A. N. Konoplev, N. N. Chavarga, V. N. Slavik, and V. S. Shevera, Pis'ma Zh. Tekh. Fiz. **15**, 48 (1989) [Sov. Tech. Phys. Lett. **15**, 892 (1989)].
3. M. F. Mahmood, J. Phys. D **23**, 1019 (1990).
4. Yu. M. Smirnov, *Physics of Electron and Atomic Collisions* (Fiz.-Tekh. Inst. Akad. Nauk SSSR, Leningrad, 1985), pp. 183–193.
5. Yu. M. Smirnov, J. Phys. II **4** (1), 23 (1994).
6. R. Celiberto and T. N. Rescigno, Phys. Rev. A **47** (3), 1939 (1993).
7. R. Celiberto, U. T. Lamanna, and M. Capitelli, Phys. Rev. A **50**, 4778 (1994).
8. S. A. Pozdneev, Zh. Éksp. Teor. Fiz. **117**, 35 (2000) [JETP **90**, 30 (2000)].
9. K. S. Krasnov, N. V. Filippenko, V. A. Bobkova, *et al.*, *Molecular Constants of Inorganic Compounds* (Khimiya, Leningrad, 1979), p. 84.
10. A. E. Parker, Phys. Rev. **47** (3), 349 (1935).
11. K. P. Huber and G. Herzberg, *Molecular Spectra and Molecular Structure*, Vol. IV: *Constants of Diatomic Molecules* (Van Nostrand Reinhold, New York, 1979; Mir, Moscow, 1984), Part 2.
12. Yu. M. Smirnov, Khim. Yys. Énerg. **33**, 405 (1999).
13. T. K. Karasheva, D. K. Otorbaev, V. N. Ochkin, *et al.*, Tr. Fiz. Inst. Akad. Nauk SSSR **157**, 124 (1985).
14. L. V. Gurevich, G. V. Karachevtsev, V. N. Kondrat'ev, Yu. A. Lebedev, V. A. Medvedev, V. K. Potapov, and Yu. S. Khodeev, *Bond-Rupture Energies. Ionization Potentials and Electron Affinity* (Nauka, Moscow, 1974), p. 152, p. 227, p. 291.
15. V. P. Starodub, I. S. Aleksakhin, I. I. Garga, and I. P. Zapesochnyĭ, Opt. Spektrosk. **35**, 1037 (1973).

Translated by V. Tsarev

Doklady Physics, Vol. 46, No. 6, 2001, pp. 414–417. Translated from Doklady Akademii Nauk, Vol. 378, No. 4, 2001, pp. 479–482.

TECHNICAL PHYSICS

Propagation of Longitudinal Acoustic Waves in a Thin Elastic Strip Coated by a Layer of a Viscous Liquid

S. L. Bazhenov*, A. K. Rogozinskiĭ, and Corresponding Member of the RAS A. A. Berlin****

Received by December 21, 2000

In [1, 2], we observed an effect of decreasing propagation velocity of longitudinal sound waves in a fine elastic rod after its immersion in a liquid. The decrease in the sound velocity is governed by the so-called boundary layer of the liquid, which vibrates together with the rod as an associated mass. The thickness of this layer depends on both the vibration frequency and both the density and viscosity of the liquid. At a sound signal frequency of about 100 kHz, the typical value of the boundary layer thickness for technical oils is 10 to 50 μm [1]. Therefore, the decrease in the sound velocity is considerable only for thin samples, i.e., samples whose thickness does not exceed a few hundreds of microns.

Since the thickness of the boundary layer depends on the viscosity of a liquid, it is appropriate to employ the above effect for determining the viscosity. An advantage of this method is the possibility of performing high-rate viscosity measurements that attain a rate of up to several thousands per second. Such high rates make it possible to measure the viscosity even in the case when it varies with time.

The problem of the effect of a liquid on the propagation velocity and the damping of acoustic waves in a thin strip immersed into an infinite volume of a liquid was solved analytically [1]. However, there exists the problem of controlling the behavior of polymeric resins deposited in liquid form on a metal surface and solidified on it.

The goal of this study is to theoretically solve the problem related to the propagation of a longitudinal harmonic acoustic wave in a thin elastic strip coated by a layer of an incompressible Newtonian liquid.

We introduce a system of coordinates such that the free surface of a liquid coincides with the plane $X = 0$. The longitudinal vibrations of the elastic strip along the *Y*-axis are described by the equation [3–5]

$$\rho_0 H\frac{\partial^2 u}{\partial t^2} = EH\frac{\partial^2 u}{\partial y^2} + \tau. \qquad (1)$$

Here, u is the displacement of a small strip element from the equilibrium position; ρ_0 and E are the strip density and the elastic modulus, respectively; τ is the shear stress describing the action of the liquid on the strip; and H is the strip thickness (Fig. 1a). We note that the shear stress τ is doubled during two-sided depositing of the liquid (Fig. 1b). In this case, H is half the elastic-strip thickness.

In order to find the stress τ, we consider the shear vibrations of the liquid in the case of the strip with the

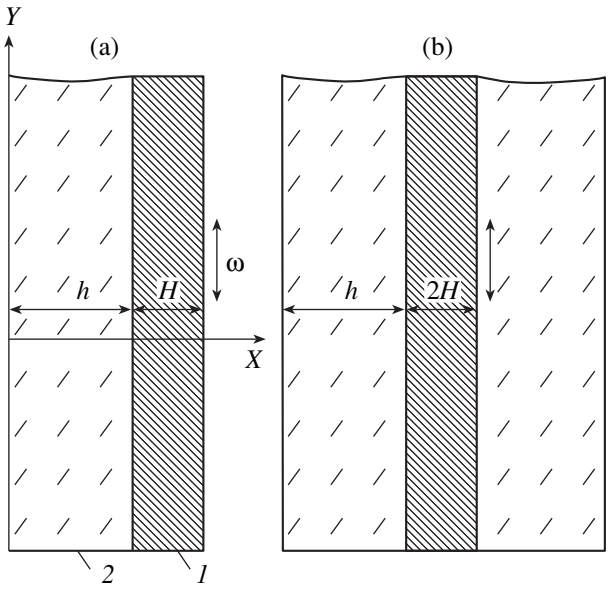

Fig. 1. Calculation scheme: (a) (*1*) elastic rod, (*2*) liquid, (*H*) strip thickness, and (*h*) liquid-layer thickness; (b) two-sided deposited liquid layer.

* *Institute of Synthetic Polymeric Materials, Russian Academy of Sciences, Profsoyuznaya ul. 70, Moscow, 117393 Russia*

** *Semenov Institute of Chemical Physics, Russian Academy of Sciences, ul. Kosygina 4, Moscow, 117977 Russia*

1028-3358/01/4606-0414$21.00

thickness $0 < x < h$, where h is the thickness of the liquid layer. The motion of the liquid is described by the equation [6]

$$\rho\frac{\partial v}{\partial t} = \eta\frac{\partial^2 v}{\partial x^2}. \quad (2)$$

Here, v is the velocity of the liquid along the axis of strip longitudinal vibrations (i.e., the *Y*-axis) and ρ and η are the density and viscosity of the liquid, respectively. The solution to Eq. (2) is sought in the form

$$v = q(x)\exp(-i\omega t), \quad (3)$$

where ω is the circular frequency of strip vibrations. Substituting v into (2), we obtain

$$-i\omega\rho q = \eta\frac{d^2 q}{dx^2}. \quad (4)$$

The boundary conditions have the form $v = \dfrac{\partial u}{\partial t}$ at $x = h$ and $\dfrac{dq}{dx} = 0$ at $x = 0$. The first condition provides equal velocities of the motion for the liquid and the strip at their interface $x = h$. The second condition follows from the absence of forces on the free boundary $x = 0$. With allowance for the boundary conditions, the solution to Eq. (4) has the form

$$q = q_0\cosh(ik_x x), \quad (5)$$

where q_0 is the integration constant and

$$k_x = (1 + i)\sqrt{\frac{\omega\rho}{2\eta}}.$$

Equation (5) determines the shear wave in the liquid that is generated by strip longitudinal vibrations.

The stress produced by the action of the liquid on the strip is equal to that in the liquid taken with the opposite sign: $\tau = -\eta\dfrac{\partial q}{\partial x}$ at $x = h$,

$$\tau = -iq_0\eta k_x\sinh(ik_x h). \quad (6)$$

We seek the solution to Eq. (1) for the longitudinal vibrations of the strip in the form

$$u = u_0\exp[-i(\omega t - ky)],$$

where k is the wave number. Then, the strip velocity is determined by the relationship

$$v = -i\omega u_0\exp[-i(\omega t - ky)]. \quad (7)$$

We assume that the length of the longitudinal wave in the strip $\left(\lambda = \dfrac{2\pi}{k}\right)$ greatly exceeds the transverse wave in the liquid. Taking $y = 0$ with due regard to the equality of the velocities of the liquid and the strip at their interface $x = h$, we find

$$-i\omega u_0 = q_0\cosh(ik_x h). \quad (8)$$

Substituting relationships (6) and (8) into the wave equation (1), we arrive at the dispersion relation

$$\rho_0 H\omega^2 = EHk^2 + \eta k_x\omega\tanh(ik_x h). \quad (9)$$

In an elastic material, the elasticity modulus and the sound velocity are bound by the relation [7]

$$E = \rho_0 c_0^2, \quad (10)$$

where c_0 is the sound velocity in a strip free of liquid. Taking into account that the hyperbolic tangent is determined by the equality [8, 9]

$$\tanh(x - iy) = \frac{\sinh 2x - i\sin 2y}{\cosh 2x + \cos 2y},$$

where x and y are real-valued quantities, the solution to Eq. (9) has the form

$$k = \frac{\omega}{c_0}\sqrt{1 + \alpha + i\beta}, \quad (11)$$

where

$$\alpha = \sqrt{\frac{\rho\eta}{2\omega H^2\rho_0^2}}\frac{\sinh 2\varphi + \sin 2\varphi}{\cosh 2\varphi + \cos 2\varphi}, \quad (12)$$

$$\beta = \sqrt{\frac{\rho\eta}{2\omega H^2\rho_0^2}}\frac{\sinh 2\varphi - \sin 2\varphi}{\cosh 2\varphi + \cos 2\varphi}, \quad \varphi = \sqrt{\frac{\omega\rho}{2\eta}}h. \quad (13)$$

As is known, the phase velocity of the longitudinal wave can be found as a ratio of the circular frequency to the modulus of the wave number k:

$$c = \frac{c_0}{\sqrt[4]{(1 + \alpha)^2 + \beta^2}}. \quad (14)$$

The wave damping is determined by the complex part of the wave number k. If the damping is weak and $\beta \ll 1$, the wave amplitude is described by the relationship

$$u = u_0\exp\left(-\frac{\omega\beta y}{2c_0}\right). \quad (15)$$

Apart from the problem of determining the velocity and damping coefficient for the acoustic wave (with the help of parameters relevant to the strip and liquid), we can also solve the inverse problem, i.e., find the viscosity of the liquid using the velocity and wave damping coefficient. To do this, it is necessary to solve Eqs. (12)–(14), which is possible, in the general case, only numerically. Nevertheless, in asymptotic cases of extremely small and extremely large thicknesses of a liquid, the problem can be solved analytically.

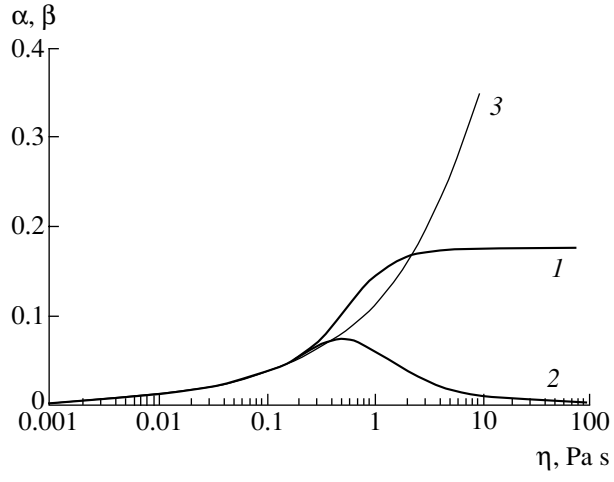

Fig. 2. Coefficients (*1*) α and (*2*) β as functions of the viscosity of a liquid. The calculation was performed for an aluminum strip 100 μm thick, which had been coated by a liquid layer with a density of 900 kg/m^3 and thickness of 30 μm; (*3*) α and β for the infinite volume of a liquid.

For a very large layer thickness, the length of the transverse wave

$$\lambda_x = \frac{2\pi}{k_x} = \sqrt{\frac{4\pi^2\eta}{\omega\rho}}$$

is negligibly small compared to the thickness of the liquid layer. Then, the relationships

$$\varphi \gg 1, \quad \tanh 2\varphi = 1,$$
$$\sin 2\varphi \ll \sinh 2\varphi, \quad \cos 2\varphi \ll \cosh 2\varphi$$

are satisfied. In this case,

$$\alpha = \beta = \sqrt{\frac{\rho\eta}{2\omega H^2\rho_0^2}}.$$

Thus, the problem is reduced to solving that for an elastic strip with a thickness $2H$ immersed in an infinite volume of a liquid [1]. This is evident since the last problem is a particular case of that being solved in this study. Using the results of [1], we find

$$c = c_0\left(1 - \sqrt{\frac{\rho\eta}{8\omega H^2\rho_0^2}}\right). \tag{16}$$

The solution to the inverse problem is

$$\eta = \frac{8\omega H^2\rho_0^2(c_0 - c)^2}{\rho c_0^2}. \tag{17}$$

The second asymptote of solution (11)–(13) corresponds to a very thin liquid layer. If the thickness of the liquid is much smaller than the length λ_x of the transverse wave, then the inequality $\varphi \ll 1$ holds. Expanding the function $\tanh x = x - \frac{x^3}{3} + \frac{2x^5}{15}$ into a series [8], we reduce Eq. (9) to the form

$$c = \frac{c_0}{\sqrt{1 + \frac{\rho h}{\rho_0 H} - \frac{2\omega^2\rho^3 h^5}{15\eta^2\rho_0 H}}}. \tag{18}$$

The viscosity of the liquid is determined by the formula

$$\eta = \sqrt{\frac{2\omega^2\rho^3 h^5 c^2}{15(c^2\rho_0 H + c^2\rho h - c_0^2\rho_0 H)}}. \tag{19}$$

Ignoring the subtrahend in the denominator of Eq. (18), we have

$$c_1 = c_0\sqrt{\frac{m_0}{m_0 + m}}, \tag{20}$$

where $m = \rho h$ and $m_0 = \rho_0 H$ are masses of the liquid and the strip, respectively. Thus, the physical meaning of Eq. (20) is the following. At a small thickness ($h \ll \lambda_x$) of the liquid layer, the entire liquid vibrates as an associated mass together with the strip. In this case, the sound velocity is determined only by the mass (thickness) of the liquid and is independent of its viscosity. As is seen from the more exact equation (18), such a dependence does take place but is rather weak.

It is worth noting that Eq. (20) is derived from the classical formula (10), provided that the rod–liquid system is assumed to be a homogeneous composite material with averaged stiffness and density. In this sense, Eq. (20) is an analog of the so-called mixture rule. According to this rule, the stiffness E_c and the density ρ_m of the armored composite material are determined by averaging characteristics of the armor and the matrix [10]:

$$\rho_c = V\rho + V_0\rho_0 \text{ and } E_c = VE + V_0E_0,$$

where V and V_0 are the volume fraction of the matrix (liquid) and the armor, respectively.

The relationship (18) for the sound velocity involves the thickness of the liquid layer in the fifth power. Hence, in the case of a thin layer (or high viscosity) of a liquid, the variation in the layer thickness results in significant errors while determining the viscosity. Therefore, the viscosity determination based on the damping of sound waves can turn out more exact than that based on their velocity.

Figure 2 shows the coefficients α (curve *1*) and β (curve *2*), which were calculated according to formulas (12) and (13), as functions of the viscosity η of a liquid. It is clearly seen that the coefficient α monotonically rises and attains its asymptotic limit at a large viscosity. For comparison, curve *3* illustrates the behavior of the same parameters for the infinite volume of the liquid, i.e., when $\alpha = \beta$. It is worth noting the existence

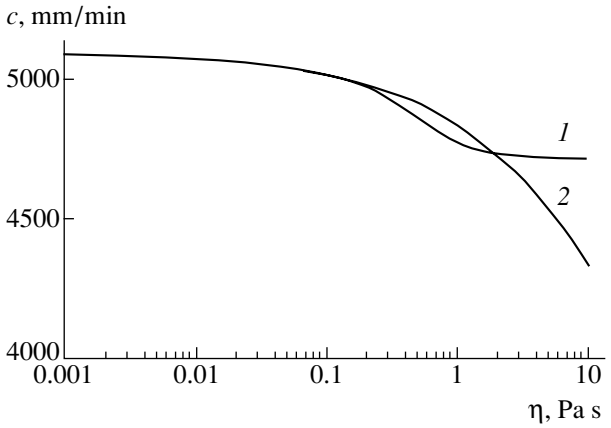

Fig. 3. Sound velocity as a function of the viscosity of a liquid. The cases of *1* and *2* correspond to a finite and infinite volume of a liquid, respectively.

of a region in which the coefficient α is higher than that in the case of infinite volume of the liquid.

The damping (curve *2*) has a maximum corresponding to the value $\varphi = 1.13$ when the thickness of the liquid layer is roughly $\frac{1}{5}$ of the transverse-wave length. We recorded experimentally a region characterized by a high damping while studying the process of solidifying an epoxy resin on an aluminum substrate. In this region, we even observed the disappearance of a signal. We note also a region in which the coefficient β is slightly higher than that for the infinite volume of a liquid.

A weak damping at the low viscosity of the liquid is caused by a small value of the associated mass of the liquid. The weakening of the damping at a very high viscosity is explained by the fact that the shear displacement $\frac{dq}{dx}$ of the liquid decreases, which follows from Eq. (5) for small parameters $k_x x$. In this case, the entire liquid vibrates together with the rod as an associated mass, as if they were a solid body. The work of shear forces in the liquid decreases, and the damping is lowered.

The sound velocity (curve *1*), which was calculated from Eqs. (12)–(14) as a function of the viscosity of the liquid, is shown in Fig. 3. The velocity monotonically decreases and attains its limiting value at a large viscosity. Curve *2* characterizes the behavior of the sound velocity for an infinite volume of the liquid. The appearance of a region in which the sound velocity is lower than that in the infinite volume of the liquid seems surprising. However, such a behavior is explained by both the reflection of the generated wave from the free surface of the liquid and interaction between the reflected wave and the strip. This phenomenon is observed in the region of the maximum damping when the thickness of the liquid layer is comparable to the length of the generated transverse wave.

REFERENCES

1. A. K. Rogozinskiĭ, S. L. Bazhenov, and A. A. Berlin, Dokl. Akad. Nauk **362**, 618 (1998) [Dokl. Phys. **43**, 623 (1998)].
2. A. K. Rogozinskiĭ, S. L. Bazhenov, and A. A. Berlin, Dokl. Akad. Nauk **362**, 481 (1998) [Dokl. Phys. **43**, 616 (1998)].
3. M. A. Isakovich, *General Acoustics* (Nauka, Moscow, 1973).
4. V. A. Krasil'nikov and V. V. Krylov, *Introduction to Physical Acoustics* (Nauka, Moscow, 1984).
5. L. F. Lependin, *Acoustics* (Vysshaya Shkola, Moscow, 1978).
6. L. D. Landau and E. M. Lifshitz, *Course of Theoretical Physics*, Vol. 6: *Fluid Mechanics* (Nauka, Moscow, 1988; Pergamon, New York, 1987).
7. L. D. Landau and E. M. Lifshitz, *Course of Theoretical Physics*, Vol. 7: *Theory of Elasticity* (Nauka, Moscow, 1965; Pergamon Press, New York, 1986).
8. H. B. Dwight, *Tables of Integrals and Other Mathematical Data* (Macmillan, London, 1961; Nauka, Moscow, 1973).
9. G. N. Watson, *Treatise on the Theory of Bessel Functions* (Cambridge Univ. Press, Cambridge, 1952; Inostrannaya Literatura, Moscow, 1949).
10. B. W. Rosen, in *Fiber Composite Materials* (ASM, Metals Park, 1965), pp. 37–76.

Translated by Yu. Vishnyakov

Doklady Physics, Vol. 46, No. 6, 2001, pp. 418–421. Translated from Doklady Akademii Nauk, Vol. 378, No. 5, 2001, pp. 624–627.

TECHNICAL PHYSICS

Propagation of Longitudinal Acoustic Waves in a Thin Cylindrical Pipe Filled with a Liquid

S. L. Bazhenov*, A. K. Rogozinskiĭ,**
and Corresponding Member of the RAS A. A. Berlin**

Received December 21, 2000

The velocity of a longitudinal acoustic wave in an elastic material is specified by its elasticity modulus E and density ρ [1]:

$$c = \sqrt{\frac{E}{\rho}}. \quad (1)$$

In [2, 3], the effect of reducing the wave velocity was found for elastic rods made in the form of a thin strip or fiber and immersed in a liquid. A reduction of the velocity is observed only in thin samples with a thickness on the order of a hundred microns. The effect found is caused by the fact that the so-called boundary layer of a liquid vibrates together with the rod. The thickness of this layer depends on the vibration frequency and the density and viscosity of the liquid. When the sound velocity depends on the viscosity, the effect discovered is employed for the determination of the viscosity of liquids. An advantage of this method is its ability to provide high-rate measurements, which makes it possible to control the chemical reactions with a time-dependent viscosity that proceed in liquids. As a sensor, we used metallic strips and fibers with a diameter of approximately 0.1 mm [2, 3], which were immersed in the liquid under investigation. The use, for this purpose, of a thin capillary filled with the liquid presents a number of advantages, among them the possibility of operating with a very small quantity (specified by the capillary volume) of liquid. The problem of the effect of liquid on the propagation of sound in a thin pipe (capillary) has not yet been solved. The goal of this study is to theoretically seek a solution to this problem.

We consider the propagation of a longitudinal acoustic wave in an elastic capillary filled with a viscous liquid (Fig. 1). The presence of the liquid is taken into account by adding a term describing the interaction of the fiber with the liquid into the vibrational equation [2, 3]:

$$S\rho_0\frac{\partial^2 u}{\partial t^2} = SE\frac{\partial^2 u}{\partial y^2} + 2\pi R\tau. \quad (2)$$

Here, u is the displacement of a capillary element from the equilibrium position; Y is the direction of the capillary axis; ρ_0 and E are the density and the modulus of elasticity for the capillary material, respectively; $S = \pi(R_1^2 - R^2)$ is the capillary cross section; R and R_1 are the inner and outer radii of the capillary, respectively; and τ is the shear stress arising as a result of capillary interaction with the liquid.

For finding the shear stress τ, we solve the problem of motion of a liquid in the capillary. We consider an

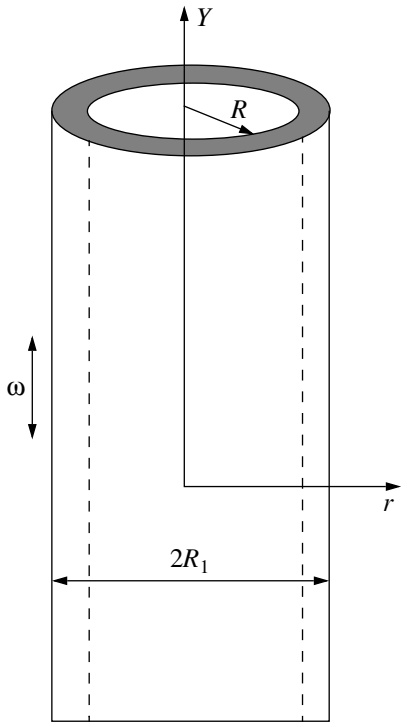

Fig. 1. Scheme of calculations.

* *Institute of Synthetic Polymeric Materials, Russian Academy of Sciences, Profsoyuznaya ul. 70, Moscow, 117393 Russia*

** *Semenov Institute of Chemical Physics, Russian Academy of Sciences, ul. Kosygina 4, Moscow, 117977 Russia*

1028-3358/01/4606-0418$21.00

unbounded cylindrical capillary with an inner radius R in contact with an incompressible viscous liquid. The capillary executes longitudinal harmonic vibrations along its Y-axis. In the cylindrical coordinates, the motion of the liquid is described by the equation [4–6]

$$\rho\frac{\partial v}{\partial t} = \eta\left(\frac{\partial^2 v}{\partial r^2} + \frac{1}{r}\frac{\partial v}{\partial r}\right), \quad (3)$$

where v is the velocity of liquid along the Y-axis of vibrations, ρ is the density, and η is the viscosity of the liquid.

We seek the time-periodic solution to Eq. (3) in the form

$$v(r, t) = s(r)\exp(i\omega t),$$

where ω is the angular frequency of vibrations. By changing the variable $r = \sqrt{\frac{i\eta}{\omega\rho}}z$, we reduce relationship (3) to the form

$$\frac{d^2 s}{dz^2} + \frac{1}{z}\frac{ds}{dz} + s = 0. \quad (4)$$

Equation (4) represents the Bessel equation of the complex argument $z = xi\sqrt{i}$, where $x = -r\sqrt{\frac{\omega\rho}{\eta}}$. Bounded at $x = 0$, the solution to this equation is known as the Bessel function of the first kind of the argument $xi\sqrt{i}$. This function is also termed the Tomson function [7, 8]:

$$s = s_0(\mathrm{ber}x + i\,\mathrm{bei}x), \quad (5)$$

where ber and bei are, respectively, the real and imaginary parts of the Tomson function and s_0 is a constant.

The shear stress with which the liquid acts on the capillary is $\tau = -\eta\frac{dv}{dr}$ for $r = R$. Using the evenness of the Tomson function, i.e., the conservation of its value while changing the sign of its argument, we obtain

$$\tau = -s_0\sqrt{\eta\omega\rho}(\mathrm{ber}'x_0 + i\,\mathrm{bei}'x_0)\exp(i\omega t), \quad (6)$$

where

$$x_0 = \sqrt{\frac{\omega\rho}{\eta}}R, \quad \mathrm{ber}'x = \frac{d\,\mathrm{ber}x}{dx}, \quad \mathrm{bei}'x = \frac{d\,\mathrm{bei}x}{dx}.$$

The solution to Eq. (2) is sought in the form

$$u = u_0\exp[i(\omega t - ky)],$$

where k is the wave number. The velocity of the capillary is found as $\frac{\partial u}{\partial t}$:

$$v = i\omega u_0\exp[i(\omega t - ky)]. \quad (7)$$

The velocity of liquid $s_0(\mathrm{ber}x_0 + i\,\mathrm{bei}x_0)\exp(i\omega t)$ at the capillary boundary is equal to v:

$$i\omega u_0 = s_0(\mathrm{ber}x_0 + i\,\mathrm{bei}x_0), \quad (8)$$

where $x_0 = -R\sqrt{\frac{\omega\rho}{\eta}}$. Substituting relationships (6) and (8) into Eq. (2), we obtain

$$S\rho_0\omega^2 = SEk^2 + i\frac{2\pi R\omega\sqrt{\eta\omega\rho}(\mathrm{ber}'x_0 + i\,\mathrm{bei}'x_0)}{\mathrm{ber}x_0 + i\,\mathrm{bei}x_0}. \quad (9)$$

Taking into account formula (1), which relates the elasticity modulus to the sound velocity, we determine the wave number as

$$k = \frac{\omega}{c_0}\sqrt{1 + \alpha - i\beta}. \quad (10)$$

Here, c_0 is the sound velocity in the capillary without a liquid,

$$\alpha = \frac{2R}{R_1^2 - R^2}\sqrt{\frac{\rho\eta}{\omega\rho_0^2}}\frac{\mathrm{bei}'x_0\,\mathrm{ber}x_0 - \mathrm{ber}'x_0\,\mathrm{bei}x_0}{\mathrm{ber}^2x_0 + \mathrm{bei}^2x_0},$$
$$\beta = -\frac{2R}{R_1^2 - R^2}\sqrt{\frac{\rho\eta}{\omega\rho_0^2}}\frac{\mathrm{ber}'x_0\,\mathrm{ber}x_0 + \mathrm{bei}'x_0\,\mathrm{bei}x_0}{\mathrm{ber}^2x_0 + \mathrm{bei}^2x_0}. \quad (11)$$

The sound velocity can be found as a ratio of the angular frequency to the wave-number modulus:

$$c = \frac{c_0}{\sqrt[4]{(1 + \alpha)^2 + \beta^2}}. \quad (12)$$

The damping of a longitudinal wave is determined by the imaginary part of the wave number k. Assuming the damping to be weak ($\beta \ll 1$), we expand relationship (10) into a series in order to find the wave amplitude:

$$u = u_0\exp\left(-\frac{\omega\beta y}{2c_0}\right). \quad (13)$$

In the asymptotic limits of a small and ultimately large capillary inner radius, solution (10) is simplified.

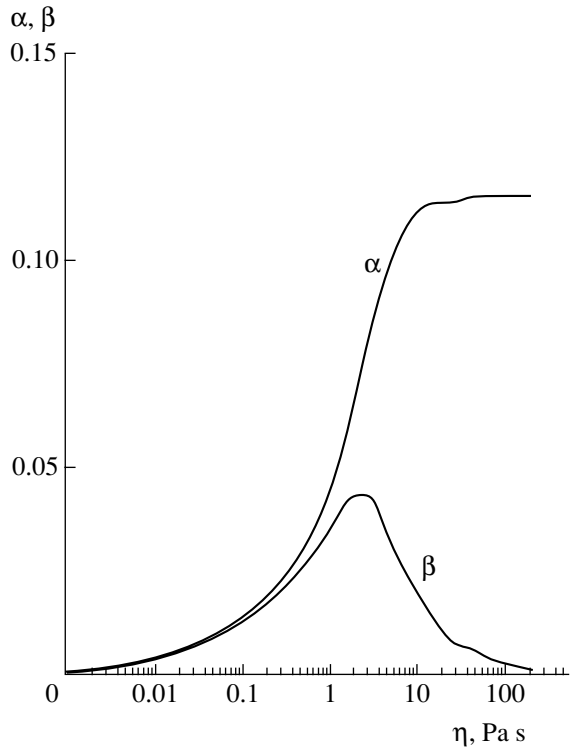

Fig. 2. Coefficients α and β as functions of the viscosity η of a liquid. The calculation was carried out for a capillary with inner and outer diameters of 100 and 200 μm, respectively. Densities of the liquid and the capillary material were 900 and 2600 kg/m^3, respectively. The sound velocity measured in the absence of the liquid was 5.1 km/s.

In the asymptotic case $x \gg 1$, the functions ber$x$ and bei$x$ take the form [7, 8]

$$\mathrm{ber}x \approx \frac{\exp\left(\frac{x}{\sqrt{2}}\right)}{\sqrt{2\pi x}}\cos\left(\frac{x}{\sqrt{2}} - \frac{\pi}{8}\right),$$

$$\mathrm{ber}'x \approx \frac{\exp\left(\frac{x}{\sqrt{2}}\right)}{\sqrt{2\pi x}}\cos\left(\frac{x}{\sqrt{2}} + \frac{\pi}{8}\right),$$

$$\mathrm{bei}x \approx \frac{\exp\left(\frac{x}{\sqrt{2}}\right)}{\sqrt{2\pi x}}\sin\left(\frac{x}{\sqrt{2}} - \frac{\pi}{8}\right),$$

$$\mathrm{bei}'x \approx \frac{\exp\left(\frac{x}{\sqrt{2}}\right)}{\sqrt{2\pi x}}\sin\left(\frac{x}{\sqrt{2}} + \frac{\pi}{8}\right).$$

Using these relationships, we obtain

$$\alpha = \beta = \frac{R}{R_1^2 - R^2}\sqrt{\frac{2\rho\eta}{\omega\rho_0^2}}.$$

The sound velocity is expressed by the relationship

$$c = c_0\left(1 - \frac{R}{R_1^2 - R^2}\sqrt{\frac{\rho\eta}{2\omega\rho_0^2}}\right). \quad (14)$$

The viscosity of a liquid is specified by the formula

$$\eta = \frac{2\omega\rho_0^2(c_0^2 - c)^2(R_1^2 - R^2)^2}{\rho c_0^2 R^2}. \quad (15)$$

In the asymptotic limit of $x \ll 1$, the length of the transverse wave greatly exceeds the capillary diameter. Expanding the functions ber$x$ and bei$x$ into a series for $x \ll 1$ [7, 8] and restricting ourselves to first terms of the expansion, namely, $\mathrm{ber}x = 1 - \frac{x^4}{64}$, $\mathrm{ber}'x = -\frac{x^3}{16}$, $\mathrm{bei}x = \frac{x^2}{4}$, and $\mathrm{bei}'x = \frac{x}{2} - \frac{x^5}{384}$, we determine the coefficients α and β as

$$\alpha = \frac{m}{M}\left(1 - \frac{\omega^2\rho^2}{48\eta^2}R^4\right), \quad \beta = \frac{\omega\rho R^2}{8\eta}\frac{m}{M}. \quad (16)$$

Here, $m = \pi R^2\rho L$ is the mass of the liquid in the capillary and L and $M = \pi(R_1^2 - R^2)\rho_0 L$ are the capillary length and mass, respectively.

Ignoring the minuend in Eq. (16), we obtain $\alpha = \frac{m}{M}$. The sense of this relationship consists in the fact that, at a small capillary thickness, the whole liquid vibrates as an associated mass together with the capillary material. In this case, the wave-propagation velocity is specified only by the masses of both the liquid and capillary and is independent of the viscosity of the liquid:

$$c = c_0\sqrt{\frac{M}{M + m}}. \quad (17)$$

Solving Eq. (16) with respect to the viscosity η and considering the damping to be small, we obtain

$$\eta = \sqrt{\frac{Q}{1 + \frac{2m}{M} - \frac{c_0^4}{c^4}}}, \quad (18)$$

where

$$Q = \frac{\omega^2\rho^2R^4m}{M}\left(\frac{1}{24} + \frac{m}{64M}\right).$$

The viscosity of the liquid can also be determined from the signal damping:

$$\eta = \frac{\omega\rho R^2}{8\beta}\frac{m}{M}.$$

In theoretical evaluation of the coefficients α and β, it is more convenient to calculate the functions ber$x$ and

bei$x$ not in the form of a series (poorly convergent at large x) but using numerical integration:

$$\mathrm{ber}_n x = \frac{1}{2\pi}\int_0^{2\pi} \cosh\left(\frac{x\sin\theta}{\sqrt{2}}\right)\cos\left(n\theta + \frac{x\sin\theta}{\sqrt{2}}\right)d\theta, \quad (19)$$

$$\mathrm{bei}_n x = \frac{1}{2\pi}\int_0^{2\pi} \sinh\left(\frac{x\sin\theta}{\sqrt{2}}\right)\sin\left(n\theta + \frac{x\sin\theta}{\sqrt{2}}\right)d\theta, \quad (20)$$

where $\mathrm{ber}_0 x \equiv \mathrm{ber}x$ and $\mathrm{bei}_0 x \equiv \mathrm{bei}x$.

Relationships (19) and (20) are derived from the Bessel integral

$$J_n(x) = \frac{1}{2\pi}\int_0^{2\pi} \cos(n\theta - z\sin\theta)d\theta, \quad (21)$$

where n = 0, 1, 2, 3, … is the subscript of the Bessel function. The argument z of the Tomson function is a complex quantity. It is possible to pass to the real-valued argument using the relationship

$$\cos z = \frac{e^{iz} - e^{-iz}}{2}.$$

The derivatives of the functions ber$x$ and bei$x$ were determined using recursion formulas:

$$\mathrm{ber}'x = \frac{\mathrm{ber}_1 x + \mathrm{bei}_1 x}{\sqrt{2}}, \quad \mathrm{bei}'x = \frac{\mathrm{bei}_1 x - \mathrm{ber}_1 x}{\sqrt{2}}.$$

In Fig. 2, we show the coefficients α and β calculated from Eq. (11) as functions of the viscosity of the liquid. The coefficient α monotonically increases and attains its limit at a high viscosity. The coefficient β attains its maximum at a certain viscosity of the liquid. Low damping at a low viscosity of the liquid is explained by the small length of the transverse wave and, consequently, by the low associated mass of the liquid. Reduction in the damping at a high viscosity is explained by the fact that the whole liquid vibrates with the rod as an associated mass. As a consequence, the energy loss decreases and the signal damping is reduced.

In Fig. 3, we present the sound velocity, which was calculated from Eqs. (12)–(14), as a function of the viscosity of the liquid. The velocity monotonically decreases and attains its limit. The lower limit of the velocity at a high viscosity is determined by the fact that the whole liquid participates in the vibrations as an associated mass.

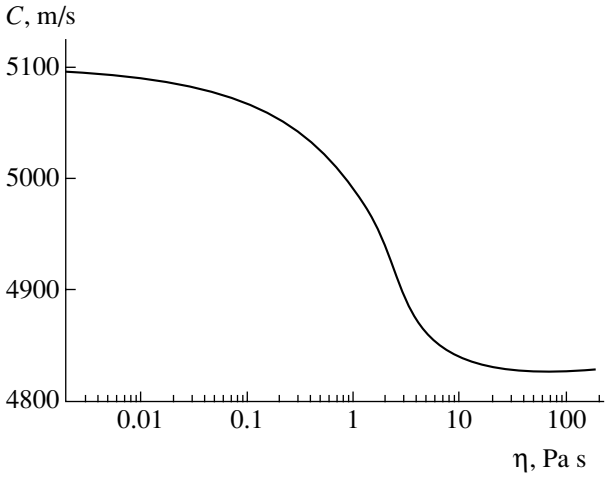

Fig. 3. Sound velocity as a function of the viscosity of a liquid.

REFERENCES

1. L. D. Landau and E. M. Lifshitz, *Course of Theoretical Physics*, Vol. 7: *Theory of Elasticity* (Nauka, Moscow, 1965; Pergamon Press, New York, 1986).
2. A. K. Rogozinskiĭ, S. L. Bazhenov, and A. A. Berlin, Dokl. Akad. Nauk **362**, 618 (1998) [Dokl. Phys. **43**, 623 (1998)].
3. A. K. Rogozinskiĭ, S. L. Bazhenov, and A. A. Berlin, Dokl. Akad. Nauk **362**, 481 (1998) [Dokl. Phys. **43**, 616 (1998)].
4. L. D. Landau and E. M. Lifshitz, *Course of Theoretical Physics*, Vol. 6: *Fluid Mechanics* (Nauka, Moscow, 1988; Pergamon, New York, 1987).
5. V. A. Krasil'nikov and V. V. Krylov, *An Introduction to Physical Acoustics* (Nauka, Moscow, 1984).
6. L. F. Lependin, *Acoustics* (Vysshaya Shkola, Moscow, 1978).
7. H. B. Dwight, *Tables of Integrals and Other Mathematical Data* (Macmillan, London, 1961; Nauka, Moscow, 1973).
8. G. N. Watson, *Treatise on the Theory of Bessel Functions* (Cambridge Univ. Press, Cambridge, 1952; Inostrannaya Literatura, Moscow, 1949).

Translated by V. Bukhanov

Doklady Physics, Vol. 46, No. 6, 2001, pp. 422–424. Translated from Doklady Akademii Nauk, Vol. 378, No. 4, 2001, pp. 483–486.

MECHANICS

Multisolitons in a Liquid with Gas Bubbles of Two Different Sizes

Academician V. E. Nakoryakov and V. E. Dontsov

Received January 9, 2001

The evolution of pressure waves in a liquid with one-sized bubbles has been reasonably well studied both theoretically and experimentally and described, for example, in monographs [1, 2]. In particular, it was shown that an initial perturbation in a gas–liquid medium can disintegrate into solitary waves (solitons), and their properties were studied in considerable detail. In [3, 4], it was shown that taking into account the polydisperse nature of a gas–liquid medium leads to an additional damping of pressure perturbations without qualitatively modifying the wave structure. In [5], the existence of oscillatory solitary waves (multisolitons) in a liquid with gas bubbles of two different sizes was discovered. Numerical calculations [6, 7] showed that, in the case of a propagation of nonlinear perturbations in a liquid with gas bubbles of two different sizes, the existence of two degrees of freedom results in the formation of complicated wave structures (multisolitons). The simplest structures are multisolitons with a (2, 1) oscillation mode. The oscillation mode is understood as the number of oscillations of small-sized (m) and large-sized (n) bubbles in an oscillatory solitary wave. Steady multisolitons with a discrete amplitude spectrum, as well as quasisteady multisolitons with a continuous amplitude spectrum, were numerically investigated in [6, 7]. In [8], the structure and damping of oscillatory solitary waves were experimentally investigated in a liquid containing gas bubbles with bubble-radius ratios of $\frac{R_2}{R_1} = 2$ and $\frac{R_2}{R_1} = 3$. The slow-motion filming of gas bubbles in a wave confirmed the resonant nature of multisoliton formation.

In this study, we investigated experimentally the evolution and structure of solitary waves in a liquid containing gas bubbles of two different sizes, with the radius ratios $\frac{R_2}{R_1} = 1.5$ and $\frac{R_2}{R_1} = 1.7$. The existence of new types of oscillatory solitary waves caused by resonant oscillations of bubbles has been shown.

Kutateladze Institute of Thermal Physics, Siberian Division, Russian Academy of Sciences,
pr. Akademika Lavrent'eva 1, Novosibirsk, 630090 Russia

The experiments were carried out using a "shock-tube" type setup. Its operational part represented a vertical thick-wall steel pipe with an inner diameter of 0.053 m and a length of 1.5 m. This pipe was filled by a liquid and saturated by gas bubbles produced by two independent bubble generators arranged in the lower part of the pipe. The spread of bubble sizes in a liquid was within the range of ±5%. The bulk gas content in a liquid was less than 1%. We used a 50% solution of glycerin in distilled water as a working liquid and Freon 12 as a gas phase. Bell-shaped pressure waves were generated by an electromagnetic radiator arranged on the bottom of the operational part of the setup. The signal formed when a thin copper plate was pushed away from an electromagnetic coil in the passing of a current pulse through the coil. Pressure-wave profiles were detected by piezoelectric pressure sensors arranged lengthwise to the operational part of the apparatus. The signals from sensors were fed into an analog-to-digital converter and then processed by a computer.

It is experimentally shown that such media are characterized by an instability of appearance and evolution of complicated wave structures (multisolitons). From an initial signal, either ordinary solitary waves or multisolitons breaking up into ordinary solitary waves in the process of evolution can be isolated. Figure 1 illustrates the evolution of pressure waves in a liquid with gas bubbles of two different sizes, with the bubble-radius ratio $\frac{R_2}{R_1} = 1.5$. It is seen that an oscillatory solitary wave with the (3, 2) oscillation mode (according to the terminology accepted in [6]) is separated from an initial bell-shaped signal at a distance of $x = 0.56$ m from the input into the gas–liquid medium. In the time required for such a wave to propagate through the medium, a large-sized bubble makes two oscillations in the wave; the small-sized bubble, three oscillations. Unlike the multisolitons with the (2, 1) oscillation mode present in a liquid with gas bubbles with $\frac{R_2}{R_1} = 2$ [8], which are stable and do not qualitatively change shape in the process of evolution, in our experiments, the (3, 2) solitary wave is unstable and breaks up into ordinary solitary waves (Fig. 1; $x = 0.76$ m). The profile

1028-3358/01/4606-0422$21.00

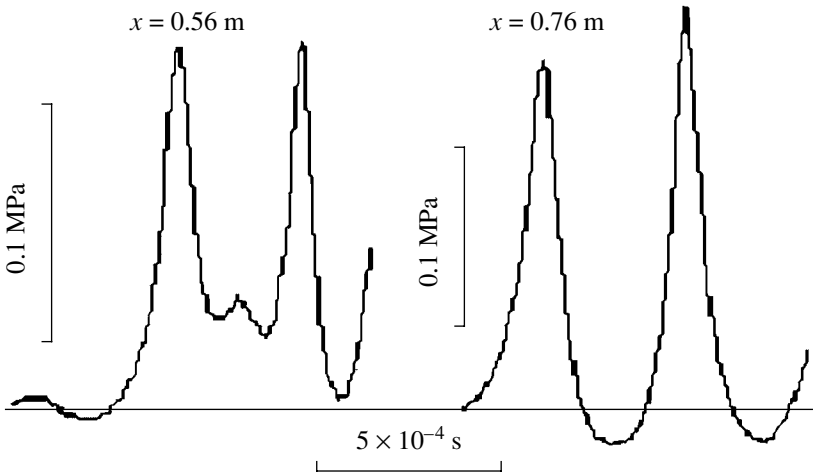

Fig. 1. Structure of a multisoliton with the (3, 2) oscillation mode. $R_1 = 0.53$ mm.

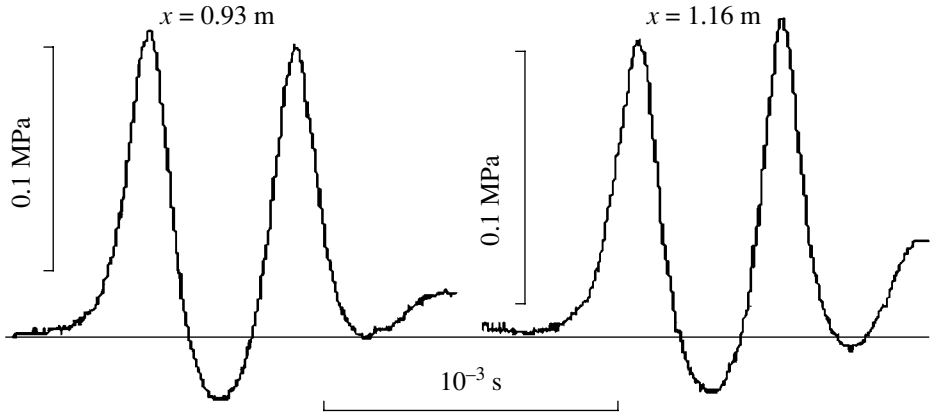

Fig. 2. Structure of a multisoliton with the (2, 2) oscillation mode. $R_1 = 0.53$ mm, $\frac{R_2}{R_1} = 1.5$.

of an ordinary solitary wave is well described by the calculation for a monodisperse medium with the averaged radius value proposed in [4]. The quasistable (3, 2) multisolitons in a liquid containing gas bubbles with the radius ratio $\frac{R_2}{R_1} = 1.5$ were previously discovered numerically in [7]. However, the predicted multisolitons are stable, as opposed to the experimentally observed multisolitons, and do not break up in the process of evolution. The cause of instability of such multisolitons may be the difference in the experimental bubble-radius ratio from the calculated ratio, an insufficiently narrow size distribution of bubbles, and heterogeneity of the gas–liquid mixture. To clarify the reasons for this instability, it is necessary to carry out numerical calculations with allowance for real experimental conditions.

A specific feature of quasistable solitary waves in a liquid with gas bubbles of different sizes is their possible interaction [7]. This phenomenon can lead to the formation of new wave structures. The simplest structure is a numerically calculated (2, 2) mode formed via the interaction of two ordinary solitary waves with closely related amplitudes [7]. The calculated (2, 2) mode is stable and varies only slightly in its shape in the process of propagation. In our experiments, we also discovered the interaction of solitary waves in a liquid with gas bubbles of two different sizes and the formation of a new wave structure (Fig. 2). From an initial signal, two solitary waves are isolated, the interaction of which led to the equalization of their amplitudes and to the formation of a new quasistable wave structure. In the process of evolution, the wave amplitude decreases via dissipative losses, but the wave structure is retained (Fig. 2). Note that, in experiments, contrary to in calculations, the solitary waves are coupled through a rarefaction wave. The presence of bubbles of two different sizes in a liquid leads to the appearance of a rarefaction zone with a sufficiently large wave amplitude (up to 20% of the solitary-wave amplitude). The calculations performed in [4] showed that, in a polydisperse

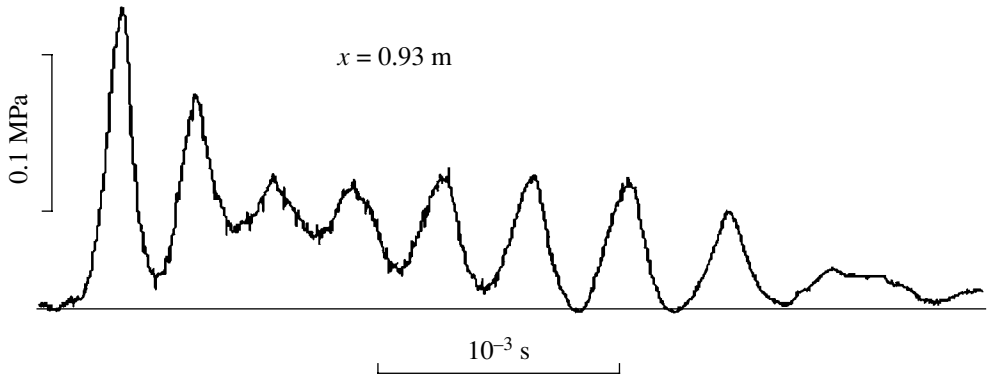

Fig. 3. Structure of a pressure wave with a moderate amplitude. $R_1 = 0.53$ mm, $\frac{R_2}{R_1} = 1.5$.

medium, small-sized bubbles can "follow" the pressure of a liquid in the wave, while large-sized bubbles cannot. The delay in the expansion of large-sized bubbles at the rear front of the first solitary wave and the essential nonlinearity of the medium are likely to lead to the formation of the rarefaction zone. Similar wave structures were found in a liquid with gas bubbles of two different sizes, with $\frac{R_2}{R_1} = 1.7$, and their behavior corresponds qualitatively to the wave structures shown in Fig. 2.

As the amplitude of the signal entering the medium increases, the process of formation and separation of solitary waves is delayed. Within the interval of measurement, the solitary waves remain coupled or form an oscillatory shock wave (Fig. 3). An interesting feature of the structure of coupled solitary waves is the nonmonotone behavior of the solitary-wave envelope, which differs from that obtained in the previous theoretical analysis and numerical calculations [1, 2]. The appearance of an analogue of "beats" is presumably associated with the transformation of solitary waves. This means that, in the process of propagation of solitary waves, a phase shift takes place between pressure oscillations in the wave and bubble-radius oscillations owing to the divergence of these waves, which can initiate the beats.

No formation of chaotic structures in a liquid with gas bubbles of two different sizes, with $\frac{R_2}{R_1} = 1.7$, which was predicted in [7], was observed experimentally.

Thus, new types of wave structures (multisolitons) are experimentally found in a liquid with gas bubbles of two different sizes, with the bubble-radius ratios $\frac{R_2}{R_1} = 1.5$ and $\frac{R_2}{R_1} = 1.7$. The multisolitons with the (3, 2) oscillation mode are shown to be unstable and to disintegrate into ordinary solitary waves. The multisolitons with the (2, 2) oscillation mode are stable and damp in the process of evolution owing to dissipative losses but qualitatively retain their shape. During the propagation of a series of solitary (oscillatory shock) waves, a nonmonotone behavior is observed for the solitary-wave envelope; this can be associated with a phase shift between the pressure oscillation in the wave and the bubble-radius oscillations in the process of evolution of these waves.

ACKNOWLEDGMENTS

This work was supported by the Russian Foundation for Basic Research, project nos. 00-01-00831 and 00-15-96177.

REFERENCES

1. V. E. Nakoryakov, B. G. Pokusaev, and I. R. Shreĭber, *Wave Dynamics of Gas–Liquid and Vapor–Liquid Media* (Énergoatomizdat, Moscow, 1990).
2. R. I. Nigmatulin, *Dynamics of Multiphase Media* (Nauka, Moscow, 1987), Vol. 2.
3. V. K. Kedrinskiĭ, Zh. Prikl. Mekh. Tekh. Fiz., No. 4, 29 (1968).
4. V. Sh. Shagapov, Izv. Akad. Nauk SSSR, Mekh. Zhidk. Gaza, No. 6, 145 (1976).
5. V. G. Gasenko, V. E. Dontsov, V. V. Kuznetsov, and V. E. Nakoryakov, Izv. Sib. Otd. Akad. Nauk SSSR, Ser. Tekh. Nauk **6** (21), 43 (1987).
6. V. G. Gasenko and V. P. Izergin, in *Proceedings of the XI International Symposium on Nonlinear Acoustics, Novosibirsk, 1987*, Part 2, p. 23.
7. V. P. Izergin, Izv. Sib. Otd. Akad. Nauk SSSR, Ser. Tekh. Nauk, No. 1, 16 (1989).
8. V. E. Dontsov, V. E. Kuznetsov, P. G. Markov, and V. E. Nakoryakov, Akust. Zh. **35**, 157 (1989) [Sov. Phys. Acoust. **35**, 95 (1989)].

Translated by V. Bukhanov

Doklady Physics, Vol. 46, No. 6, 2001, pp. 425–428. Translated from Doklady Akademii Nauk, Vol. 378, No. 4, 2001, pp. 487–491.

MECHANICS

An Effect of a Lift Force on the Structure of Attached Internal Waves in a Continuously Stratified Fluid

Yu. D. Chashechkin and V. V. Mitkin

Presented by Academician D.M. Klimov December 15, 2000

Received December 14, 2000

The pattern of attached internal waves [1] as an analogue of lee waves in the atmosphere [2] and ocean [3], as calculated by the source–sink method [4], agrees satisfactorily with observations and laboratory measurements on waves past perfectly shaped obstacles [5] when the wake effect can be ignored. The wave field around a symmetric body dipped into a continuously stratified fluid is antisymmetric about the horizontal plane passing through the line of motion of the body center. In some flow regimes with waves interacting actively with vortices in the wake, the antisymmetric wave pattern evolves into a symmetric one at a large distance from the obstacle [6]. In a real situation, the obstacles are generally irregular in shape and, therefore, a skew in the flow can affect the field structure of radiated waves. This work is devoted to the experimental study of the internal waves generated by a vertical or inclined plate towed uniformly when not only a drag force but also a lifting force arises.

Experiments were made with a setup including a tank measuring $220 \times 40 \times 60$ cm^3, a system creating a saline stratification, a mechanism for the model towing, a carriage intended for the mounting and translating of sensors, a device for acquisition and processing of experimental data, and a schlieren. Linear stratification in the tank is created by the continuous replacement method. The density profile and the velocity distribution are determined with the help of a vertical marker acting as the wake past a freely falling sugar crystal [7]. The layer displacements and the medium buoyancy period T_b (in our experiment, this amounts to 14 s) were measured by a contact "one-electrode" conduction transducer that was calibrated directly in experiments by the "lift–plunge" method. A rectangular plate 2.5 cm wide and 0.1 cm thick was mounted vertically or at some angle to the motion direction and was towed horizontally with a velocity U = 0.08–0.6 cm/s. The plate is fixed on the carriage mounted over the tank by thin transparent knifes.

Institute of Problems of Mechanics,
Russian Academy of Sciences,
pr. Vernadskogo 101, Moscow, 117526 Russia

The flow pattern was observed with the aid of a IAB-458 schlieren equipped with photo-, filming-, and video-systems. Visualization was implemented by two versions of the Maksutov methods, "vertical slit–knife" and "vertical slit–filament at the focus" [8], which are suitable in dealing with media exhibiting wide variations in the gradient of the refraction index. The first method records disturbances of the horizontal component of the refraction index gradient and is preferable, due to its high sensitivity, in cases of weak stratification (or low velocities), when perturbations of the density gradient are small and light rays are not intercepted by the construction elements of the experimental setup.

The second method visualizes the modulus of the perturbation of the refraction-index gradient in a medium. The filament is disposed at the center of the slit image and, as a consequence, the minimum level of the average visual field illumination corresponds to an undisturbed state. In this case, the loci of crests and troughs, as they vary in contrast, are distinguished from the entire wave pattern. This method is more suitable for observing fine structural perturbations that are not shadowed by a contrast image of waves, which is typical of the knife method.

The density label, the vertical marker, is a long-lived hydrodynamic wake past freely falling sugar crystal whose thickness $\delta \sim 0.25$ cm. The time of the wake observation in the shadow picture is 10–150 s, depending on the velocity distribution in the flow. The continuous profile of the horizontal component of velocity is calculated from the measured displacements of the marker over the known time interval Δt.

The key parameters of the problem are the density $\rho(z)$, its vertical gradient $\frac{d\rho}{dz}$, the kinematic fluid viscosity ν, the diffusion coefficient of the stratifying additive κ_s, the free fall acceleration g, the plate height $h = b\sin\alpha$ (α is its slope to the motion direction), and the obstacle velocity U. The exponential stratification is characterized by the scale $\Lambda = \left(\frac{d\ln\rho}{dz}\right)^{-1}$ and by the

1028-3358/01/4606-0425$21.00

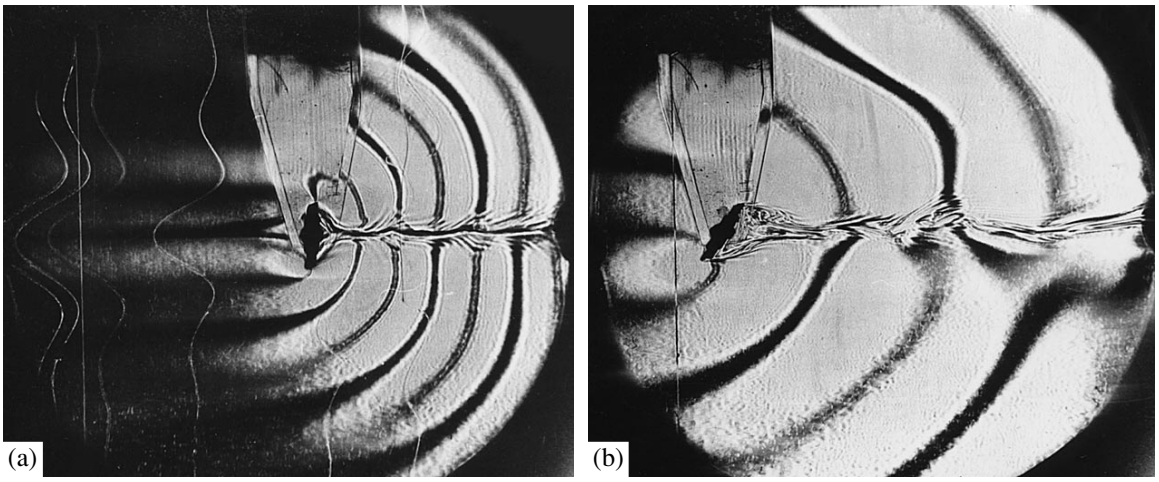

Fig. 1. The antisymmetric wave field near the vertical (a) and inclined (b) plates moving from right to left. T_b = 14 s; (a) U = 0.21 cm/s, $\alpha = 90°$, h = 2.5 cm, l_x = 0.1 cm, λ = 3.0 cm, Re = 52, Fr = 0.19; (b) U = 0.5 cm/s, $\alpha = 53°$, h = 3.0 cm, l_x = 1.5 cm, λ = 7.0 cm, Re = 140, Fr = 0.56. Visualization is implemented by the method of slit–filament at the focus. Dark and gray lines designate crests and troughs of the internal waves, respectively. The thin straight line in the left part of the frames designates the vertical. The curved lines (a) are markers visualizing the velocity profiles in leading and lagging perturbations.

depth-independent buoyancy frequency $N = \sqrt{\frac{g}{\Lambda}}$ $\left(\text{or the buoyancy period } T_b = \frac{2\pi}{N}\right)$.

The structure-forming elements of the flow are the attached internal waves with wavelength $\lambda = UT_b$ [1, 2], velocity $\left(\text{scale } \delta_u = \frac{\nu}{U}\right)$ and density $\left(\text{scale } \delta_\rho = \frac{\kappa_s}{U}\right)$ boundary layers on the obstacle, and diffusion-induced flows with variability scales $\delta_\nu = \sqrt{\frac{\nu}{N}}$ and $\delta_s = \sqrt{\frac{\kappa_s}{N}}$ for the velocity and density, respectively [9]. Basic dimensionless parameters are defined as the ratios of intrinsic scales of the characteristic structural elements: the Reynolds number $\mathrm{Re} = \frac{Uh}{\nu} = \frac{h}{\delta_u}$, the inner vortex Froude number $\mathrm{Fr} = \frac{U}{Nh} = \frac{\lambda}{2\pi h}$, and the ratio between scales $C = \frac{\Lambda}{h}$. The Schmidt number $\mathrm{Sc} = \frac{\nu}{\kappa_s} = \frac{\delta_u}{\delta_\rho} \approx 700$ was unchanged in all the experiments.

Figure 1 depicts the typical flow with the antisymmetric field of attached inner waves past the obstacle (the flow visualization is implemented by the method of slit–filament at the focus; crests and troughs correspond, respectively, to dark and gray lines). Such a field structure is characteristic of a vertical plate or other symmetric obstacles whose perturbing effect is accounted for by fluid displacement and viscous friction force and is observed at an arbitrary value of the inner vortex Froude number [1, 5, 6]. It follows from the theory that the crest and trough loci are arcs of a circle [1]. The shape of the phase surfaces deviates, owing to the Doppler effect, from the calculated shape only in the vicinity of the outer boundary of the density wake, where they are entrained by the wake flow. A symmetric vortex adjoins the plate in the bottom region, and its outer high-gradient envelope evolves into the central high-gradient interlayer shown by the dark line past the body (Fig. 1a).

The interlayer occurrence in the lagging layer is accounted for by the general stratification rearrangement due to the moving obstacle. The density jump lying in the central plane is formed as a result of the blocking effect: the slowing down and pushing through of the fluid in front of the two-dimensional obstacle under the action of buoyancy and viscosity forces and the closing up of fluid layers past the plate, which vary in density and were previously spaced along the vertical direction. A similar phenomenon is observed in the flow past two- and three-dimensional obstacles. The effect of blocking a cylinder upstream was studied in detail in [10].

The system of high-gradient interlayers disposed in a layer varying in thickness (its average height is 1 cm) makes up the outer part of the density wake past the plate. In this flow regime, interlayers with a typical thickness of 0.1 cm do not form a single high-gradient wake envelope; their shape reflects the spatial field structure of the attached waves. The height of the fine-structure wake varies periodically with the distance from the obstacle and reaches, in the upper half-space, a maximum on the crests and a minimum on the troughs of the attached waves (in the lower half-space, the height maxima lie at troughs of the waves). Thus, in this flow regime, the wavelength of the attached wave deter-

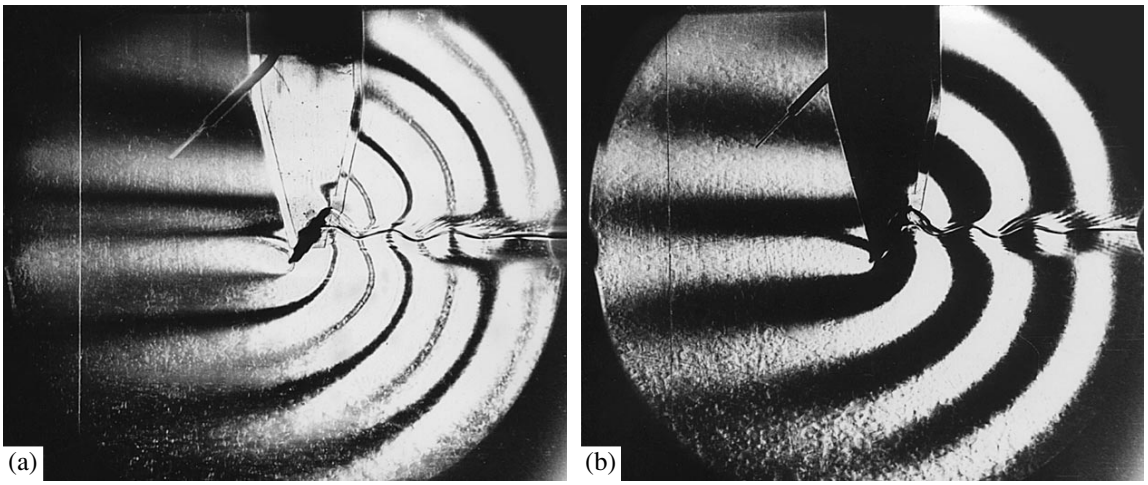

Fig. 2. The symmetric field of the attached internal waves downstream of the inclined plate moving from right to left. T_b = 14 s; U = 0.21 cm/s; $\alpha = 53°$; h = 2.0 cm; l_x = 1.5 cm; λ = 3.0 cm; Re = 42; Fr = 0.23. The flow visualization is implemented by the slit–filament (a) and slit–knife method (b). The sensing element of the conduction transducer past which the plate moves is seen in the upper part of the frame.

mines the scale of the streamwise modulation of the density wake past the plate, which agrees qualitatively with the downstream flow pattern of a horizontal cylinder in the regime of vortex bubbles [11].

In the case of the motion of an inclined plate which is acted upon not only by a drag force but also by a lift force, the general structure and elements of the flow persist; however, the wave system observed in the upper half-space is shifted, as a unit, relative to the system of the internal waves observed in the lower half-space (Fig. 2). Experiments conducted in a wide velocity range show that in the case of a slightly developed bottom vortex, the plate edges serve as active centers of the wave generation. If the vertical size of the bottom vortex exceeds the obstacle height, the wave generation centers are situated in the neighborhood of its upper and lower poles. The high-gradient interlayer separates the wave systems, and its displacement relative to the central horizontal plane depends on the value and direction of the lift force, which, in turn, is determined by the motion velocity and the plate tilt.

High-gradient interlayers formed in the flow stabilize the flow pattern downstream of the obstacle in general and fine details. The two photographs obtained in two independent experiments (Fig. 2) are similar qualitatively and quantitatively. However, the visualization by the filament method (Fig. 2a) shows the density deformation structure on the outer boundary of the density wake more distinctly than the standard visualization (Fig. 2b).

In this instance, when the tilt angle $\alpha = 53°$ (this angle is counted from the horizontal plane passing through the body center and the head edge of the plate), the high-gradient interlayer at the separation point in the wake is displaced upward by 0.4 cm from the plate center. It bends on a scale of Δx = 2.1 cm, which is less than the wavelength of the attached internal wave $\lambda = UT_b$ = 2.9 cm due to the Doppler effect. In this case, the swing of the interlayer oscillations amounts to 0.5 cm and far exceeds its displacements in a flow regime with an antisymmetric field of attached internal waves (Fig. 1a).

The phase shift in the flow regime presented in Fig. 2 is equal strictly to one-half of the wavelength, and the wave field in the vicinity of the obstacle is symmetric about the density wake center. In essence, the displacements of the wave fields (backward in the upper half-space and forward in the lower half-space relative to the body center and to the wave pattern shown in Fig. 1a) are determined, in this case, by the positions of the generation centers, which lie on the body edges and are spaced at $l_x = h\cos\alpha$ = 1.5 cm; in these experiments, this separation is equal to one-half of the wavelength. The stable vortexlike structure that substantially distorts the shape of the phase surfaces is formed in the wake in the vicinity of the third wave. It follows from the deformation character of the wave crests and troughs that the velocity profile of the lee stream is smooth, while the density perturbations are formed by individual interlayers whose thickness $\delta \approx$ 0.05 cm is much smaller than the height of the shift layer.

The antisymmetric pattern of attached internal waves downstream of the inclined plate is restored as the velocity of the plate motion increases (Fig. 1b). In this regime, the density wake is characterized by a well-defined vortex structure. The vorticity comes off the asymmetric bottom vortex in the form of vortex loops whose longitudinal dimension correlates with the wavelength of the internal wave. The crest of the internal wave is in contact with the first peak of the vertical vortex size in the upper half-space, as well as with the

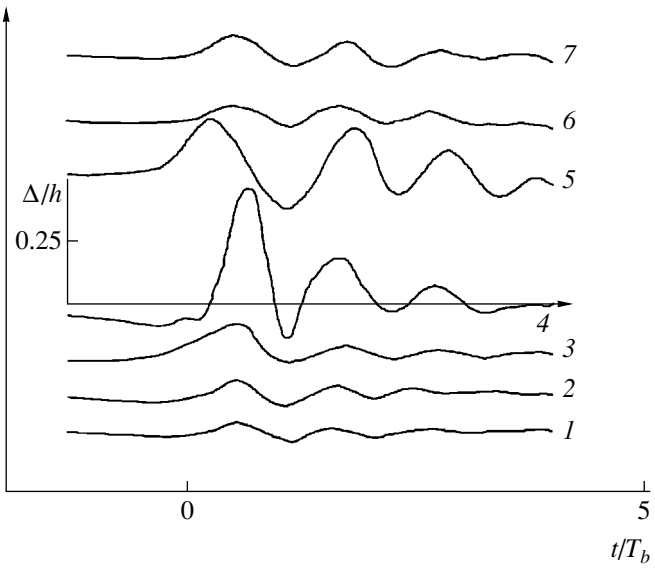

Fig. 3. The time series of displacements of fluid particles in the internal waves generated by a 2-cm high plate mounted at an angle $\alpha = 53°$ to the motion direction. 1–7: Fr = 0.18, 0.19, 0.21, 0.24, 0.28, 0.32, 0.36.

vortex bubble in Fig. 1a. The stratification inhibits the vertical motion rather rapidly, and density inhomogeneities are disposed almost horizontally even in the second wave past the body. Phase surfaces are close to a semicircle almost everywhere with the exception of the region immediately adjoining the wake where they interfere with the second wave (Fig. 2b, right part).

A number of time series presented in Fig. 3 depict the amplitude properties of the wave fields in the vicinity of the inclined plane. A stationary sensor is mounted over the upper edge of the obstacle at a distance of $\Delta z = \frac{UT_b}{2}$ (one-half of the wavelength); the wave amplitude and time are normalized to the obstacle height h and to the buoyancy period, respectively. All the graphs are presented on the same scale; the time origin corresponds to the instant of passing the plate center through the vertical plane in which the sensor is disposed.

All the time series are alike in behavior. A gentle depression (a leading perturbation) corresponds to the onset of perturbations at the given distance; the maximum amplitude, decreasing monotonically with distance from the obstacle, characterizes the wave crest nearest to the obstacle. Nonlinearity in the wave pattern manifests itself in the region of maximum amplitudes ($0.21 < \mathrm{Fr} < 0.32$) as an asymmetry of displacements in crests and troughs and as distortions in the waveform. Comparison between the time series shows that Fr = 0.24 is the necessary condition for the maximum efficiency of the wave generation. The amplitudes of attached waves decrease rather rapidly with a decrease in the Froude number ($\mathrm{Fr} < 0.24$) and with its increase ($\mathrm{Fr} > 0.28$), lasting until the vortex elements of the flow in the wake become additional strong wave sources.

ACKNOWLEDGMENTS

This work was supported by the Ministry of Industry, Science, and Technology of the Russian Federation, project no. MO-9.1(00)-P, by the Ministry of Education of the Russian Federation, Federal Purposeful Project “Integratsiya,” project no. 2.1-304, and by the Russian Foundation for Basic Research, project no. 99-05-64980.

REFERENCES

1. M. J. Lighthill, *Waves in Fluids* (Cambridge Univ. Press, Cambridge, 1978; Mir, Moscow, 1981).
2. R. S. Scorer, *Environmental Aerodynamics* (Halsted Press, New York, 1978; Mir, Moscow, 1980).
3. K. V. Konyaev and K. D. Sabinin, *Waves in Ocean* (Gidrometeoizdat, Leningrad, 1992).
4. Yu. A. Stepanyants, I. V. Sturova, and É. V. Teodorovich, Itogi Nauki Tekh., Mekh. Zhidk. Gaza **21**, 93 (1987).
5. S. A. Makarov and Yu. D. Chashechkin, Izv. Akad. Nauk SSSR, Fiz. Atmos. Okeana **18**, 986 (1982).
6. V. V. Mitkin and Yu. D. Chashechkin, Izv. Akad. Nauk, Mekh. Zhidk. Gaza, No. 5, 139 (1998).
7. S. A. Smirnov, Yu. D. Chashechkin, and Yu. S. Il’inykh, Izmer. Tekh., No. 6, 15 (1998).
8. D. D. Maksutov, *Shadow Methods for Testing Optical Systems* (Gostekhteorizdat, Leningrad, 1934).
9. V. G. Baĭdulov and Yu. D. Chashechkin, Izv. Akad. Nauk, Fiz. Atmos. Okeana **29**, 666 (1993).
10. V. V. Mitkin and Yu. D. Chashechkin, Izv. Akad. Nauk, Mekh. Zhidk. Gaza, No. 5, 20 (2000).
11. D. L. Boyer, P. A. Davies, H. J. S. Fernando, and X. Zhang, Philos. Trans. R. Soc. London, Ser. A **328**, 501 (1989).

Translated by V. Devitsyn

Doklady Physics, Vol. 46, No. 6, 2001, pp. 429–433. Translated from Doklady Akademii Nauk, Vol. 378, No. 5, 2001, pp. 628–632.

MECHANICS

A Hyperbolic Model for Viscous Mixed Flows

B. V. Rogov and I. A. Sokolova

Presented by Academician A.A. Samarskiĭ November 2, 2000

Received November 9, 2000

1. INTRODUCTION

There is a wide class of steady-state viscous gas flows that are important to industrial application in which the disturbance propagation upstream is insignificant. This class includes limited mixed flows, the most part of which are overlapped by a sonic surface. Since small (acoustic) disturbances do not propagate counter to a supersonic flow, the physical conditions at the right-hand boundary situated downstream with respect to the sonic surface weakly affect the mainstream region [1, 2]. For internal flows, such a regime is realized, for example, in a Laval nozzle that represents a component of chemical or gas-dynamic lasers or of rocket or other-type engines [1, 3]. In the case of external flows, this effect occurs in the shock layer being formed by a supersonic flow around blunted bodies [2, 4]. It is unreasonable to use the complete Navier–Stokes equations for numerical simulation of such flows. This is especially true while calculating chemically and thermally nonequilibrium gas-mixture flows at moderate or large values of the Reynolds number [2, 3].

The most efficient models describing these flows are based on systems of parabolic or hyperbolic equations. These equations are evolutionary with respect to the longitudinal coordinate along the dominating flow direction. Therefore, they can be solved by fast space-marching methods for one downstream run [2, 3].

For internal viscous flows in Laval nozzles, such models were proposed in [5–7]. However, models [5, 6] are inadequate for flows with considerable transverse pressure gradients, while the applicability of model [7] is limited by moderate values of the longitudinal duct-wall curvature.

For the problem of a supersonic viscous gas flow around a blunted body, nonelliptic models were proposed in [8, 9]. However, their efficiency depends on the azimuth angle counted off from the frontal stagnation point.

Institute of Mathematical Modeling,
Russian Academy of Sciences,
Miusskaya pl. 4a, Moscow, 125047 Russia

The hyperbolic model [10] proposed recently for internal mixed viscous flows is free of disadvantages intrinsic to models [5–7] and allows pressure fields with considerable transverse pressure gradients to be adequately reproduced. Here, we propose a new gas-dynamic model for external mixed viscous flows. It is based on hyperbolic-type equations and is intended to describe the shock layer being formed by a supersonic flow near a blunted body at large or moderate values of the Reynolds number. In contrast to [8, 9], this model well reproduces distributions of pressure and heat flux along the surface of a body placed into a flow and makes it possible to calculate flows around thin bodies with lengths hundreds of times their diameters. We demonstrate, as an example, the calculation data for a shock layer formed near a sphere and a very long blunted (in the hemispherical-shape) cylinder in contact with a moving viscous fluid. These calculations agree sufficiently well with the corresponding calculations according to the equations of the full viscous shock layer (FVSL) [11] and the Navier–Stokes equations.

2. A FLOW MODEL

We consider a steady-state flow of a viscous heat-conducting perfect gas in a shock layer, which forms near an unyawed either smooth axisymmetric or plane blunted body. According to [2], at moderate or large values of the Reynolds number, the descriptions of flows by the FVSL model [11] and by the Navier–Stokes equations are close to each other. Therefore, as input equations, we use equations which describe the FVSL and are written out in the curvilinear coordinate system (ξ, η). These equations are

$$g\frac{\partial}{\partial\xi}(\rho u) + \frac{\partial}{\partial\eta}(f\rho) + h\rho u = 0, \tag{1}$$

$$g\frac{\partial}{\partial\xi}(\rho u^2) + \bar{r}^{\nu} y_s \frac{\partial p}{\partial\xi} + \frac{\partial}{\partial\eta}\left[f\rho u - \bar{r}^{\nu}\eta y_s' p - \frac{\bar{r}^{\nu} H\mu}{\mathrm{Re}_\infty} \times\left(\frac{1}{y_s}\frac{\partial u}{\partial\eta} - \frac{K_w u}{H}\right)\right] - \frac{\bar{r}^{\nu} K_w y_s \mu}{\mathrm{Re}_\infty}\left(\frac{1}{y_s}\frac{\partial u}{\partial\eta} - \frac{K_w u}{H}\right) + (h + \bar{r}^{\nu} K_w y_s \sin\alpha)\rho u^2 \tag{2}$$

1028-3358/01/4606-0429$21.00

$$+ \bar{r}^{\nu} K_w y_s \rho u v + (2\bar{r}^{\nu} - 1) y_s' p = 0,$$

$$g\frac{\partial}{\partial \xi}(\rho u v) + \frac{\partial}{\partial \eta}(f\rho v + \bar{r}^{\nu} H p) \qquad (3)$$

$$- gK_w \rho u^2 + h\rho u v - q y_s p = 0,$$

$$g\frac{\partial}{\partial \xi}(\rho u T^*) + \frac{\partial}{\partial \eta}\left\{ f\rho T^* - \frac{\bar{r}^{\nu} H \mu}{\mathrm{Re}_\infty}\left[\frac{1}{y_s \mathrm{Pr}}\frac{\partial T}{\partial \eta}\right.\right.$$

$$\left.\left. + u\cos^2\alpha\left(\frac{1}{y_s}\frac{\partial u}{\partial \eta} - \frac{K_w u}{H}\right)\right]\right\} + h\rho u T^* = 0, \qquad (4)$$

$$T^* = T + \frac{u^2\cos^2\alpha + v^2}{2},$$

$$\rho = \frac{\gamma}{\gamma - 1}\frac{p}{T}, \qquad (5)$$

where

$$\xi = \int_0^x \cos\alpha dx, \quad \eta = \frac{y}{y_s}, \quad \bar{r} = \frac{r}{r_w},$$

$$r = r_w + \eta y_s \cos\alpha, \quad r_w = \int_0^x \sin\alpha dx,$$

$$H = 1 + K_w \eta y_s, \quad y_s' = \frac{dy_s}{d\xi},$$

$$f = \bar{r}^{\nu}(Hv - \eta y_s' \cos^2\alpha), \quad g = \bar{r}^{\nu} y_s \cos^2\alpha,$$

$$h = (2\bar{r}^{\nu} - 1) y_s' u \cos\alpha + q y_s \sin\alpha,^2$$

$$q = \frac{\nu H \cos\alpha}{r_w} + \bar{r}^{\nu} K_w.$$

Here, xR_{w0} and yR_{w0} are the natural orthogonal body-attached coordinates; R_{w0} is the blunted-nose radius; r_w and K_w are the contour of a smooth body and its curvature, respectively; α is the angle between a tangent to the surface and the body's axis of symmetry; $uV_\infty\cos\alpha$ and vV_∞ are the velocity components tangent and normal to the surface; $\rho\rho_\infty$, $p\rho_\infty V_\infty^2$, $\frac{TV_\infty^2}{c_p}$, and $\mu\mu_\infty$ are the density, pressure, temperature, and the dynamic viscosity, respectively; y_s is the shock-layer thickness along a surface normal; $\gamma = \frac{c_p}{c_v}$, where c_p and c_v are the specific heats at constant pressure and volume, respectively; Re_∞ is the Reynolds number; Pr is the Prandtl number; and $\nu = 0$ and 1 for the plane and axisymmetric cases, respectively. The subscripts ∞, w, 0, and s label values of quantities in the incident flow, on the body's surface, in the axis of symmetry, and immediately behind the shock wave, respectively.

The derivative of the shock-wave contour which enters into Eqs. (1)–(4) is related to the shock-layer thickness y_s by the geometric expression

$$\frac{dy_s}{d\xi} = \frac{\tan(\beta - \alpha)}{\cos\alpha}H_s, \quad H_s = 1 + K_w y_s, \qquad (6)$$

where β is the angle between a tangent to the shock wave and the body's axis of symmetry.

We obtain an elliptic-hyperbolic model consisting of a system of FVSL equations, which is simplified below in the following manner.

We present the pressure p in the multiplicative form

$$p = p_s(\xi)\varphi(\xi, \eta),$$

where $p_s(\xi)$ satisfies the trivial equation

$$\frac{\partial p_s}{\partial \eta} = 0. \qquad (7)$$

We replace the pressure gradient entering into (2) by the expression

$$\frac{\partial p}{\partial \xi} \approx \varphi\left(\frac{\partial p_s}{\partial \xi}\right) + \omega p_s\left(\frac{\partial \varphi}{\partial \xi}\right), \qquad (8)$$

the weighting function $\omega(\xi, \eta)$ being taken in the form

$$\omega = \min\left\{1, \sigma\frac{\gamma M_x^2}{1 + (\gamma - 1)M_x^2}\right\}, \quad 0 \le \sigma < 1, \qquad (9)$$

where M_x is the local Mach number determined with the use of the longitudinal velocity component u. Then, the density and $\frac{dy_s}{d\xi}$ are excluded from Eqs. (1)–(4) with the help of the equation of state (5) and Eq. (6), respectively.

We now determine the type of system of equations derived. Assuming that, at large values of the Reynolds number the mathematical type of the system of differential equations (1)–(4), (6), (7) with respect to the unknowns u, v, T, φ, p_s, and y_s is determined by inviscid terms [12], we consider the characteristic equation

$$\det(\lambda \mathbf{A} - \mathbf{B}) = 0.$$

Here, $\mathbf{A}$ and $\mathbf{B}$ are the matrices corresponding to the longitudinal and transverse gradients of the desired functions, respectively, and λ are the eigenvalues. With allowance for expressions (8) and (9), the characteristic equation has only real-valued eigenvalues. Therefore, the system of equations under consideration is hyperbolic with respect to the variable ξ throughout the entire range of the Mach numbers [12].

The model corresponding to the system of equations derived is termed the model of the hyperbolic viscous shock layer (HVSL model). It takes into account, as

much as possible, the inviscid disturbance transfer downstream and ignores it upstream. Thus, the elliptic properties of the FVSL system of equations are associated with the term $(1 - \omega)p_s\frac{\partial\varphi}{\partial\xi}$, which represents a part of the pressure gradient in the longitudinal-momentum equation (2).

The boundary conditions for Eqs. (1)–(4) and (7) in the variables u, v, T, φ, and p_s are the following. In the shock wave ($\eta = 1$), they are three of four generalized Rankine–Hugoniot relations [2] and $\varphi = 1$. On the surface ($\eta = 0$), which is in contact with the fluid, they are the given temperature and the conditions of attachment and the absence of injection (these conditions are imposed on the velocity components). The fourth, Rankine–Hugoniot relation between the angle β and p_s serves, in fact, for determining the shock-layer thickness y_s by Eq. (6).

To determine the initial conditions in the axis (plane) of symmetry, we solve the system of ordinary differential equations. These are degenerate equations obtained from (1)–(4) and (7) at $\xi = 0$.

3. THE CALCULATION RESULTS

Initial distributions of the desired functions along the axis of symmetry depend on the curvature K_{s0} of a shock wave. Moreover, for the longitudinal gradients of u, v, T, and p_s entering into the HVSL equations, the evolutionary matrix is degenerate in the sonic line $M_x = 1$ (as is the similar matrix corresponding to the longitudinal gradients of u, v, T, and p in the FVSL equations). Therefore, the integral curves of the HVSL equations, which correspond to different values of K_{s0}, branch in the vicinity of the sonic line. The integral curves of equations describing a viscous mixed flow in the Laval nozzle also behave in a similar way [10, 13]. Thus, in the latter case, a gas-flow rate plays the part of K_{s0}. Similarly to the existence of a unique critical flow rate, there exists a unique "critical" value of K_{s0}. This value is in correspondence with the ultimate integral curve of the HVSL equations, which can be smoothly continued beyond the sonic line; it is the integral curve that represents the desired solution to the problem.

The HVSL equations were solved for the case of $\sigma = 0.95$ in Eq. (9) by the method developed in [13]. We used a difference scheme with fourth (with respect to η) and second (with respect to ξ) orders of accuracy and solved the difference equations by the vector-sweep method at each marching step.

For the flow around a sphere, Fig. 1 shows the distributions of $\left(\frac{\partial\varphi}{\partial\xi}\right)_w$ as functions of the azimuth angle $\theta = \frac{\pi}{2} - \alpha$, which branch off the desired ultimate distribution in the vicinity of the sonic line at $\gamma = 1.4$,

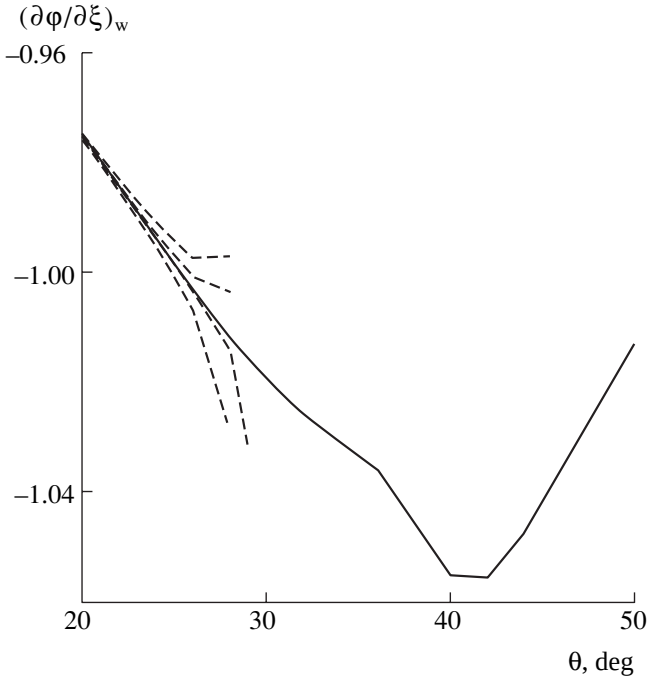

Fig. 1. Branching solutions corresponding to different curvatures K_{s0} of shock waves in the axis of symmetry near the sonic line. Solid and dashed curves correspond to the desired ultimate solution and other solutions, respectively.

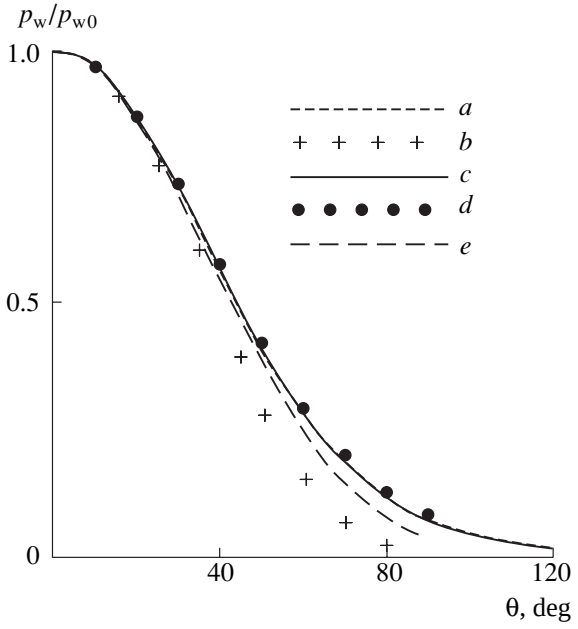

Fig. 2. Distribution (over the sphere surface) of pressure normalized to that at the stagnation point for $M_\infty = 10$, $Re_\infty = 10^3$, and $T_w = 0.2$. The calculations are performed by (*a*) the HVSL model; (*b*) the model from [9] ($Re_\infty = 10^4$); (*c*) the FVSL model, this work; (*d*) the FVSL model, the time-marching method [14]; and (*e*) Euler equations.

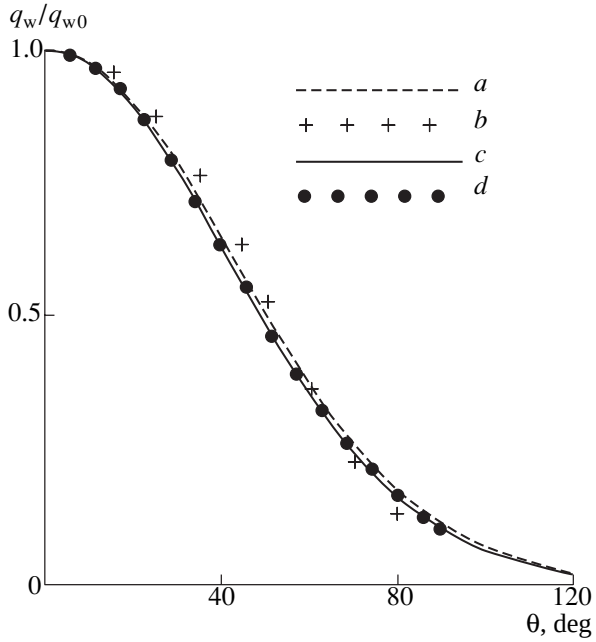

Fig. 3. Distribution (over the sphere surface) of the heat flux normalized to its value at the stagnation point for a sphere at $M_\infty = 7.5$, $Re_\infty = 10^3$, and $T_w = 0.24$. The calculations are performed by (*a*) the HVSL model; (*b*) the model from [9] ($Re_\infty = 10^4$); (*c*) the FVSL model, this work; (*d*) the FVSL model; and the time-marching method [14].

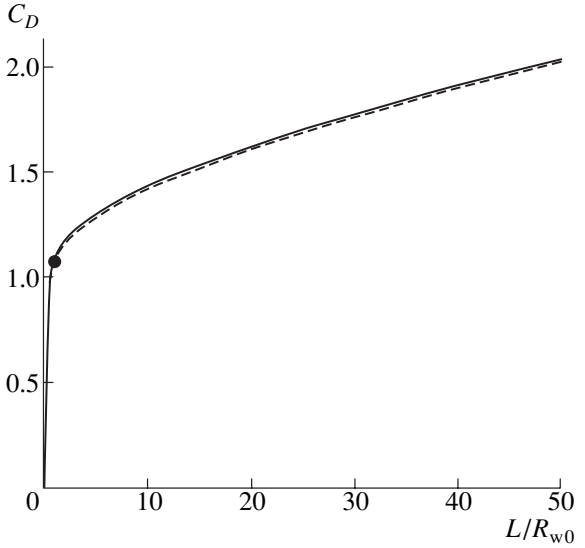

Fig. 4. Coefficient of the total drag for the frontal and lateral surfaces of a cylinder C_D blunted in the shape of a hemisphere as a function of the cylinder length L at $M_\infty = 20$, $Re_\infty = 750$, and $T_w = 0.025$. The calculations are performed by the FVSL model (solid line) and the HVSL model (dashed line). The dot indicates the drag of the hemisphere calculated in [4] by the Navier–Stokes equations.

$\mu \sim T^{0.5}$, Pr = 0.7, $M_\infty = 7.5$, and $Re_\infty = 10^3$. Figure 2 presents the distribution of relative pressure over the surface of a sphere placed in a flow, which are calculated by different models. The elliptic-hyperbolic system of the FVSL equations is solved by the method described in [10] and is based on global iterations with respect to $\frac{\partial \varphi}{\partial \xi}$. The iterations rapidly converge; i.e., for the initial approximation (in the case when it is presented by the HVSL model), even one iteration yields a solution accurate to within 0.5%. According to Fig. 2, the distributions calculated by the HVSL and FVSL models are close to each other. The inaccuracy of the model from [9], which is the best of [8, 9], is noticeable at $\theta > \frac{\pi}{4}$.

Figure 3 shows the distribution of relative heat flux over the sphere surface. We can see that the results of the HVSL and FVSL models are also close to each other. The total resistance of frontal and lateral surfaces, which is calculated by the HVSL and FVSL models for a cylinder blunted in the shape of a hemisphere, is shown in Fig. 4 as a function of the cylinder length L. The dot in Fig. 4 represents the hemisphere drag calculated by the Navier–Stokes equations [4]. The difference between these results is smaller than 1–2%.

Thus, the new hyperbolic model, which is developed for a mixed flow in a viscous shock layer near a blunted body, allows sufficiently accurate calculation of aerodynamic characteristics such as heat flux, pressure, and drag. The model can be used to calculate a flow around a thin body with a length hundreds of times its diameter. The model is developed as a result of a more detailed (compared to [15]) separation of the hyperbolic and elliptic terms of the longitudinal pressure gradient, which are responsible for inviscid disturbance propagation upstream and downstream. The model completely takes into account the mechanisms of the information transfer upstream and, in fact, allows for calculations up to the point of boundary-layer separation. Moreover, this model represents a good initial approximation for performing calculations by the FVSL model and the Navier–Stokes equations.

ACKNOWLEDGMENTS

This work was supported by the Russian Foundation for Basic Research, project no. 00-01-00151.

REFERENCES

1. U. G. Pirumov and G. S. Roslyakov, *Gas Flow in Nozzles* (Mos. Gos. Univ., Moscow, 1978).
2. Yu. P. Golovachev, *Numerical Simulation of Viscous-Gas Flows in Shock Layers* (Nauka, Moscow, 1996).
3. Yu. V. Lapin and M. Kh. Strelets, *Internal Flows of Gas Mixtures* (Nauka, Moscow, 1989).
4. O. M. Belotserkovskiĭ, *Numerical Simulation in Mechanics of Continuous Media* (Nauka, Moscow, 1984).
5. J. C. Williams, AIAA J. **1**, 186 (1963).

6. J. P. Kreskovsky and S. J. Shamroth, Comput. Methods Appl. Mech. Eng. **13**, 307 (1978).
7. B. V. Rogov and I. A. Sokolova, Dokl. Akad. Nauk **345**, 615 (1995) [Phys. Dokl. **40**, 654 (1995)].
8. H. K. Cheng, in *Proceedings of Heat Transfer and Fluid Mechanics Institute* (Stanford Press, Stanford, 1961), pp. 161–175.
9. A. I. Borodin and S. V. Peĭgin, Mat. Model. **5** (1), 16 (1993).
10. N. N. Kalitkin, B. V. Rogov, and I. A. Sokolova, Dokl. Akad. Nauk **374**, 190 (2000) [Dokl. Phys. **45**, 481 (2000)].
11. R. T. Davis, AIAA J. **8**, 843 (1970).
12. C. A. J. Fletcher, *Computational Techniques for Fluid Dynamics* (Springer-Verlag, Berlin, 1988), Vol. 2.
13. N. N. Kalitkin, B. V. Rogov, and I. A. Sokolova, Mat. Model. **11** (7), 95 (1999).
14. A. I. Borodin, V. A. Ivanov, and S. V. Peĭgin, Zh. Vychisl. Mat. Mat. Fiz. **36** (8), 158 (1996).
15. Y. C. Vigneron, J. V. Rakich, and J. C. Tannehill, AIAA Pap., No. 78, 1137 (1978).

Translated by Yu. Verevochkin

Doklady Physics, Vol. 46, No. 6, 2001, pp. 434–439. Translated from Doklady Akademii Nauk, Vol. 378, No. 5, 2001, pp. 633–638.

MECHANICS

Parametric Resonance in Systems with Weak Dissipation

A. P. Seyranian and A. A. Mailybaev

Presented by Academician V.V. Kozlov December 28, 2000

Received December 29, 2000

We consider a linear oscillatory system with many degrees of freedom, whose periodic coefficients are functions of three independent parameters: the frequency and amplitude of a periodic excitation and the parameter of dissipative forces. The last two quantities are assumed to be small. We analyze the instability of the trivial solution (parametric resonance). For an arbitrary periodic-excitation matrix and a positive-definite matrix of the dissipative forces, we derive general expressions for the regions of the main and combination resonances. We study two particular cases for the periodic-excitation matrix that are often encountered in applications: a symmetric matrix and a stationary matrix multiplied by a scalar periodic function. It is shown that in both cases, the resonance regions represent, to a first approximation, cones in the three-dimensional space of the parameters. The relationships obtained allow us to analyze the influence of both the natural frequencies and the resonance number on the instability region. We employ the method of examining parametric-resonance regions which is based on analyzing the behavior of multipliers and uses formulas for the derivatives of the monodromy matrix with respect to the parameters [1, 2]. As an example, the problem on the dynamical stability of the plane bending of a beam loaded by periodic moments is considered.

In referring to previous studies, we should mention book [3], wherein systems close to Hamiltonian systems were studied, as well as papers [4–7], in which systems were transformed to normal coordinates of a conservative system (i.e., the systems for which a transition matrix is required). This paper differs from the previous studies in the statement of the problem and in both the method of analyzing the problem and the results obtained.

1. We consider a linear oscillatory system with periodic coefficients,

$$\mathbf{M}\ddot{\mathbf{y}} + \gamma\mathbf{D}\dot{\mathbf{y}} + (\mathbf{C} + \delta\mathbf{B}(\Omega t))\mathbf{y} = 0. \qquad (1)$$

Here, **M**, **D**, and **C** are the symmetric positive-definite ($m \times m$) matrices of mass, damping, and potential forces, respectively; $\mathbf{B}(\tau)$ is a piecewise continuous 2π-periodic matrix of a parametric excitation; $\mathbf{y} = (y_1, \ldots, y_m)^{\mathrm{T}}$ is the vector of the generalized coordinates; and the point stands for the derivative with respect to time.

We now analyze the stability of the trivial solution $\mathbf{y} \equiv 0$ to system (1) as a function of the vector of three parameters $\mathbf{p} = (\gamma, \delta, \Omega)$ whose components describe the amplitude of dissipative forces and the amplitude and frequency of a periodic excitation, respectively. We assume that the quantities γ and $|\delta|$ are small, i.e., that system (1) is close to an autonomous conservative system. The evident restrictions $\gamma > 0$ and $\Omega > 0$ are imposed on the parameters γ and Ω.

We rewrite (1) as a set of equations of the first order:

$$\dot{\mathbf{x}} = \mathbf{A}(\Omega t)\mathbf{x}, \quad \mathbf{x} = \begin{pmatrix} \mathbf{y} \\ \dot{\mathbf{y}} \end{pmatrix}. \qquad (2)$$

The $(2m \times 2m)$ matrix $\mathbf{A}(\Omega t)$ is a real-valued periodic function with period $T = \dfrac{2\pi}{\Omega}$. The $(2m \times 2m)$ matrix $\mathbf{X}(t)$ satisfying the relationships

$$\dot{\mathbf{X}} = \mathbf{A}(\Omega t)\mathbf{X}, \quad \mathbf{X}(0) = \mathbf{I} \qquad (3)$$

is referred to as a matriciant of system (2), with **I** being the unit matrix. The value of the matriciant at $t = T$ is referred to as a monodromy matrix $\mathbf{F} = \mathbf{X}(T)$ [3]. According to the known theorem on the parameter dependence of solutions to differential equations, the monodromy matrix is a smooth function of the parameter vector **p**. The eigenvalues ρ of the matrix **F** are called multipliers. System (2) is asymptotically stable if all its multipliers are located inside the unit circle on the complex plane, i.e., $|\rho| < 1$. If at least one multiplier is outside of the unit circle, i.e., $|\rho| > 1$, then the system becomes unstable [3].

If $\gamma = \delta = 0$, system (1) is conservative. Seeking its solutions in the form $\mathbf{y} = \mathbf{u}\exp(i\omega t)$, we arrive at the eigenvalue problem

$$\mathbf{Cu} = \omega^2\mathbf{Mu}, \quad \mathbf{u}^{\mathrm{T}}\mathbf{Mu} = 1, \qquad (4)$$

where the second equality is a normalization condition. The real-valued natural frequencies ω and vibration

Institute of Mechanics, Moscow State University, Michurinskiĭ pr. 1, Moscow, 117192 Russia

1028-3358/01/4606-0434$21.00

modes $\mathbf{u}$ are determined from these equations. We assume that all the frequencies $0 < \omega_1 < \omega_2 < \ldots < \omega_m$ are different and denote the corresponding eigenvectors by $\mathbf{u}_j$, with $j = 1, \ldots, m$.

When $\gamma = \delta = 0$, the multipliers of the monodromy matrix $\mathbf{F}_0$ are given by [3]

$$\rho_j, \bar{\rho}_j = \exp(\pm i\omega_j T) = \exp\left(\pm i\frac{2\pi\omega_j}{\Omega}\right), \quad j = 1, \ldots, m. \tag{5}$$

Since all the multipliers ρ_j (5) are at the unit circle $|\rho| = 1$, the stability of system (1) for nonzero γ and δ is determined by perturbations of all the multipliers. In general, all ρ_j are different. Repeated multipliers appear for the following critical values of the frequency Ω:

$$\Omega = \frac{2\omega_j}{k}, \quad j = 1, \ldots, m, \quad k = 1, 2, \ldots; \tag{6}$$

$$\Omega = \frac{\omega_j \pm \omega_l}{k}, \quad j, l = 1, \ldots, m, \quad j > l, \quad k = 1, 2, \ldots \tag{7}$$

Equalities (6) and (7) define, respectively, the main (simple) and combination resonances and correspond to the double multipliers $\rho = (-1)^k$ and $\rho = \exp(i\omega_j T)$. Multipliers of higher order originate only if the quantities $\omega_j \pm \omega_l$ are linked by rational relationships. Here, j, $l = 1, \ldots, m$; $j \geq l$; and $j \neq l$ in the case of $\omega_j - \omega_l$. These cases are nongeneric and will not be considered in this paper.

2. We assume that, for $\gamma = \delta = 0$ and a certain $\Omega = \Omega_0$, all the multipliers of the monodromy matrix $\mathbf{F}_0$ are different. Using the formulas for the derivatives of simple multipliers with respect to parameters [1, 2] and taking (4) into account, we obtain, to a first approximation, the following expression for the modulus of the multiplier of system (2):

$$|\rho_j(\mathbf{p})| = 1 - \frac{\pi\mathbf{u}_j^{\mathrm{T}}\mathbf{D}\mathbf{u}_j}{\Omega_0}\gamma + o(\|\mathbf{p} - \mathbf{p}_0\|), \tag{8}$$

where $\mathbf{p}_0 = (0, 0, \Omega_0)$. It follows from the assumption on the positive definiteness of the dissipative matrix $\mathbf{D}$ that the coefficient of γ in (8) is negative. Therefore, the introduction of small dissipative forces results in the displacement of all the simple multipliers into the interior of the unit circle for small $|\delta|$ and $|\Omega - \Omega_0|$. This implies that small dissipative forces stabilize system (1), which is subjected to weak parametric excitations for noncritical values of the frequency Ω.

3. The instability (parametric resonance) can originate at frequencies Ω close to critical values (6) and (7). Under these conditions, the double multipliers appear at the unit circle. Let the frequency $\Omega = \Omega_0$ of a parametric excitation satisfy the relationship

$$\omega_j + \omega_l = k\Omega_0 \tag{9}$$

for certain frequencies ω_j and ω_l of the conservative system and for a certain natural number k. It is worth noting that condition (9) involves both the case of main resonance (6) for $j = l$ and the case of the summed combination resonance (7) for $j > l$.

Condition (9) implies that two multipliers coincide:

$$\rho_j = \bar{\rho}_l = \exp(i\omega_j T_0), \quad T_0 = \frac{2\pi}{\Omega_0}.$$

Denoting $\rho_0 = \rho_j = \bar{\rho}_l$, we obtain that $\rho_0 = (-1)^k$ for $j = l$ (main resonance), while for $j > l$, ρ_0 is a complex-valued multiplier (combination resonance). The double multiplier ρ_0 is semisimple because two linearly independent eigenvectors correspond to it. Employing the theory of perturbations for multiple eigenvalues [8] and the formulas for the derivatives of the monodromy matrix with respect to the parameters [1, 2], we find the equation for the stability region in the first approximation:

$$\gamma^2(\eta_j + \eta_l)^2\left[\eta_j\eta_l\gamma^2 - \xi_1\delta^2 + k^2\left(\Delta\Omega + \frac{\sigma_+\delta}{k}\right)^2\right] - \left[\xi_2\delta^2 + k(\eta_j - \eta_l)\left(\Delta\Omega + \frac{\sigma_+\delta}{k}\right)\gamma\right]^2 > 0. \tag{10}$$

Here, $\Delta\Omega = \Omega - \Omega_0$, and the coefficients η_j, η_l, σ_+, ξ_1, and ξ_2 are real quantities determined by the relationships

$$\eta_j = \mathbf{u}_j^{\mathrm{T}}\mathbf{D}\mathbf{u}_j, \quad \eta_l = \mathbf{u}_l^{\mathrm{T}}\mathbf{D}\mathbf{u}_l, \quad \sigma_+ = -\frac{\omega_j c_0^{(ll)} + \omega_l c_0^{(jj)}}{2\omega_j\omega_l},$$
$$\xi_1 + i\xi_2 = \frac{c_{-k}^{(jl)} c_k^{(lj)}}{\omega_j\omega_l}, \quad c_k^{(lj)} = \frac{1}{2\pi}\int_0^{2\pi}\mathbf{u}_l^{\mathrm{T}}\mathbf{B}(\tau)\mathbf{u}_j e^{ik\tau}d\tau. \tag{11}$$

It is worth noting that the constants η_j and η_l are positive due to the assumption on the positive definiteness of the dissipative matrix $\mathbf{D}$. Inequality (10) defines the form of the stability region in the three-dimensional space of the parameters $\mathbf{p} = (\gamma, \delta, \Omega)$.

We now consider the critical frequency Ω_0 satisfying the condition

$$\omega_j - \omega_l = k\Omega_0, \quad j > l \tag{12}$$

for a certain natural number k (difference combination resonance). In this case, there is a semisimple double multiplier $\rho_0 = \rho_j - \rho_l$ for $\gamma = \delta = 0$. Then, the first

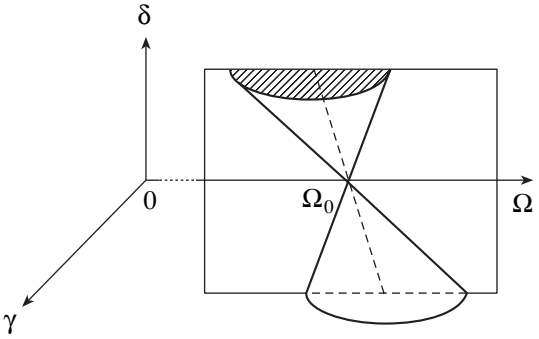

Fig. 1.

approximation for the stability region in the neighborhood of the point $\mathbf{p}_0 = (0, 0, \Omega_0)$ takes the form

$$\gamma^2(\eta_j + \eta_l)^2\left[\eta_j\eta_l\gamma^2 + \xi_1\delta^2 + k^2\left(\Delta\Omega + \frac{\sigma_-\delta}{k}\right)^2\right] - \left[\xi_2\delta^2 - k(\eta_j - \eta_l)\left(\Delta\Omega + \frac{\sigma_-\delta}{k}\right)\gamma\right]^2 > 0. \quad (13)$$

Here, the real coefficients η_j, η_l, ξ_1, and ξ_2 are determined by relationships (11) and the real constant σ_- is given by the equality $\sigma_- = \dfrac{\omega_j c_0^{(ll)} - \omega_l c_0^{(jj)}}{2\omega_j\omega_l}$. Changing the sign of the inequalities in (10) and (13) yields the equation for the boundary of the stability region in the first approximation.

We now analyze the configuration of the instability regions (parametric resonance) in the following most common cases.

(a) Let the parametric-excitation matrix $\mathbf{B}(\Omega t)$ be symmetric. Then, the quantities $c_{-k}^{(jl)}$ and $c_k^{(lj)}$ are complex conjugate. Therefore, $\xi_2 = 0$ and the quantity ξ_1 in (11) takes the form

$$\xi_1 = \frac{c_{-k}^{(jl)}c_k^{(lj)}}{\omega_j\omega_l} = \frac{(a_k^{(jl)})^2 + (b_k^{(jl)})^2}{4\omega_j\omega_l} \geq 0,$$

$$a_k^{(jl)} = \frac{1}{\pi}\int_0^{2\pi}\mathbf{u}_j^{\mathrm{T}}\mathbf{B}(\tau)\mathbf{u}_l\cos(k\tau)d\tau,$$

$$b_k^{(jl)} = \frac{1}{\pi}\int_0^{2\pi}\mathbf{u}_j^{\mathrm{T}}\mathbf{B}(\tau)\mathbf{u}_l\sin(k\tau)d\tau.$$

In the case of main and combined resonances of the summation type (9), stability condition (10) leads to an inequality defining the parametric resonance region (after the reduction of the positive factor):

$$\eta_j\eta_l\gamma^2 - \xi_1\delta^2 + 4k^2\frac{\eta_j\eta_l}{(\eta_j + \eta_l)^2}\left(\Delta\Omega + \frac{\sigma_+\delta}{k}\right)^2 \leq 0. \quad (14)$$

Since the quantities η_j and η_l are positive and $\xi_1 \geq 0$, condition (14) for $\xi_1 \neq 0$ defines the interior of a cone in the three-dimensional space of the parameters $\mathbf{p} = (\gamma, \delta, \Omega)$ (Fig. 1). The cone axis defined by the centers of the conic plane sections at $\delta = \text{const}$ is determined by the equations $\gamma = 0$ and $\Omega - \Omega_0 + \dfrac{\sigma_+\delta}{k} = 0$. In the case of parametric excitation, with a zero mean $c_0^{(jj)} = c_0^{(ll)} = 0$, we have $\sigma_+ = 0$ and, therefore, the cone axis is parallel to the $O\delta$-axis. The stability region corresponds to the exterior of the cone.

When the number k specifying the number of resonances (9) increases at fixed values of ω_j and ω_l, the coefficient ξ_1 decreases as the modulus squared of the Fourier series expansion term. As a result, the instability cone rapidly shrinks with increasing k and the cone axis is straightened. The section of the cone by the plane $\delta = \text{const}$ (with the parametric excitation amplitude fixed) is an ellipse. Because of the factor k^2 in (14), the ellipse shrinks in the direction of the $O\Omega$-axis with increasing k. Since the denominators in (11) contain the products $\omega_j\omega_l$, the quantities ξ_1 and $|\sigma_+|$ decrease with increasing j and l. As a result, the instability cone shrinks and its axis is straightened with increasing j and l, i.e., for resonances at higher frequencies.

In the case of the difference-type combination resonance (12), it follows from stability condition (13) that the parametric-resonance region is defined by the inequality

$$\eta_j\eta_l\gamma^2 + \xi_1\delta^2 + 4k^2\frac{\eta_j\eta_l}{(\eta_j + \eta_l)^2}\left(\Delta\Omega + \frac{\sigma_-\delta}{k}\right)^2 \leq 0. \quad (15)$$

It is noteworthy that inequality (15) differs from (14) only in the sign of the second term and in the coefficient σ_-, which is used in place of σ_+. Consequently, for $\xi_1 \neq 0$ (nondegenerate case), only one of the inequalities (14) and (15) defines a cone, while the other gives the point $\gamma = \delta = \Delta\Omega = 0$ (absence of resonance). Therefore, for positive ξ_1, the region of the difference-type combination resonance is lacking. It is worth noting that, in the case of Hamiltonian systems (without dissipation), the absence of the difference-type combination resonances has already been noted [3].

(b) Let the parametric-excitation matrix have the form $\mathbf{B}(\Omega t) = \varphi(\Omega t)\mathbf{B}_0$, where $\mathbf{B}_0$ is an arbitrary time-independent matrix and $\varphi(\tau)$ is a 2π-periodic scalar

function. In this case, the product $c_{-k}^{(jl)}c_k^{(lj)}$ in (11) is real. Therefore, $\xi_2 = 0$ and the coefficient ξ_1 is given by

$$\xi_1 = \frac{c_{jl}[\alpha_k^2 + \beta_k^2]}{4\omega_j\omega_l}, \quad c_{jl} = \mathbf{u}_j^{\mathrm{T}}\mathbf{B}_0\mathbf{u}_l\mathbf{u}_l^{\mathrm{T}}\mathbf{B}_0\mathbf{u}_j,$$
$$\alpha_k = \frac{1}{\pi}\int_0^{2\pi}\varphi(\tau)\cos(k\tau)d\tau, \quad \beta_k = \frac{1}{\pi}\int_0^{2\pi}\varphi(\tau)\sin(k\tau)d\tau. \tag{16}$$

In the case of the main resonance and the summed combination resonance (9), the stability condition (10) defines the parametric-resonance region (14). For the difference-type combination resonance (12), the instability region is given by (15). In the nondegenerate case, when $\xi_1 \neq 0$, the sign of ξ_1 coincides with that of c_{jl}. For the main resonance, $c_{jj} \geq 0$; therefore, when $c_{jj} \neq 0$, there exists the main-resonance region defined by cone (14). The existence of combination resonance regions depends on the sign of c_{jl}. Namely, for $c_{jl} > 0$ or $c_{jl} < 0$, only the region of the summed or difference-type combination resonance exists, respectively. The shape of the parametric-resonance regions (cones) depends on the resonance number k and the frequencies ω_j and ω_l just as in the case **(a)** described above. When $c_{jl} = 0$, the resonance region is either absent or degenerate (i.e., the first approximation represents a straight line).

We formulate the results obtained in the following statement.

Theorem. *For a symmetric matrix* $\mathbf{B}(\tau) = \mathbf{B}^T(\tau)$, *system* (1) *exhibits only the main resonance* (6) *and the summed combination resonance* (7). *In the case of* $\mathbf{B}(\tau) = \varphi(\tau)\mathbf{B}_0$, *where* $\varphi(\tau)$ *is a periodic scalar function and* $\mathbf{B}_0$ *is a constant matrix, either the main resonances* (6), *the summed combination resonances* (*for* $c_{jl} > 0$), *or the difference-type combination resonances* (*for* $c_{jl} < 0$) *are realized in the system. In the three-dimensional space of the parameters* γ, δ, *and* Ω, *the regions of both main and summed combination resonances are described by cones* (14), *while those of difference-type combined resonances are given by cones* (15).

The cases **(a)** and **(b)** considered above correspond to the most conventional forms of parametric excitations. In other cases, stability conditions (10) and (13) can be used to find the three-dimensional resonance regions. Condition (10) defines the parametric-resonance region (14) (cone) for $\xi_1 > 0$ and $\xi_2 = 0$, while condition (13) describes the resonance region (15) for $\xi_1 < 0$ and $\xi_2 = 0$.

4. We now fix the parameter $\gamma > 0$ and consider the case of $\xi_2 = 0$ [for example, cases **(a)** and **(b)** considered above]. Then, to a first approximation, the parametric-resonance regions are defined by (14) and (15). Depending on the sign of ξ_1, the parametric-resonance region is either absent or occupies the interior of the hyperbolas (conic sections by the plane γ = const) on the two-dimensional plane of the parameters δ and Ω (Fig. 2). The asymptotes of these parabolas are determined by the equation

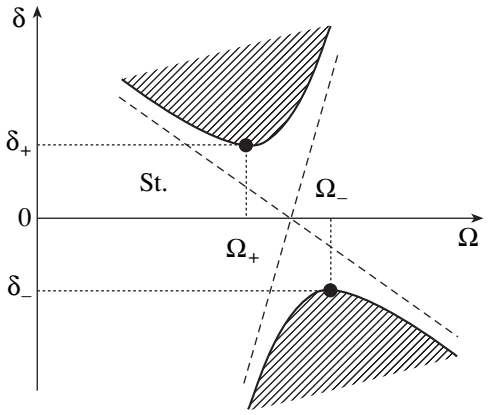

Fig. 2.

$$|\xi_1|^{1/2}\delta \pm 2k\frac{(\eta_j\eta_l)^{1/2}}{\eta_j + \eta_l}\left(\Delta\Omega + \frac{\sigma_s\delta}{k}\right) = 0, \tag{17}$$

where the subscript s stands for "+" and "–" for resonances (9) and (12), respectively. If the average over a period for the matrix $\mathbf{B}(\Omega t)$ is zero, then $\sigma_+ = \sigma_- = 0$. The parametric-resonance region on the plane (δ, Ω) decreases with increasing the dissipative parameter γ. In the first approximation, using (14) or (15), we find the minimum (critical) excitation amplitude $|\delta|$ and the corresponding frequencies at which the parametric resonance is possible:

$$\delta_\pm = \pm\left|\frac{\eta_j\eta_l}{\xi_1}\right|^{1/2}\gamma, \quad \Omega_\pm = \Omega_0 - \frac{\sigma_s\delta_\pm}{k}. \tag{18}$$

Here, Ω_0 is the resonance frequency given by (9) or (12), depending on the resonance type (Fig. 2).

5. As an example, we now consider Bolotin's problem [5, 9] on the dynamic stability of the plane bending of a beam. The elastic beam is assumed to be simply supported at its ends and loaded by the periodic moments $M(\Omega t) = \delta\varphi(\Omega t)$ in the plane of its maximum stiffness, where $\varphi(\tau)$ is a 2π-periodic function. Bending-torsional vibrations off this plane are described by the equations [9]

$$m\frac{\partial^2 w}{\partial t^2} + \gamma m d_1\frac{\partial w}{\partial t} + \mathrm{EJ}\frac{\partial^4 w}{\partial x^4} + \delta\varphi(\Omega t)\frac{\partial^2\theta}{\partial x^2} = 0,$$
$$mr^2\frac{\partial^2\theta}{\partial t^2} + \gamma m r^2 d_2\frac{\partial\theta}{\partial t} + \delta\varphi(\Omega t)\frac{\partial^2 w}{\partial x^2} - \mathrm{GI}\frac{\partial^2\theta}{\partial x^2} = 0. \tag{19}$$

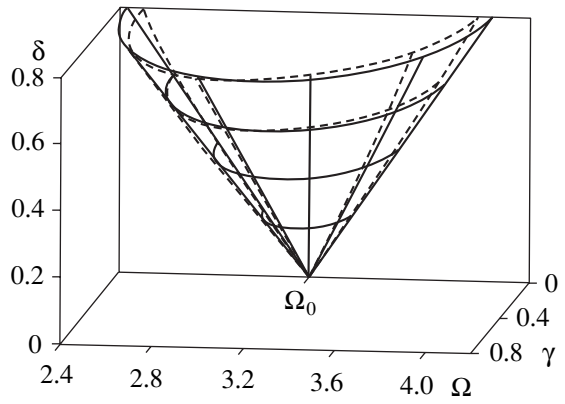

Fig. 3.

Here, $w(x, t)$ is the transverse deflection of the beam; $\theta(x, t)$ and r are the torsion angle and the radius of inertia for the beam's cross section, respectively; EJ and GI are the bending and torsion stiffnesses of the beam, respectively; m is the mass per unit length of the beam; γ is the parameter of dissipative force (viscous friction); and d_1 and d_2 are fixed constants defining the bending and torsional friction forces. The boundary conditions take the form

$$x = 0, l: w = \frac{\partial^2 w}{\partial x^2} = \theta = 0, \tag{20}$$

where l is the beam length. We seek the solution to system (19), (20) in the form of a series [5]:

$$\begin{aligned} w(x, t) &= \sum_{n=1}^{\infty} W_n(t) \sin\frac{n\pi x}{l}, \\ \theta(x, t) &= \sum_{n=1}^{\infty} \Theta_n(t) \sin\frac{n\pi x}{l}, \end{aligned} \tag{21}$$

where $W_n(t)$ and $\Theta_n(t)$ are unknown functions of time. Substituting (21) into Eq. (19), we obtain a set of ordinary differential equations with respect to $W_n(t)$ and $\Theta_n(t)$ of the form of (1) with

$$\mathbf{M} = \begin{pmatrix} 1 & 0 \\ 0 & 1 \end{pmatrix}, \quad \mathbf{D} = \begin{pmatrix} d_1 & 0 \\ 0 & d_2 \end{pmatrix}, \quad \mathbf{C} = \begin{pmatrix} \omega_{n1}^2 & 0 \\ 0 & \omega_{n2}^2 \end{pmatrix},$$

$$\mathbf{B}(\Omega t) = \varphi(\Omega t)\begin{pmatrix} 0 & -\dfrac{\pi^2 n^2}{l^2 m} \\ -\dfrac{\pi^2 n^2}{r^2 l^2 m} & 0 \end{pmatrix}, \quad \mathbf{y} = \begin{pmatrix} W_n \\ \Theta_n \end{pmatrix}. \tag{22}$$

Here, ω_{n1} and ω_{n2} are the natural frequencies of bending and torsional vibrations of the beam, respectively:

$$\omega_{n1} = \frac{n^2\pi^2}{l^2}\sqrt{\frac{EJ}{m}}, \quad \omega_{n2} = \frac{n\pi}{rl}\sqrt{\frac{GI}{m}}, \quad n = 1, 2, \ldots \tag{23}$$

The eigenvectors corresponding to the frequencies ω_{n1} and ω_{n2} are equal to $\mathbf{u}_{n1} = (1, 0)^T$ and $\mathbf{u}_{n2} = (0, 1)^T$, respectively.

We now analyze the stability of system (1) with matrices (22) for a certain fixed n. Since $\mathbf{B}(\Omega t) = \varphi(\Omega t)\mathbf{B}_0$, where $\mathbf{B}_0$ is a fixed matrix, this system belongs to the type considered in item **(b)**. The quantities determined from Eqs. (16) take the form

$$c_{11} = c_{22} = 0, \quad c_{12} = \frac{\pi^4 n^4}{l^4 r^2 m^2} > 0. \tag{24}$$

Therefore, the regions of the difference-type combination resonance are absent, while the main resonance regions are degenerate (in order to analyze them, higher approximations are required). According to (14), the regions of the summed combination resonance at frequencies close to $\Omega_0 = \dfrac{\omega_{n1} + \omega_{n2}}{k}$, $k = 1, 2, \ldots$ are defined by

$$d_1 d_2 \gamma^2 - \frac{c_{12}(\alpha_k^2 + \beta_k^2)}{4\omega_{n1}\omega_{n2}}\delta^2 + 4k^2\frac{d_1 d_2}{(d_1 + d_2)^2}\Delta\Omega^2 \le 0, \tag{25}$$

where the quantities α_k and β_k are determined from (16).

To carry out numerical calculations, we set $n = 1$, $\varphi(\tau) = \cos\tau$, $d_1 = d_2 = 1$, $\omega_{n1} = 1$ s^{-1}, $\omega_{n2} = \sqrt{5}$ s^{-1}, $l^2 m = \dfrac{\pi^2}{4}$ kg cm, and $r^2 = \dfrac{4}{\sqrt{5}}$ cm^2. The boundary of the combination resonance region (with $k = 1$) given by (25) in the first approximation is shown in Fig. 3 (solid curves). The same quantity obtained by numerical evaluation of the monodromy matrix for various values of the parameters γ, δ, and Ω is also shown (dashed curves). The Runge–Kutta method was employed to integrate Eqs. (3). It is seen from Fig. 3 that the exact (obtained numerically) and approximate regions of the combination resonance are well matched up to the amplitudes $\delta \approx 0.8$.

This work was supported by the Russian Foundation for Basic Research, project no. 99-01-39129.

REFERENCES

1. A. P. Seyranian, F. Solem, and P. Pedersen, Arch. Appl. Mech. **69**, 160 (1999).

2. A. A. Mailybaev and A. P. Seyranian, Prikl. Mat. Mekh. **64**, 947 (2000).
3. V. A. Yakubovich and V. M. Starzhinskiĭ, *Parametric Resonance in Linear Systems* (Nauka, Moscow, 1987).
4. C. S. Hsu, J. Appl. Mech. **30**, 367 (1963).
5. *Vibrations in Technique*, Vol. 1: *Oscillations of Linear Systems*, Ed. by V. V. Bolotin (Mashinostroenie, Moscow, 1978).
6. G. Schmidt, *Parametererregte Schwingungen* (VEB Deutscher Verlag der Wissenschaften, Berlin, 1975; Mir, Moscow, 1978).
7. S. V. Chelomeĭ, Dokl. Akad. Nauk SSSR **252**, 307 (1980) [Sov. Phys. Dokl. **25**, 366 (1980)].
8. A. P. Seyranian, Strojnicky Casopis **42** (3), 193 (1991).
9. V. V. Bolotin, in *Nonlinear Stability of Structures. Theory and Computational Techniques*, Ed. by A. N. Kounadis and W. B. Kratzig (Springer, New York, 1995), pp. 3–72.

Translated by V. Chechin

Doklady Physics, Vol. 46, No. 6, 2001, pp. 440–444. Translated from Doklady Akademii Nauk, Vol. 378, No. 6, 2001, pp. 758–762.

MECHANICS

On a Unique and Complete Description of the Axisymmetric Supercritical Behavior of a Shallow Spherical Cup

Corresponding Member of the RAS É. I. Grigolyuk and E. A. Lopanitsyn

Received February 5, 2001

The problem of supercritical behavior of shells involving the determination of their stable and unstable equilibrium states after they have lost their stability has been rather poorly studied. This problem is closely associated with the calculation of the shell nonlinear stress-strain state before buckling, as well as with the attainment of stability under the conditions of a preliminary nonlinear stress-strain state.

In this regard, shallow spherical cups, along with cylindrical shells, are the most thoroughly investigated. To describe the behavior of shallow shells with a finite bending, the so-called Marguerre equations are most often used. Attempts to completely solve the problem of supercritical behavior of an ideal shallow spherical cup were performed by H. Weinitschke [9] (1960), G. Thurston [8] (1961), D. I. Shilkrut, *et al.* [5] (1969), L. Bauer *et al.* [6] (1973), and N.V. Valishvili [1] (1976). However, only Mescall [7], in 1966, succeeded in solving this problem. In Fig. 1, we show the loading trajectory of a shallow spherical cup with a rigidly fixed contour; this cup is subjected to the action of a uniform transverse pressure [7]. Here, q^* and w_0^* denote the dimensionless transverse loading and the relative deflection at the cup pole.

As is seen in Fig. 1, the cup loading trajectory exhibits its points of intersection. This fact led Mescall to an erroneous conclusion on the existence of bifurcation points in this trajectory. Moreover, this statement was repeated in various publications dedicated to the stability of shells, e.g., in [2]. In fact, there cannot be bifurcation points in the shell-loading trajectory, provided the shell deformation is axisymmetric. Only ultimate points that correspond to the state of indifferent equilibrium of the shell can exist there. In the vicinity of these ultimate points, the shell may loose its stability through snapping. Bifurcation points appear in the loading trajectory when there is a possibility of asymmetric shell deformation. These points correspond to states of shell indifferent equilibrium in which an Eulerian buckling may occur accompanied by the appearance of asymmetric forms of shell bending.

Unfortunately, after Mescall had published this paper, nobody succeeded in completely reproducing the process of cup supercritical deformation. No studies follow those of Mescall. This was likely associated with computational difficulties in solving the nonlinear equations. Therefore, the question of the appearance of bifurcation points in the loading trajectory of a shallow spherical shell under the condition of its axisymmetric deformation alone remained open.

The goal of this study is to solve a complete problem on the finite bending of a shallow spherical cup rigidly fixed around its contour under the action of uniform transverse pressure. On the basis of this solution, we also try to elucidate the types of singular points present in the cup loading trajectory under the condition of axisymmetric deformation alone.

We consider a shallow spherical cup with curvature radius R and thickness h. Let the cup rigidly fixed around its contour and having a radius a be subjected to the action of uniform transverse pressure q. The prob-

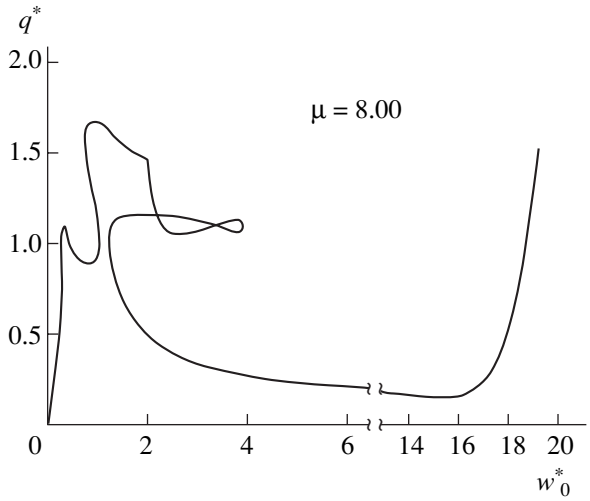

Fig. 1. Loading trajectory for the thin-walled shallow spherical cup. The solution by Mescall.

Moscow State Technical University
"Moscow Automotive Institute,"
ul. Bol'shaya Semenovskaya 38, Moscow, 105830 Russia

1028-3358/01/4606-0440$21.00

lem of the cup axisymmetric snapping and supercritical behavior in the variational formulation on the basis of the Margerr equation involves two functions u and ϑ_r that vary independently. These functions describe, respectively, the radial displacements of middle-surface points and the rotation angle of a surface normal with respect to this surface. Such a formulation follows from the Lagrange principle, written out, for this case, in the form

$$(rN_{rr}\delta u - rM_{rr}\delta\vartheta_r)\Big|_0^a - \int_0^a \left\{\frac{1}{r}[(rN_{rr})' - N_{\Theta\Theta}]\delta u - \left[\frac{1}{r}((rM_{rr})' - M_{\Theta\Theta}) + \frac{r}{R}N_{rr} + N_{rr}\vartheta_r + \frac{r}{2}q\right]\delta\vartheta_r\right\} rdr = 0, \quad (1)$$

where N_{rr}, $N_{\Theta\Theta}$, and M_{rr} with $M_{\Theta\Theta}$ are, respectively, specific normal forces and specific bending moments arising in the shell.

These force functions and the shell deflection are unambiguously described by the independently varying functions u and ϑ_r. These functions are represented by finite sums:

$$u = \sum_{i=1}^{K} U_i u_i(r), \quad \vartheta_r = \sum_{i=1}^{K} \Theta_i \vartheta_i(r). \quad (2)$$

In these sums, U_i and Θ_i are the unknown generalized displacements, while $u_i(r)$ and $\vartheta_i(r)$ are the basis functions given with the help of Bessel functions and obeying the boundary conditions of the problem:

$$u = \vartheta_r = 0 \text{ at } r = 0, \quad u = \vartheta_r = 0 \text{ at } r = a.$$

Thus, we can write out Eqs. (1) of the shell equilibrium in the form of a set of nonlinear algebraic equations:

$$\mathbf{F}(\mathbf{X}) = \mathbf{0}. \quad (3)$$

Here, we imply that the vector $\mathbf{F} = (F_1F_2\ldots F_{2K})^{\mathrm{T}}$ consists of summands standing in the left-hand side of Eq. (1) with variations of generalized displacements U_i and Θ_i ($i = 1, 2, 3, \ldots, K$). In this case, the vector $\mathbf{X}$, in accordance with the concept of equivalence of all solution variables, is composed of generalized displacements including transverse loading:

$$\mathbf{X} = (U_1\Theta_1\ldots U_K\Theta_K\, q)^{\mathrm{T}}.$$

The order of vector $\mathbf{X}$ is determined by the number of terms taken into account in partial sums (2): $N_{\max} = 2K + 1$.

The solution to the set of nonlinear algebraic equations (3) is constructed by the continuous-extension method. In accordance with [4], the basis of the method consists in numerical solution of the Cauchy problem [equivalent to the set of equations (3)] with zero initial conditions, which corresponds to the unloaded-shell state. A method of the discrete extension [3] is used to compensate for errors in the components of vector $\mathbf{X}$. These errors are accumulated when numerically solving the equivalent set of equations. The method of discrete extension is based on Newton's method realized for an extended space of variables. Such an approach makes it possible to determine the solution vector $\mathbf{X}$ with a preassigned error at an arbitrary regular point in the loading trajectory, including its ultimate points.

As a result of this solution, the shell-loading trajectory, i.e., the locus corresponding to its equilibrium states, turns out to be a certain curve in a space with dimension $N_{\max}$, which is determined by a number of independent variables of the solution. This number depends on the degree of problem discretization. Therefore, a question arises as to the least number of shell characteristics necessary for sufficient, complete description of the shell deformation process. The sufficiently complete description implies a representation (as a rule, graphical) of the process under consideration that adequately reflects all evolutions of the shell stress-strain state without loosing the essence of the process.

To solve this problem, we now return to variational equation (1). The force variables entering into this equation are unambiguously described by independent functions u and ϑ_r. Thus, the potential energy of the shell deformation is unambiguously given by any two functions taken from the pairs u_i and N_{rr} or ϑ_r and M_{rr}. This implies that each of the several possible stress-strain states for a given loading is assigned uniquely to two cup characteristics alone. They can be any two taken from the above pairs. Using two such functions, we can reconstruct (for a given loading) the stress-strain state of the shell without solving the equation of the shell equilibrium. Therefore, these functions, together with the value of the applied loading, unambiguously and sufficiently completely describe the stress-strain state of a cup at each point of a loading trajectory.

Each of the chosen functions can be characterized by its norm or its value at a characteristic point for which the cup pole is usually taken. Since the functions u and ϑ_r have zero values at the cup pole, $N_{rr}(0)$ and $M_{rr}(0)$ should be chosen as the cup-state parameters. Hence, in order for the loading trajectory to unambiguously and completely describe an arbitrary stress-strain state of a cup in any method and for arbitrary degree of problem discretization, it is sufficient to describe and construct this trajectory in the three-dimensional space of variables $N_{rr}(0)$, $M_{rr}(0)$, and q.

This conclusion may be confirmed by other considerations based on the variational formulation of the problem of finite deflections for a shallow spherical

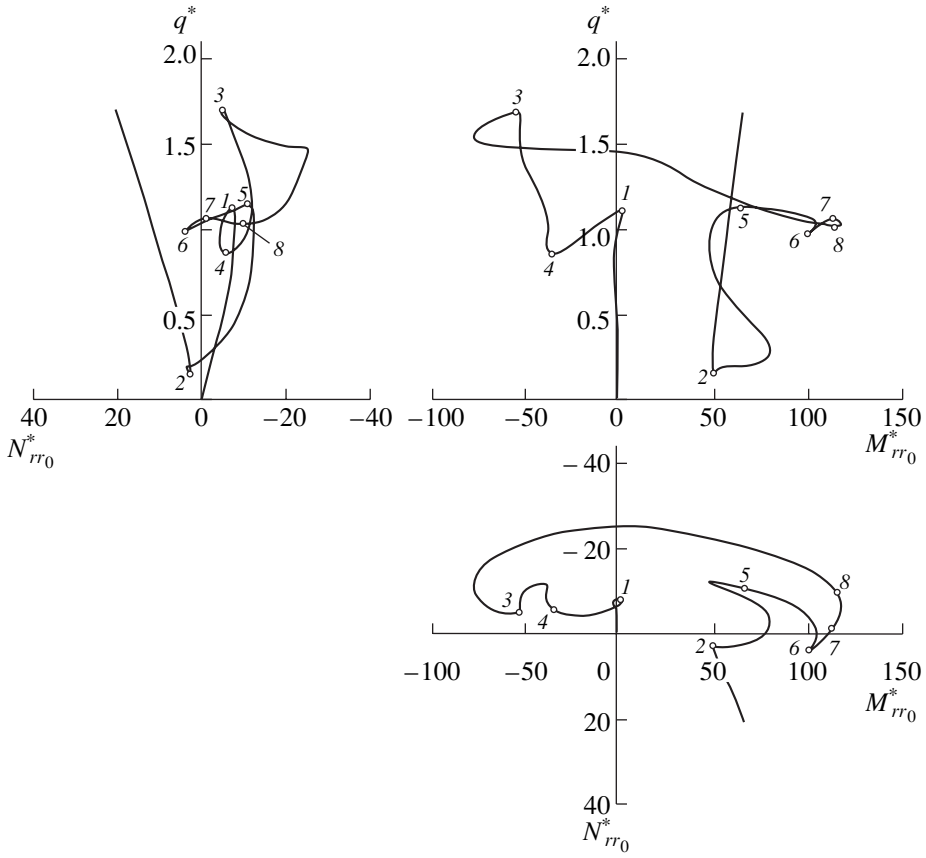

Fig. 2. Projection of the loading trajectory for the thin-walled shallow spherical cup, $\mu = 8.00$.

cup. To determine its stress-strain state, instead of the boundary value problem

$$\frac{1}{r}[(rN_{rr})' - N_{\Theta\Theta}] = 0 \quad (0 \le r \le a),$$

$$\frac{1}{r}[(rM_{rr})' - M_{\Theta\Theta}] + \frac{r}{R}N_{rr} + N_{rr}\vartheta_r + \frac{r}{2}q = 0, \quad (4)$$

$$u(0) = 0, \quad \vartheta_r(0) = 0, \quad u(a) = 0, \quad \vartheta_r(a) = 0,$$

we can write out the Cauchy problem that provides a similar solution for a given loading q:

$$\frac{1}{r}[(rN_{rr})' - N_{\Theta\Theta}] = 0 \quad (0 \le r \le a),$$

$$\frac{1}{r}[(rM_{rr})' - M_{\Theta\Theta}] + \frac{r}{R}N_{rr} + N_{rr}\vartheta_r + \frac{r}{2}q = 0,$$

$$u(0) = 0, \quad \vartheta_r(0) = 0,$$

$$N_{rr}(0) = N_{rr0}, \quad M_{rr}(0) = M_{rr0}.$$

Here, N_{rr0} and M_{rr0} are, respectively, the specific normal radial forces and the specific bending moment at the cup pole, which are found from the solution to the boundary value problem (4) for a given loading q. This confirms the conclusion that three values, namely, $N_{rr}(0)$, $M_{rr}(0)$, and q, are sufficient for unambiguous description of the stress-strain state of a shallow spherical cup.

The description of the trajectory for an axisymmetric cup deformation in the space of variables $N_{rr}(0)$, $M_{rr}(0)$, and q is not unique. This is explained by the fact that the shell deflection w can be unambiguously determined by the radial bending moment M_{rr}. This is why the value of the radial bending moment $M_{rr}(0)$ at the cup pole can be replaced by the deflection $w(0)$, also calculated at the same point, without a loss of uniqueness and completeness in description of the loading trajectory. Thus, it is possible to construct one more space of variables $N_{rr}(0)$, $w(0)$, and q, which provides unambiguous and complete description of the loading trajectory for a shallow spherical cup.

We construct the loading trajectory for a shallow spherical cup, which is calculated on the basis of the solution to the system of equations (3) for the thin-wall parameter $\mu = 8.00$. The construction is performed in the space of variables for which we take the specific radial forces, the bending moment in the cup pole, and the transverse loading. Three projections of the trajectory in the space $\{M^*_{rr0}, q^*\}$, $\{N^*_{rr0}, q^*\}$, and $\{M^*_{rr0},$

N^*_{rr0} } are shown in Fig. 2. Here, q^* is the dimensionless transverse load,

$$q^* = \frac{1}{2}\sqrt{3(1-\nu^2)}\frac{qR^2}{Eh^2},$$

ν is the Poisson's ratio for the shell material, and E is its elastic modulus. We consider

$$\mu = \sqrt[4]{12(1-\nu^2)}\sqrt{\frac{a^2}{Rh}}$$

the cup thin-wall parameter. The quantities N^*_{rr0} and M^*_{rr0} denote dimensionless specific normal radial forces and the specific bending moment at the cup pole, namely,

$$N^*_{rr0} = (1-\nu^2)\frac{a^2}{Eh^3}N_{rr}(0),$$

$$M^*_{rr0} = 12(1-\nu^2)\frac{a^2}{Eh^4}M_{rr}(0).$$

The projections of the loading trajectory in the coordinates $\{M^*_{rr0}, q^*\}$ and $\{N^*_{rr0}, q^*\}$ characterize the shell deflection and the shell tension–compression, respectively. The third projection of the loading trajectory in the coordinates $\{M^*_{rr0}, N^*_{rr0}\}$ has an adjusting character. In these projections, the ultimate points of the loading trajectory are denoted by numbers 1 to 8. As is shown in Fig. 3, these three projections correspond to a single curve in the space $\{M^*_{rr0}, N^*_{rr0}, q^*\}$. In this space, each point of the loading trajectory corresponds to only one stress-strain equilibrium state of the cup. Moreover, this result is valid for an arbitrary degree of shell discretization, when tens, hundreds, or thousands of desired generalized shell displacements are included into the number of unknowns of the solution to the set of nonlinear algebraic equations of equilibrium.

As is seen in Fig. 3, the loading trajectory of a shallow cup is a smooth curve having no points of intersection. At the same time, any projection of the loading trajectory in Fig. 2 has at least one point of intersection. This fact led Mescall, who published a paper devoted to the projection of a loading trajectory in coordinates $\{w^*_0, q^*\}$ (Figs. 1, 4), to a wrong conclusion on the existence in this trajectory of bifurcation points. In fact, as is seen in Fig. 3, under the condition that axisymmetric shell deformation alone is possible, the loading trajectory cannot have bifurcation points. Only ultimate points can exist in it. The points of intersection of the loading trajectory, which were accepted by Mescall as bifurcation points (Fig. 4), are, in fact, its regular

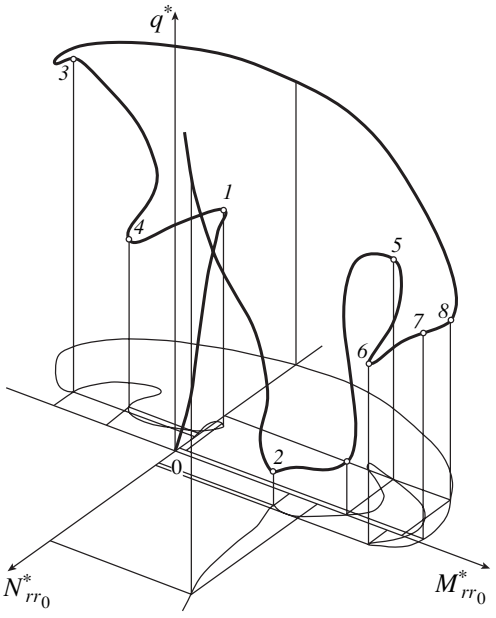

Fig. 3. Loading trajectory for the thin-walled shallow spherical cup, $\mu = 8.00$.

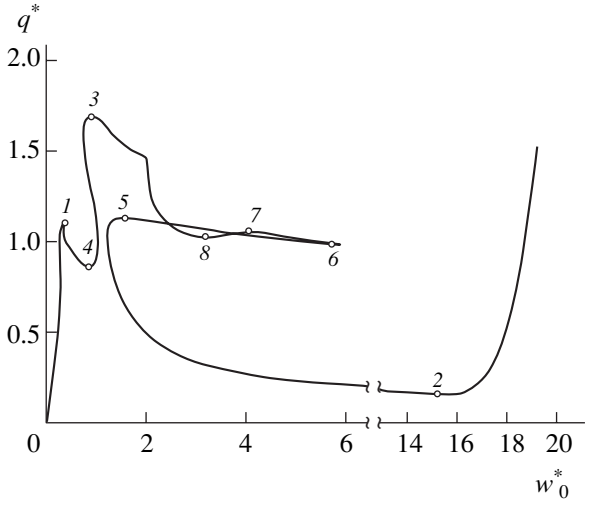

Fig. 4. Projection of the loading trajectory for the thin-walled shallow spherical cup in the coordinates $\{w^*_0, q^*\}$, $\mu = 8.00$.

points. They are the only points of intersection for the regions of projection of the loading trajectory that belongs to the extended space of variables. At the same time, the trajectory in itself has no points of intersection in this space (Fig. 3). The same arguments can be related to cusps. The loading trajectory of a shallow spherical cup has no cusps. This trajectory contains points belonging to regions with a small (compared to other regions) radius of curvature. They may be assumed to be cusps. However, in fact, the loading trajectory of a cup is a smooth curve.

ACKNOWLEDGMENTS

This work was performed under the financial support of the Competitive Center of Fundamental Natural Science.

REFERENCES

1. N. V. Valishvili, *Computer Calculation Methods for Shells of Revolution* (Mashinostroenie, Moscow, 1976).
2. É. I. Grigolyuk and V. V. Kabanov, *Stability of Shells* (Nauka, Moscow, 1978).
3. É. I. Grigolyuk and E. A. Lopanitsyn, Prikl. Mekh. Tekh. Fiz., No. 5, 95 (1990).
4. É. I. Grigolyuk and E. A. Lopanitsyn, Dokl. Akad. Nauk **335**, 582 (1994) [Phys. Dokl. **39**, 254 (1994)].
5. D. I. Shil'krut, N. V. Shevandorov, V. P. Morar, and Yu. A. Maksimov, *Solving Problems of Nonlinear Theory of Shells by Analog Computers* (Akad. Nauk Mold. SSR, Kishinev, 1969).
6. L. Bauer, E. L. Reiss, and H. B. Keller, Int. J. Non-Linear Mech. **8**, 31 (1973).
7. J. Mescall, AIAA J. **4**, 2041 (1966).
8. G. A. Thurston, J. Appl. Mech. **28**, 557 (1961).
9. H. Weinitschke, J. Math. Phys. (Cambridge, Mass.) **38** (4), 209 (1960).

Translated by G. Merzon

Doklady Physics, Vol. 46, No. 6, 2001, pp. 445–451. Translated from Doklady Akademii Nauk, Vol. 378, No. 6, 2001, pp. 763–768.

MECHANICS

Two-Dimensional Pressure Waves in a Liquid Containing Bubble Zones

Academician R. I. Nigmatulin, V. Sh. Shagapov, I. K. Gimaltdinov, and M. N. Galimzyanov

Received February 15, 2001

To date, one-dimensional waves in a liquid containing bubbles (bubble liquid) have been thoroughly investigated [1, 2]. In this paper, we study the evolution of two-dimensional waves in such a liquid. We consider a case of a plane impact upon a liquid containing a finite-size bubble zone, as well as a case of concentrated impact upon a homogeneous bubble-containing liquid. Horseshoe-shaped soliton waves are revealed whose propagation qualitative features are similar to analogous wave patterns in plasma [3].

Let a bubble zone be located in a liquid which, in the general case, is bounded by a cylindrical surface whose generatrix is parallel to the z-axis (the zone longitudinal size is much longer than the transverse one). We consider two-dimensional wave disturbances. This situation can be realized, e.g., in the case of an action on the system boundary of a pressure independent of the z-coordinate [$p = p^0(t, y)$] for $x = x_0$.

In order to describe the motion of the bubble liquid under assumptions which are usual for these systems, we write out a set of equations for the masses, number of bubbles, momenta, and pressure in the bubbles in the one-velocity approximation [1]:

$$\frac{d\rho_i}{dt} + \rho_i\left(\frac{\partial u}{\partial x} + \frac{\partial v}{\partial y}\right) = 0, \quad i = l, g,$$

$$\frac{dn}{dt} + n\left(\frac{\partial u}{\partial x} + \frac{\partial v}{\partial y}\right) = 0,$$

$$\rho\frac{du}{dt} + \frac{\partial p_l}{\partial x} = 0, \quad \rho\frac{dv}{dt} + \frac{\partial p_l}{\partial y} = 0,$$

$$\frac{dp_g}{dt} = -\frac{3\gamma p_g}{a}w - \frac{3(\gamma-1)}{a_0}q, \qquad (1)$$

$$w = \frac{da}{dt}, \quad \frac{d}{dt} = \frac{\partial}{\partial t} + u\frac{\partial}{\partial x} + v\frac{\partial}{\partial y},$$

$$\alpha_l + \alpha_g = 1, \quad \alpha_g = \frac{4}{3}\pi a^3 n,$$

$$\rho_i = \rho_i^0\alpha_i, \quad \rho = \rho_g + \rho_l.$$

Here, a is the bubble radius, γ is the adiabat index for a gas, p_i is the phase pressure, ρ_i^0 are phase true densities, α_i are volume phase contents, q is the heat-transfer intensity, n is the number of bubbles per unit volume, and w is the radial bubble density. The velocities u and v correspond to the motion along the x- and y-coordinates. We label the parameters of the liquid and gaseous phases by the subscripts $i = l, g$, respectively.

While describing the radial motion, in accordance with the refinements proposed in [4], we assume that the velocity of this motion consists of two components:

$$w = w_R + w_A, \qquad (2)$$

where w_R is described by the Rayleigh–Lamb equation

$$a\frac{dw_R}{dt} + \frac{3}{2}w_R^2 + 4\nu_l\frac{w_R}{a} = \frac{p_g - p_l}{\rho_l^0} \qquad (3)$$

and ν_l is the viscosity of the liquid. The additional velocity w_A is determined from the solution (in the acoustical approximation) to the problem of spherical unloading on a sphere with radius a in a carrier liquid:

$$w_A = \frac{p_g - p_l}{\rho_l^0 C_l \alpha_g^{1/3}}, \qquad (4)$$

where C_l is the sound velocity in the liquid. We assume that the liquid is acoustically compressible and the gas is calorically perfect:

$$p_l = p_0 + C_l^2(\rho_l^0 - \rho_{l0}^0), \quad p_g = \rho_g^0 R T_g, \qquad (5)$$

Sterlitamak Branch, Academy of Sciences of Republic Bashkortostan, pr. Lenina 37, Sterlitamak, Bashkortostan, 453103 Russia

1028-3358/01/4606-0445$21.00

where R and T_g are, respectively, the gas constant and temperature of the gas. Henceforth, the subscripts 0 indicate that the corresponding parameter relates to the initial unperturbed state.

The heat flow q is given by the approximate finite relation

$$q = \mathrm{Nu}\lambda_g\frac{T_g - T_0}{2a}, \quad \frac{T_g}{T_0} = \frac{p_g}{p_0}\left(\frac{a}{a_0}\right)^3,$$

where $T_0 = \mathrm{const}$ is the temperature of the liquid, λ_g is the heat conductivity, and Nu is the Nusselt number. For the bubble liquid described above, the equilibrium sound velocity C and the Minnaert frequency ω_M of the bubble free oscillations are determined as [1]

$$C = \sqrt{\frac{\gamma p_0}{\rho_{10}\alpha_{g0}}}, \quad \omega_M = \frac{1}{a_0}\sqrt{\frac{3\gamma p_0}{\rho_{10}}}.$$

For numerical analysis of the evolution of nonlinear waves in a bubble liquid, it is more convenient to use the system of equations presented here and written out in Lagrange variables. We take initial Eulerian coordinates as these variables. This choice is associated, in particular, with the fact that the bubble screen written out in Lagrange coordinates is immovable.

The results of the numerical experiment are illustrated in Figs. 1 and 2, in which the evolution of the wave pulse initiated by a plane impact at the boundary $x_0 = 0$ in a water volume containing an air-bubble screen of the rectangular cross section is presented:

$$p^0(t, y) = p_0 + \Delta p_0 \exp\left[-\left(\frac{t - \delta t/2}{\delta t/2}\right)^2\right].$$

A semi-infinite channel is taken as a calculation domain. On the boundaries of this domain ($x_0 = 0$, $0 < y_0 < L_y$, $y_0 = 0$, and $y = L_y$), the conditions are assumed to be the same as those on a rigid wall. It should be mentioned that in the present study, we consider a case when the wave pulse, being completely formed, interacts with the bubble screen. The calculation region is taken to be sufficiently broad in order to avoid the effect of secondary signals produced as a result of reflections from the boundaries of the calculation domains during a period of the wave-pulse action. In this and subsequent calculations, the pressure distribution is symmetric with respect to the straight line $y = \frac{L_y}{2}$. Therefore, the calculation results (spatial pressure distributions) are presented for one of the half-planes separated by this straight line. It is seen that when propagating a longer signal (Fig. 2), tower-shaped pressure distributions can be produced at certain time moments in the screen pressure sensors owing to two-dimensional effects. In this case, pressure sensors placed at these points record significant pressure bursts. In the example under analysis, the $D2$ sensor located in the middle of the bubble screen records signals with amplitudes of about 6 atm, which exceeds the amplitude of the initial signal by a factor of two. This tower-shaped pressure burst decreasing in amplitude is carried away along the direction of the basic-wave propagation. This picture can be seen from the calculated oscillogram for the $D3$ sensor (the recorded amplitude exceeds the initial one by almost 1 atm). In the case of a short signal (Fig. 1), the $D2$ sensor placed in the middle of the same screen virtually does not record an external pulsed signal, while the $D3$ sensor acquires only a weakened signal with an amplitude of about 1 atm. Thus, when pulsed signals propagate in a liquid containing a finite-size bubble screen and the time duration of each signal is sufficiently long $\left(\delta t > \frac{l_y}{C}\right)$, it is quite possible that, inside the screen, there is an elevation of the pressure amplitude such that it can exceed the amplitude of the initial pulse. In the case of sufficiently short pulses $\left(\delta t \le \frac{l_y}{C}\right)$, particles of the two-phase system inside the screen virtually do not feel the propagation of the wave pulse (as if completely protected from its action).

Figures 3 and 4 represent spatial pressure distributions evolving along the transverse coordinate of the wave pulse given in the form

$$p^0(t, y) = p_0 + \Delta p_0 \exp\left[-\left(\frac{t - \delta t/2}{\delta t/2}\right)^2\right] \times \exp\left[-\left(\frac{y - L_y/2}{\delta y/2}\right)^2\right] \quad (6)$$

and acting through the Lagrange boundary $x_0 = 0$ in the homogeneous water–air bubble mixture. It is seen that in the case of a longer pulse (Fig. 3) whose characteristic duration greatly exceeds the period of bubble free oscillations ω_M^{-1} [i.e., ($\delta t \gg \omega_M^{-1}$)], virtually only one leading wave is formed that is similar to a horseshoe-shaped soliton [3]. In contrast to the one-dimensional soliton, its damping is determined not only by the dissipation but also by the two-dimensional spreading. As is seen, the amplitude of the leading soliton is larger than that of the horseshoe-shaped wave packet associ-

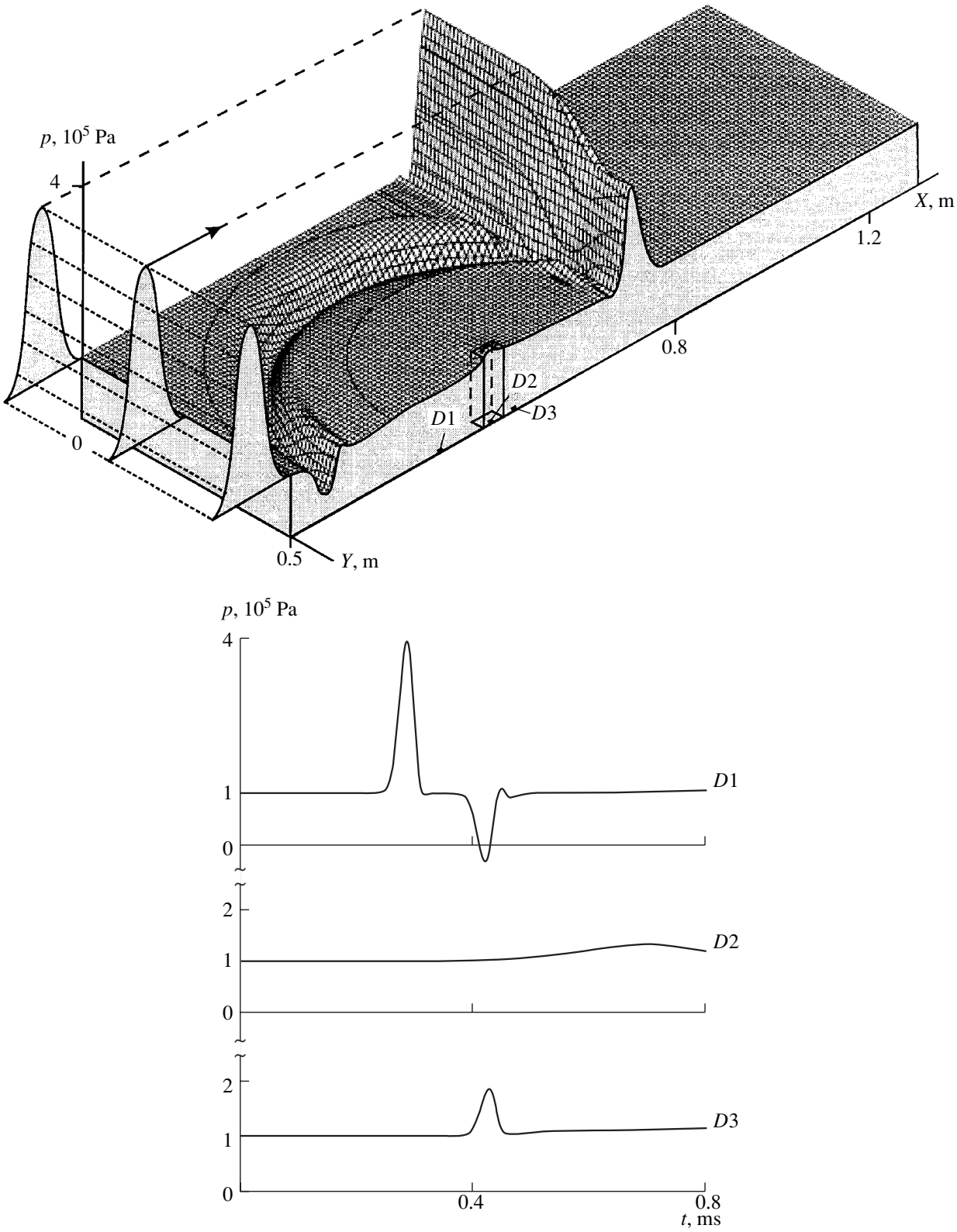

Fig. 1. Propagation of a wave pulse in a liquid in the case of a finite-size bubble screen. The pressure distribution $p(x, y)$ is given for the time moment $t = 0.6$ ms. Calculated oscillograms for the $D1$, $D2$, and $D3$ sensors are presented. The sensors are located at a distance of 0.1 m ahead of the bubble screen, in the middle of the bubble screen, and beyond the bubble screen at a distance of 0.05 m from its rear boundary, respectively. The initial parameters of the water-air mixture and the pulse are $l_x = l_y = 0.05$ m, $\alpha_{g0} = 10^{-2}$, $a_0 = 10^{-3}$ m, $p_0 = 0.1$ MPa, $T_0 = 300$ K, $\Delta p_0 = 0.3$ MPa, and $\delta t = 0.1$ ms.

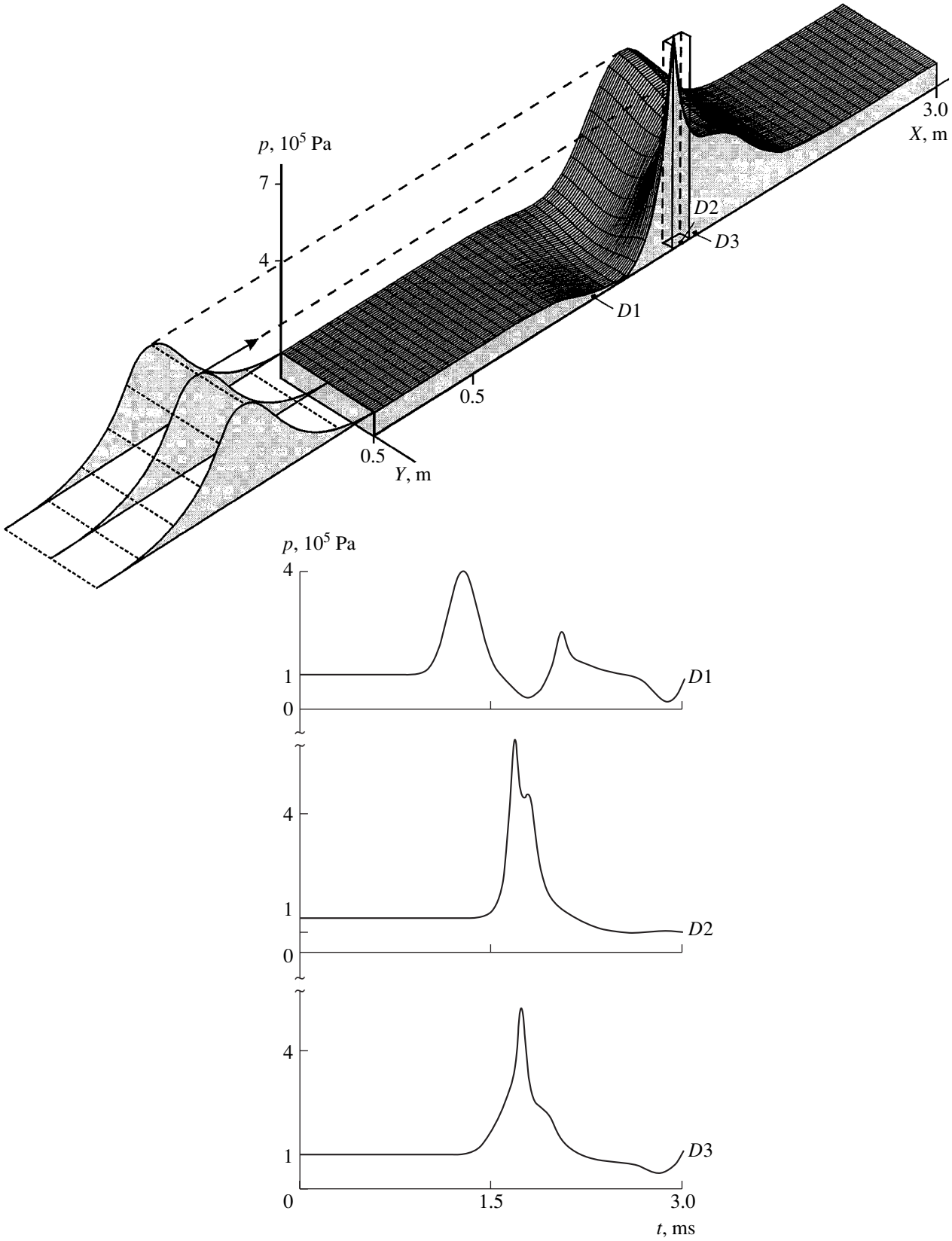

Fig. 2. The same as in Fig. 1, with the pulse duration $\delta t = 1$ ms. The pressure distribution $p(x, y)$ is presented for the time moment $t = 1.7$ ms. Calculated oscillograms are given for $D1$, $D2$, and $D3$ sensors located at a distance of 0.4 m ahead of the bubble screen, in the middle of the bubble screen, and beyond the bubble screen at a distance of 0.05 m from its rear boundary, respectively. Other parameters are the same as in Fig. 1.

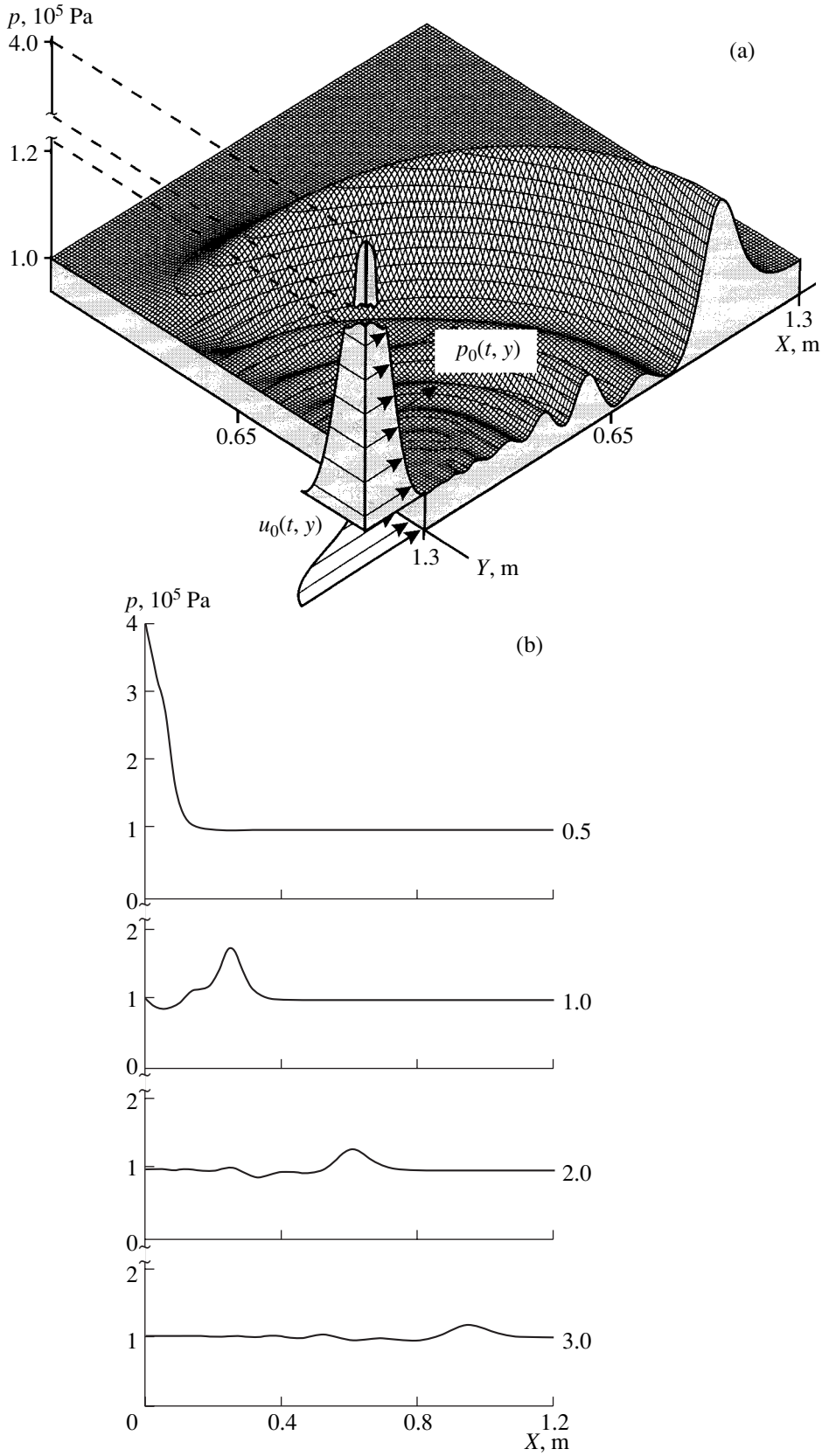

Fig. 3. Evolution of a concentrated (along the transverse coordinate) wave pulse in the water–air bubble mixture. The initial parameters of the mixture and the pulse are $\alpha_{g0} = 10^{-3}$, $a_0 = 10^{-3}$ m, $\Delta p_0 = 0.3$ MPa, $\delta t = 1$ ms, and $\delta y = 0.4$ m. (a) The pressure distribution $p(x, y)$ for a time moment $t = 3$ ms; (b) pressure plots along the x-coordinate for $y = L_y/2$. Numbers near curves indicate the time t, ms.

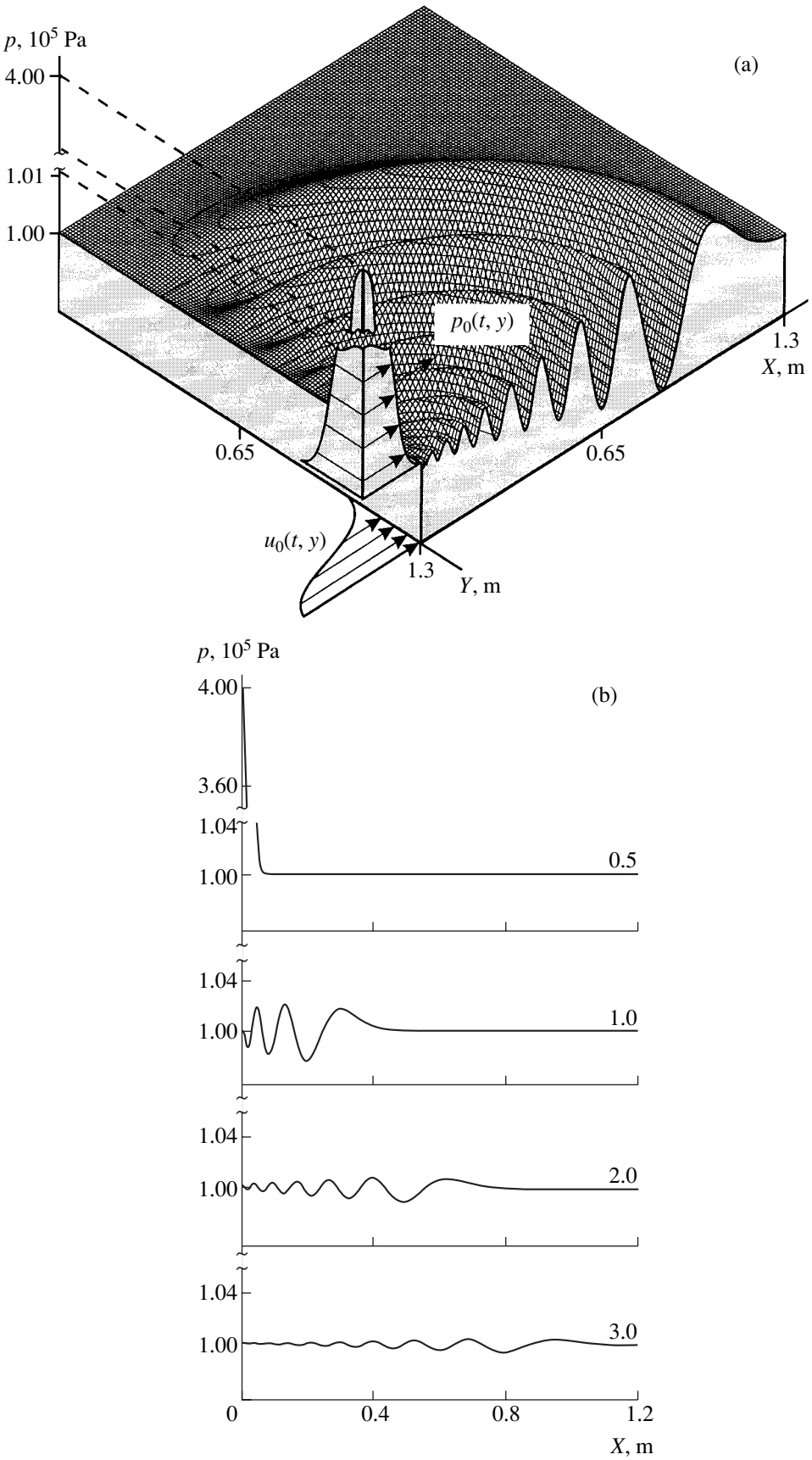

Fig. 4. The same as in Fig. 3 for the pulse duration $\delta t = 0.1$ ms ($\delta y = 0.04$ m). Other parameters are the same as in Fig. 3.

ated with the manifestation of the bubble radial inertia. In the case of a short pulse (Fig. 4), when $\delta t \sim \omega_M^{-1}$, a diverging wave packet forms with characteristic wavelengths $\lambda \simeq \frac{C}{\omega_M}$.

REFERENCES

1. R. I. Nigmatulin, *Dynamics of Multiphase Media* (Nauka, Moscow, 1987), Vols. 1, 2.
2. S. S. Kutateladze and V. E. Nakoryakov, *Heat-and-Mass Transfer and Waves in Gas-Liquid Systems* (Nauka, Novosibirsk, 1987), p. 302.
3. B. B. Kadomtsev and V. I. Petviashvili, Dokl. Akad. Nauk SSSR **192**, 753 (1970) [Sov. Phys. Dokl. **15**, 539 (1970)].
4. R. I. Nigmatulin, V. Sh. Shagapov, and N. K. Vakhitova, Dokl. Akad. Nauk SSSR **304**, 1077 (1989) [Sov. Phys. Dokl. **34**, 98 (1989)].

Translated by G. Merzon